APPLICATIONS OF A NUCLEAR TECHNIQUE FOR DEPTH-SENSITIVE HYDROGEN ANALYSIS: TRAPPED H IN LUNAR SAMPLES AND THE HYDRATION OF TERRESTRIAL OBSIDIAN

Thesis by

Douglas Albert Leich

In Partial Fulfillment of the Requirements

for the Degree of

Doctor of Philosophy

California Institute of Technology

Pasadena, California

1974

(Submitted November 20, 1973)

ACKNOWLEDGEMENTS

I wish to express my sincere appreciation to Professor Thomas A. Tombrello for his much needed guidance, advice, and constant interest throughout the course of this research. I also gratefully acknowledge Professor Donald S. Burnett for his intense interest and indispensible help in the lunar sample investigations, as well as for his many helpful suggestions in all phases of this work.

Many members of the Kellogg Radiation Laboratory were directly or indirectly helpful to this work, and particular thanks go to Messers. Richard H. Goldberg and Roland R. Lee. It is a pleasure to acknowledge the entire Kellogg staff for the friendly and stimulating atmosphere they have provided and for valuable support and assistance.

The author would like to thank Professors G. J. Wasserburg, S. Epstein and H. P. Taylor, Jr., Dr. I. Friedman and Mr. J. E. Ericson for their support and for many useful discussions. I am grateful for the financial assistance provided by an NDEA fellowship and by various assistantships awarded to me by the California Institute of Technology. This research was supported in part by the National Science Foundation grant GP - 28027.

Finally, I wish to thank my wife, Sandra, and her mother, Mrs. Virginia Franklin, who collaborated in the typing of this thesis and who have been patient, understanding, and helpful in many ways.

ABSTRACT

The resonant nuclear reaction $^{19}F(p,\alpha\gamma)^{16}O$ has been used to perform depth-sensitive analyses for both fluorine and hydrogen in solid samples. The resonance at 0.83 MeV (center-of-mass) in this reaction has been applied to the measurement of the distribution of trapped solar protons in lunar samples to depths of $\sim\frac{1}{2}$ μm. These results are interpreted in terms of a redistribution of the implanted H which has been influenced by heavy radiation damage in the surface region. Fluorine determinations have been performed in a 1-μm surface layer on lunar and meteoritic samples using the same $^{19}F(p,\alpha\gamma)^{16}O$ resonance. The measurement of H depth distributions has also been used to study the hydration of terrestrial obsidian, a phenomenon of considerable archaeological interest as a means of dating obsidian artifacts. Additional applications of this type of technique are also discussed.

TABLE OF CONTENTS

I. INTRODUCTION

The use of resonant nuclear reactions to determine the concentration of certain light elements as a function of depth in solid samples has developed over the last decade as a result of increasing interest in properties of surfaces and in surface-related phenomena. Work begun by Amsel and Samuel (1962) using resonances in the $^{18}O(p,\alpha)^{15}N$ and $^{27}Al(p,\gamma)^{28}Si$ reactions to study anodic oxidation has led to a continuing program of investigation of the processes of oxygen diffusion in solids using the $^{18}O(p,\alpha)^{15}N$ reaction (Choudhury et al., 1965; Palmer, 1965) and the $^{16}O(d,p)^{17}O$ reaction (Amsel et al., 1968). Another group (Ollerhead et al., 1966) has used the $^{17}O(^{3}He,\alpha)^{16}O$ reaction in a study of oxygen diffusion and oxidation. The idea of using resonant nuclear reactions to study the depth distributions of implanted ions in solids (Porat and Ramavataram, 1960) has been applied to the measurement of ^{15}N range distributions (Phillips and Read, 1963) and, more recently, ^{18}O range distributions (Whitton et al., 1971) at various implantation energies, using the reactions $^{15}N(p,\alpha\gamma)^{12}C$ and $^{18}O(p,\alpha)^{15}N$, respectively. Resonances in the $^{19}F(p,\alpha\gamma)^{16}O$ reaction have also been used (Möller and Starfelt, 1967; Padawer, 1970) to measure the concentration profiles of fluorine contamination in metals. The purpose of the present experimental study is to apply a new variation of this type of technique to the measurement of hydrogen depth distributions in solids by reversing

the roles of projectile and target in the $^{19}F + p$ system.

The motivation for this study has mainly been supplied by the lunar science program. Large noble gas concentrations were observed in the preliminary examination of the fine lunar soil material (LSPET, 1969). In order to prove that this large rare gas component was the result of solar wind ion implantation, several groups performed experiments to show that the rare gases were located near the surfaces rather than uniformly distributed throughout the volume of the grains. Measurement of the rare gas content of soil samples after removal of a surface layer by chemical etching showed that the rare gases were indeed located near the surfaces of the grains, confirming evidence supplied by the observation of a distinct anti-correlation between grain size and rare gas content per gram in the Apollo 11 soils (Eberhardt et al., 1970; Hintenberger et al., 1970; Kirsten et al., 1970). However, the implied thicknesses (ranging from 0.2 - 8 μm) of the gas-rich surface layers were significantly larger than typical solar wind ion ranges of 0.01 - 0.05 μm, suggesting extensive modification of the distribution of the implanted ions. The resonant nuclear reaction depth analysis technique, using the reaction $^{1}H(^{19}F,\alpha\gamma)^{16}O$, made possible a direct measurement of the depth distribution of implanted hydrogen in lunar samples, providing an important check on the somewhat surprising results of the chemical etching experiments. Due to its excellent depth resolution (~0.02 μm), this

technique is particularly well suited to the investigation of the historical record of solar wind and other particle radiations contained in extraterrestrial materials and of the processes which modify the distribution of the implanted ions.

A second problem to which this technique has been successfully applied is the study of obsidian hydration. An archaeological technique developed for dating of obsidian artifacts depends on the correlation of the thickness of a hydration "rind" on the surface of a given obsidian artifact, which can be observed in thin-section, with the age of the obsidian surface (Friedman and Smith, 1960). High resolution hydrogen depth profile measurements on hydrated obsidian samples, made possible by the $^{1}H(^{19}F,\alpha\gamma)^{16}O$ resonant nuclear reaction technique, represent a valuable aid toward understanding the hydration process. Such an understanding is essential to the establishment of the obsidian hydration dating technique as a reliable chronometer.

In Section II of this thesis I shall discuss the experimental methods and apparatus along with the results of implantation experiments performed as a test of the analytical technique. Results of measurements on lunar samples, including measurements of fluorine depth distributions using the $^{19}F(p,\alpha\gamma)^{16}O$ reaction, are presented in Section III. Section IV is concerned with measurements of obsidian hydration profiles. In conclusion, Section V includes an evaluation of the technique and its applications, and a discussion

of further promising applications of nuclear reactions as depth-sensitive analysis probes. The development of the $^{1}H(^{19}F,\alpha\gamma)^{16}O$ technique discussed in Section II has been previously described by Leich and Tombrello (1973). Many of the lunar sample results and ideas presented in Section III have also been published (Leich, Tombrello and Burnett, 1973a) or are in press (Leich, Tombrello and Burnett, 1973b). A manuscript dealing with the obsidian hydration measurements discussed in Section IV is being prepared for publication (Lee et al., 1973).

II. EXPERIMENTAL METHODS

In this section the experimental methods, techniques, and apparatus are treated in detail.

A. Depth Analysis for Hydrogen Using $^{1}H(^{19}F,\alpha\gamma)^{16}O$

The applicability of the resonant nuclear reaction depth analysis technique depends on the existence of an isolated resonance in a nuclear reaction involving an isotope of the element to be analyzed. In Appendix A the general case of a nuclear reaction A(a,b)B is considered in some detail, with regard to its use as a depth analysis probe for nuclei A, when such a resonance exists. The existence of a strong, narrow, isolated resonance in the reaction $^{1}H(^{19}F,\alpha\gamma)^{16}O$ has been exploited in this study to determine hydrogen depth profiles in solid samples. The resonance employed occurs at an ^{19}F energy E_R = 16.45 MeV with a total width Γ (FWHM) of $\sim$89 keV, corresponding to a proton energy of 0.872 MeV and width of 4.7 keV for the same resonance in $^{19}F(p,\alpha\gamma)^{16}O$ (Ajzenberg-Selove, 1972). The peak cross section σ_R is $\sim$0.6 barn for emission of an α particle leading to one of three excited states of the residual ^{16}O nucleus at excitation energies of 6.1, 6.9, and 7.1 MeV (Ajzenberg-Selove and Lauritsen, 1959). All three states de-excite by emission of a prompt γ ray directly to the ground state. At ^{19}F energies different from the resonance energy by more than a few Γ the cross section for the production of the high energy γ rays is

negligible. Thus, if the surface of a material containing hydrogen is irradiated with ^{19}F ions at energies sufficiently greater than the resonance energy E_R, the ^{19}F ions will gradually slow down, due to electronic collisions, until at a depth x_R the resonance energy is reached and the reaction will occur at a rate proportional to the hydrogen concentration in a thin layer at x_R. At greater depths the ^{19}F energy will fall below the resonance energy where the cross section is again negligible compared to σ_R. Hence hydrogen located outside the layer at $x_R \pm \Gamma/[-dE/dx]$ contributes only a negligible amount to the total reaction yield. Since the stopping power, dE/dx (a negative quantity), is nearly independent of energy (within ~1%) (Northcliffe, 1963) in the relevant range of ^{19}F energies, the depth x_R can be related to the ^{19}F beam energy E_o by the linear relation

$$x_R = \frac{E_o - E_R}{[-dE/dx]} \quad . \tag{1}$$

Selection of the ^{19}F beam energy E_o is equivalent to specifying the depth x_R at which the hydrogen concentration is to be determined, and measuring the γ-ray production rate as E_o is varied gives a direct indication of hydrogen concentration as a function of depth in the target. The relation between $H(x_R)$, the hydrogen concentration at depth x_R, and $Y(E_o)$, the reaction yield per incident ^{19}F ion of energy E_o, is shown in Appendix A (equation A.7) to be

given by

$$Y(E_o) = \frac{\pi \sigma_R \Gamma}{2[-dE/dx]_R} H(x_R), \tag{2}$$

using the Breit-Wigner dispersion equation,

$$\sigma(E) = \sigma_R \frac{\Gamma^2/4}{(E-E_R)^2 + \Gamma^2/4} \tag{3}$$

to describe the dependence of the cross section σ on ^{19}F energy E in the vicinity of the resonance at E_R.

A second strong resonance at an ^{19}F energy of 17.64 MeV producing the same characteristic γ rays as the first resonance (although in slightly different proportions) limits the depth range over which the first resonance can be used in the straightforward manner outlined above to about 0.4 μm. For H distributions extending to greater depths, information can still be extracted from the excitation function $Y(E_o)$ for $E_o > E_{R2} = 17.64$ MeV. (Since we must now deal with two resonances simultaneously, the subscripts 1 and 2 are used in the following to indicate the resonances at 16.45 MeV and 17.64 MeV respectively.) The yield per incident ^{19}F ion is now the sum of the yield from the first resonance due to hydrogen at depth $x_{R1} = \int_{E_o}^{E_{R1}} \frac{dE}{[dE/dx]}$ and a contribution from the second resonance due to hydrogen at depth $x_{R2} = \int_{E_o}^{E_{R2}} \frac{dE}{[dE/dx]}$, i.e., for $(E_o - E_{R2}) >> \Gamma_2 (= 154$ keV),

$$Y(E_o) = Y_1(E_o) + Y_2(E_o) \tag{4}$$

where

$$Y_1(E_o) = \frac{\pi\, \sigma_{R1}\, \Gamma_1}{2[-dE/dx]_{R1}}\, H(x_{R1}) \tag{5}$$

and

$$Y_2(E_o) = \frac{\pi\, \sigma_{R2}\, \Gamma_2}{2[-dE/dx]_{R2}}\, H(x_{R2})\ . \tag{6}$$

But since $x_{R2} = x_{R1} - \Delta x$, where $\Delta x \equiv \int_{E_{R2}}^{E_{R1}} \frac{dE}{[dE/dx]}$, we have

$$Y_2(E_o) = \frac{\pi\, \sigma_{R2}\, \Gamma_2}{2[-dE/dx]_{R2}}\, H(x_{R1} - \Delta x), \tag{7}$$

and hence,

$$Y_2(E_o) = \frac{\sigma_{R2}\, \Gamma_2\, [dE/dx]_{R1}}{\sigma_{R1}\, \Gamma_1\, [dE/dx]_{R2}}\, Y_1(E_o - \Delta E), \tag{8}$$

with $\Delta E \equiv \int_o^{\Delta x} [-dE/dx]dx$. The $\sim$5% variation of the stopping power over the extended range of useful ^{19}F beam energies may be approximated quite accurately by a linear decrease with energy. With this approximation, we obtain $\Delta E \simeq \Delta E_R \frac{[dE/dx]_o}{[dE/dx]_{R2}}$ where $[dE/dx]_o$ is the value of the stopping power at E_o and $E_{R2} - E_{R1}$. Substituting equation 8 into equation 4 leads to the expression

$$Y_1(E_o) = Y(E_o) - \frac{\sigma_{R2}\,\Gamma_2\,[dE/dx]_{R1}}{\sigma_{R1}\,\Gamma_1\,[dE/dx]_{R2}}\,Y_1(E_o - \Delta E). \qquad (9)$$

Hence, $Y_1(E_o)$ can be determined for $E_o > E_{R2}$ by calculating $Y_2(E_o)$ from a similar determination of Y_1 at a lower beam energy, $E_o - \Delta E$. (If $(E_o - \Delta E) < (E_{R2} - \Gamma_2)$, $Y_1(E_o - \Delta E)$ is measured directly.) The hydrogen concentration $H(x_{R1})$ is then inferred from the determination of $Y_1(E_o)$ in the usual way, using equation 5.

Hydrogen depth profiles can be determined, using the procedures outlined above, with a depth resolution δx depending on the width Γ_1 and on the spread in energy of the ^{19}F ions as they penetrate the sample. Using equation A.9 of Appendix A, we can estimate the resolution by

$$\delta x \simeq \frac{\sqrt{\Gamma_1^{\,2} + (\Delta E_o)^2 + \Omega^2(x_{R1})}}{2[-dE/dx]} \qquad (10)$$

where ΔE_o is the FWHM spread in beam energy (a few keV) and $\Omega(x_{R1})$ is the FWHM energy straggling at a depth x_{R1}. Figure 1 shows the calculated resolution δx as a function of depth in a quartz sample using an estimate of the energy straggling based on theoretical treatments of atomic collision processes (Maccabee et al., 1968). The 0.02-μm resolution available near the surface is gradually degraded by the energy straggling to 0.03 μm at a depth of nearly 2 μm. This represents an order of magnitude improvement in reso-

lution compared to chemical etching and other destructive sectioning techniques.

The sensitivity of nuclear reaction analysis techniques depends to a large extent on the importance of competing reactions; i.e., reactions produced by the ion beam on other constituents of the sample. Some of these reactions may result in reaction products which are difficult to distinguish from the products of the reaction of interest. For $^{1}H(^{19}F,\alpha\gamma)^{16}O$ there is very little interference of this sort (until the ^{19}F energy is raised above $\sim$20 MeV) since the production of the 6-7 MeV γ rays is quite copious. Above 20 MeV, the sensitivity falls rapidly to zero because of the rapid increase in background due to what appears to be neutron production by $(^{19}F,n)$ and/or $(^{19}F,2n)$ reactions on oxygen as the Coulomb barrier height is approached. This interference has been the determining factor in the $\sim$2-μm depth limit of the present measurements.

B. Experimental Apparatus

The extreme sensitivity of measurements of this kind to surface contamination necessitated the design and construction of a special ultrahigh vacuum (UHV) scattering chamber. The primary concerns as sources of hydrogen contamination were diffusion pump oil vapors (since accelerator beam tubes are normally pumped by oil diffusion pumps) and water vapor. The solution of this problem has been to equip the scattering chamber with a clean, self-contained getter-ion pumping system, and to baffle the accelerator-scattering chamber interface allowing passage of the ion beam with a minimal

flow of contaminant vapors from the accelerator beam tube. A schematic drawing of the scattering chamber vacuum system is shown in Figure 2.

The scattering chamber itself consists of two stainless steel UHV flanges bolted together with a copper gasket metal-to-metal seal to form a cylindrical exterior 20 cm in diameter and 4.5 cm deep. The interior faces of the flanges were machined to form a cavity 15 cm in diameter and 3 cm deep. A direct drive rotary feedthrough was mounted on a port at the rear of the scattering chamber so that its shaft extended into the cavity along the chamber axis. A 10-cm diameter aluminum target wheel was mounted on this shaft using glass spacers to electrically insulate the wheel from the rotary drive shaft. Twelve 16.5-mm diameter by 6-mm deep holes equally spaced along a 7-cm diameter circle on the target wheel provide mounts for samples to be analyzed. One of two ports on the front face of the chamber serves as the connection to the accelerator beam tube and is placed 3.5 cm off-axis to line up with the centers of the target mounts. The second port is fitted with a window and allows precise positioning of the target wheel using degree markings on the edge of the wheel and a vernier mounted on the chamber wall, and also allows the targets to be viewed while in their mounts in the sealed scattering chamber. A sliding electrical contact fabricated from beryllium-copper alloy makes contact with the aluminum target wheel and connects with one lead of a ceramic-sealed electrical feedthrough, thus allowing the beam current to be

collected from the target wheel with negligible leakage to ground.

The scattering chamber vacuum is maintained by a getter-ion pumping system with a pumping speed of 50 liters per second for air. A Varian sublimation pump provides most of the pumping speed by means of the gettering action for chemically reactive gases of a thin layer of titanium coating the interior walls of the water-cooled stainless steel pump chamber. The titanium layer is periodically renewed by sublimation from one of three titanium alloy filaments in the center of the pump chamber. A small pumping speed for inert gases is maintained by a standard 15ℓ/s Varian Vac-Ion pump. All vacuum connections in the scattering chamber and vacuum system are made using copper-gasket metal-to-metal seals, allowing the entire system to be baked at temperatures up to 300°C to drive trapped gases from the interior surfaces. A straight-through 1-cm bore gold seal valve is used as a beam-line isolation valve, while a second gold seal valve is used on the roughing line. A molecular sieve sorption pump is used to obtain the necessary 10^{-2} Torr vacuum to start the ion pump.

The getter-ion pumping system, together with the use of low vapor pressure bakeable materials in the construction of the scattering chamber, enables a vacuum of $<10^{-9}$ Torr to be routinely maintained, and eliminates internal sources of hydrocarbon contamination. To minimize contamination from pump oil and other vapors in the accelerator beam tubes, the connection of the scattering chamber to the beam line is interfaced with a 40-cm long, 1-cm bore

liquid nitrogen cooled baffle. The trapping of condensable vapors on the refrigerated walls of this low-conductance tube enables the getter-ion pumping system to maintain a vacuum of $\sim 10^{-9}$ Torr in the scattering chamber with beam on the target. Thus, sources of hydrogen contamination are minimized while another potential problem, the build-up of carbon deposits on the targets from the cracking of hydrocarbon vapors during irradiation with an ion beam, is virtually eliminated.

The ^{19}F beam necessary for hydrogen depth analysis is provided by the Caltech tandem accelerator. Fluorine ions are extracted from a duoplasmatron ion source using freon-14 (CF_4), diluted with helium, as the source gas. $^{19}F^-$ ions are accelerated to the terminal where they are stripped to a variety of positive charge states. Following the second stage of acceleration, the $^{19}F^{4+}$ charge state is selected by a 90° magnetic analyzer. The resulting $^{19}F^{4+}$ beam is monoenergetic to within a few parts in 10^4. The beam energy can be determined precisely using a digital nuclear magnetic resonance gaussmeter (Alpha Scientific, Inc. Model 3193) to measure the field between the two poles of the analyzing magnet, and a calibration performed by Mann, et al. (1973). The beam is then steered into the target room beam tube (S 10° leg) and focused through two sets of collimating slits located 50 cm apart at the end of the flight tube as indicated in Figure 2. With the beam-line gate valve and the scattering chamber isolation valve open, the $^{19}F^{4+}$ beam passes through the 1-cm diameter tube of the liquid

nitrogen cooled baffle and into the scattering chamber where the ^{19}F ions are stopped in the target. The target wheel is held at a potential of +300 V to retain secondary electrons, so each ion deposits a net charge q of +4e. This charge is continuously collected by the sliding electrical contact on the target wheel and the resulting current is fed out the electrical feedthrough, through the 300 V bias battery and a 1 MΩ limiting resistor, and delivered to the input of a Brookhaven Nuclear Instruments Model 1000 current integrator. This instrument amplifies the input current and puts out a digital pulse each time the integrated current reaches a preset charge, typically 6.0×10^{-10} Coulomb.

A 7.6-cm x 7.6-cm lead shielded NaI(Tℓ) scintillation detector placed outside the scattering chamber at about 30° scattering angle and about 7 cm from the target is used to detect γ radiation from the excited ^{16}O nuclei. A photomultiplier converts the scintillations into voltage pulses which are then amplified and analyzed using a 400-channel pulse-height analyzer (RIDL 34-27 series). The pulse-height spectrum shown in Figure 3 is the result of a 10-μC irradiation of an analyzed sample of Belvidere Mountain chlorite (1.64% H by weight) with a 30-nA beam of 17.2 MeV $^{19}F^{4+}$ ions. A 3.7-to 7.4-MeV counting window includes the full-energy peaks and single and double escape peaks, but excludes the tail of the Compton distribution in the response of the NaI(Tℓ) crystal to the three γ rays. With this energy window, the counted fraction η of all γ rays emitted is estimated, using the chlorite standard, to be about 0.022 (see Appendix C).

C. Data Collection and Reduction

The procedure for measurement of the excitation function $Y_1(E_o)$ involves counting the number of γ-rays emitted for a given number of incident $^{19}F^{4+}$ ions at a series of beam energies E_o. First the beam energy E_o must be selected and the beam steered and focused onto the target wheel. Then a beam-chopping magnet is turned on, steering the beam out of the beam tube, and the sample to be analyzed is set in position by manipulating the rotary feed-through and lining up the correct degree mark on the target wheel with the vernier. The total amount of beam charge Q to be collected per data point is preset on a mechanical register, and the run is started by activating a gate control which simultaneously starts the counting electronics and switches off the beam-chopping magnet, allowing the beam to irradiate the target. Counts are stored in the pulse-height analyzer during the entire "beam on" period, while a digital register tracks the integrated beam charge by tallying the pulses from the current integrator. When this register reaches the value preset on the accompanying mechanical register, a gate is automatically activated which turns on the beam-chopping magnet, thereby stopping the beam, and also blocks further input into the pulse-height analyzer. The count totals in the channels corresponding to the selected 4-7 MeV energy window are then summed and read out. This number, $N(E_o)$, is recorded along with the energy E_o, the total charge Q, and the total "beam on" time t, normally 3 - 10 minutes for beam currents in the 10 - 30 nA range with Q = 6 μC. The analyzer memory and current integration register are then cleared,

a new beam energy is selected, and the sequence is repeated for the next datum. The optimum beam energy sequence spaces data points by an amount consistent with the spatial resolution of the measurements, or about 50 keV. The range of energies used begins slightly below the resonance energy E_{R1} and continues up to a maximum energy determined by the depth of the distribution being measured.

Once data have been collected in this manner, they can be transformed to a depth profile by plotting the number of counts $N(E_o)$ for a given total beam charge Q vs. the beam energy E_o, and performing simple linear scale transformations. The energy scale becomes a depth scale using the conversion $x_{R1} = \frac{E_o - E_{R1}}{[-dE/dx]}$. The data $N(E_o)$ include a background contribution consisting of a beam independent portion (room background) primarily due to cosmic rays, and a beam dependent background due partially to competing reactions and partially to weaker resonances in the reaction $^{1}H(^{19}F,\alpha\gamma)^{16}O$ at lower energies. The background can be taken into account by writing

$$N(E_o) = \frac{Q}{q}[\eta Y(E_o) + A] + Bt \qquad (11)$$

where η is the detection efficiency, q is the charge per incident ion (= 4e), A represents the beam-dependent background (counts per incident ion) and B the beam-independent background (counts per second). Since B is independent of Q and E_o, the contribution Bt can be held constant by holding the time t constant, or equivalently holding the beam current constant, for each data point. The beam

dependent background AQ/q will also be constant if A is independent of E_o over the energy range used. This assumption has been verified (to within ± 10%), by measurement of hydrogen-free samples, and samples with constant volume concentrations of H such as the chlorite standard, up to an energy of ∿20 MeV. Thus, if the beam current is held constant, equation 11 becomes

$$N(E_o) = \frac{Q}{q} \eta Y(E_o) + \kappa \qquad (12)$$

where the constant κ (equal to $(AQ/q)+ Bt$) is evaluated from data taken at beam energies <u>below</u> E_{R1} where $Y(E_o)$ goes to zero. For $E_o < E_{R2}$, the scale transformation used to give $H(x_{R1})$ is obtained by substituting equation 5 into equation 12:

$$H(x_{R1}) = \frac{2[-dE/dx]_{R1} q}{\pi \eta \sigma_{R1} \Gamma_1 Q} [N(E_o) - \kappa] . \qquad (13)$$

For $E_o > E_{R2}$, the contribution $N_2(E_o) = \frac{Q}{q} \eta Y_2(E_o)$ must be calculated and subtracted from the data to give

$$H(x_{R1}) = \frac{2[-dE/dx]_{R1} q}{\pi \eta \sigma_{R1} \Gamma_1 Q} [N(E_o) - N_2(E_o) - \kappa] . \qquad (14)$$

following the procedures outlined in Part A of this section. Hence, for $E_{R1} < E_o < E_{R2}$, the $N(E_o)$ data scale is converted to a hydrogen concentration scale with the zero point determined by the constant background contribution κ, and the scaling factor given as in

equation 13 above. For $E_o > E_{R2}$, $N_2(E_o)$ must be subtracted from the data as in equation 14 in order to extract the hydrogen concentration for the depth x_{R1}. More sophisticated numerical deconvolutions of the resonance shape from the excitation function to yield a more accurate depth profile are possible, in principle, but have not proved necessary in practice.

Rather than rely on uncertain values for σ_{R1} and Γ_1 and an estimate of η based on these same values, a more direct approach is used in which the weight fraction of hydrogen W_H is obtained by direct comparison with counting rates obtained from irradiation of the chlorite standard:

$$W_H(x_{R1}) = W'_H \left(\frac{[dE/d(\rho x)]_{R1}}{[dE/d(\rho x)]'_{R1}} \right) \left(\frac{Q'}{Q} \right) \left(\frac{N(E_o) - \kappa}{N' - \kappa'} \right) \qquad (15)$$

where

$$[dE/d(\rho x)]_{R1} = \frac{1}{\rho} [dE/dx]_{R1},$$

$$[dE/d(\rho x)]'_{R1} = \frac{1}{\rho'} [dE/dx]'_{R1},$$

ρ and ρ' are the densities of the target medium and the chlorite standard respectively, $[dE/dx]'_{R1}$ is the stopping power of the chlorite for ^{19}F ions of energy E_{R1}, and N' and κ' are the total counts and background counts, respectively, for data taken for a total beam charge Q' per data point at energies between E_{R1} and E_{R2}. The densities ρ and ρ' need not be known to use equation 15 since the quantities $[dE/d(\rho x)]_{R1}$ and $[dE/d(\rho x)]'_{R1}$ can be calculated

directly from tabulated stopping powers (Northcliffe, 1963; Northcliffe and Schilling, 1970) and chemical analyses of the samples as described in Appendix D.

D. Implantation Tests

In order to establish the sensitivity and reliability of this technique, implantation experiments have been carried out on fused silica, crystalline quartz, and Ca-rich feldspar samples using 12-keV protons with doses of about 10^{16} cm^{-2}. The target materials were chosen for their chemical and physical similarity to the returned lunar samples (silicate glasses and rocks). Targets were chemically cleaned and then baked in the scattering chamber to remove surface contamination prior to implantation. A magnetically analyzed proton beam with a flux of about 10^{12} s^{-1}-cm^{-2} ($\sim$0.1 μA into a $\frac{1}{2}$ cm^2 area) was obtained for implantation from a duoplasmatron ion source. Following implantation of a set of targets the scattering chamber was transferred to the tandem accelerator beam line where a 0.1-μA beam of $^{19}F^{4+}$ ions was directed into a 4-mm spot for the H analysis. Figure 4 shows data for a typical implanted target and a target which was not implanted but was otherwise identical. Figure 5 shows the implantation profile obtained by subtracting the data for the blank from the data for the implanted sample. The depth and H concentration scales are calculated using the stopping power of SiO_2 for ^{19}F ions calculated from data in Northcliffe (1963) and Northcliffe and Schilling (1970). The experimentally determined distributions show

some deviation from the theoretical range distribution (Lindhard et al., 1963). A comparison between the measured and theoretical mean range and full-width at half-maximum (FWHM) is shown in Table 1. The differences may, in part, represent the effects of diffusion; accelerated, perhaps, by localized heating from the implantation beam. Repeated analyses of a single implanted sample show gradual but consistent inward shifting and broadening of the distribution, suggesting a continuation of the same process by which the range distribution is distorted during the implantation, although at a slower rate. With the exception of this effect, the profiles are reproducible; thus, there is no reason to doubt that the actual proton distribution is being measured. These results also establish the quantitative retention, within a factor of two, of amorphous and crystalline materials for implanted protons. Similar experiments with aluminum targets gave negative results in this regard, with less than 5% retention under similar experimental conditions.

E. Depth Anaylsis for F, Na, and Aℓ with Proton-Induced Nuclear Reactions

Depth distributions of fluorine in solid samples can be measured using a proton beam to produce γ radiation from the $^{19}F(p,\alpha\gamma)^{16}O$ reaction in a manner entirely analogous to the measurement of hydrogen distributions with a ^{19}F beam. The same resonance is used in both analyses, occurring at a proton energy $E_{R1} = 0.872$ MeV with FWHM $\Gamma_1 = 4.7$ keV in the frame of reference in which the ^{19}F target is initially at rest. The proton beam energy E_o is varied to

measure the excitation function $Y_1(E_o)$, and the fluorine concentration $F(x_{R1})$ at depth $x_{R1} = \int_{E_o}^{E_{R1}} \frac{dE}{[dE/dx]}$ is found from

$$Y_1(E_o) = \frac{\pi \sigma_{R1} \Gamma_1}{2[-dE/dx]_{R1}} F(x_{R1}) \qquad (16)$$

in analogy with equation 5. Here $[dE/dx]_{R1}$ is the stopping power of the medium for <u>protons</u> of energy $E_{R1} = 0.872$ MeV. The γ-ray yield due to the resonance at $E_{R2} = 0.935$ MeV ($\Gamma_2 = 8.1$ keV) can be unfolded in the same manner, and in this way the depth distributions can be measured beyond the 1-μm depth corresponding to an energy loss of $\Delta E_R \equiv E_{R2} - E_{R1} = 63$ keV. The proton beam energies necessary for this analysis can also be obtained from the Caltech tandem accelerator, and the measurements can be performed with the same apparatus and electronic set-up as is used for the hydrogen analysis. Since the same characteristic γ rays are detected with the same efficiency η in each case, even the discriminator levels remain the same. All that need be done is to switch from a 16.45 + MeV ^{19}F beam to a 0.872 + MeV proton beam, and the distribution being measured becomes that of fluorine rather than hydrogen.

Aluminum and sodium distributions can also be measured by detecting high energy γ rays from (p,γ) reactions. For aluminum, the $^{27}Al(p,\gamma)^{28}Si$ resonance used occurs at a proton energy of 0.992 MeV with a width of 0.1 keV resulting in a maximum energy γ ray of 10.8 MeV with a branching ratio of 0.76. Sodium measure-

ments can be performed using a $^{23}Na(p,\gamma)^{24}Mg$ resonance at 1.318 MeV proton energy and a width of 1.4 keV resulting in 11.6 and 13.0 MeV γ rays (Endt and Van der Leun, 1967). Counting windows must be adjusted for the particular γ rays to be detected for Aℓ and Na analyses, thereby altering the detection efficiency η, but otherwise the procedure for obtaining depth distributions follows the same procedures described for hydrogen and fluorine measurements using a single resonance.

Table 2 lists the reactions used in this study to analyze for H, F, Na, and Aℓ, along with the ion energy at resonance, the energy of the principal γ rays, and the reaction sensitivity for each resonance. The latter quantity is defined as the thick target yield per incident ion for a quartz sample containing one ppm by weight of the particular target atoms. The resolution δx for measurement of depth profiles in quartz is shown in Figure 6 for each reaction. The rapid degradation of the resolution with depth for F, Na, and Aℓ is a result of the relatively large energy straggling for protons as compared to heavier ions of comparable velocity. The resolution for H depth profiles suffers little from energy straggling of the ^{19}F ions and remains excellent to a depth of $\sim$2 μm.

III. LUNAR SAMPLE ANALYSIS

Results of hydrogen and fluorine depth distribution measurements on lunar samples are presented and discussed in this section, as well as a simulation experiment performed to determine the possible extent of penetration of terrestrial contaminants into the radiation damaged surface layers of lunar samples. The results of a search for H implanted into a platinum foil exposed to a solar flare during the Apollo 16 mission are also presented.

Knowledge of the depth distribution of hydrogen in lunar samples is important for understanding the origin of the observed H. Implantation of solar wind protons should lead to large surface (within a few hundred angstroms) concentrations of H. The more energetic solar flare protons would result in a distribution extending over a much greater depth range (up to a few millimeters). Indigenous lunar H, incorporated into rocks at the time of their formation, would be distributed throughout the volume of the lunar samples; however, solar wind H inherited from a pre-irradiated parent material could result in a similar volume distribution. Terrestrial contamination, particularly surface absorption of H_2O, is a likely source for observable amounts of H. Consequently, the basic problem in identifying the origin of the lunar H lies in distinguishing the lunar component from terrestrial contamination.

A. Experimental Results

Samples with relatively large (~ 2 mm x 2 mm) smooth surfaces of uniform composition are desirable for analysis by the resonant nuclear reaction techniques employed in this study in order to simplify interpretation of the measurements. Large samples also allow low beam-current densities (typically 10nA of $^{19}F^{4+}$ into a 0.1-cm^2 area) to be used, thereby minimizing the effects of beam heating. These considerations are best satisfied by the lunar glasses, which are a major constituent of the lunar regolith. The samples selected for this study, therefore, are predominantly lunar glass fragments and glass coated rocks.

Samples were obtained in a series of separate allocations. For convenience, however, the samples can be collected into four groups determined by similarities in the particular sample handling and analysis procedures used and by similarities in the samples themselves. These groups are: (1) Apollo 11 and Apollo 15 coarse fines, (2) Apollo 15 glass-coated rocks, (3) Apollo 16 glass-coated rocks, and (4) Apollo 16 samples returned in a vacuum-sealed sample container.

1. Apollo 11 and Apollo 15 coarse fines

The first set of samples obtained for this study consisted of three 2-3 mm sized lunar glass fragments selected on the basis of their size and smoothness from two separate aliquots of Apollo 11 "course fines" (1-4 mm fragments) numbered 10085,1 and 10085,31. The parent sample 10085 consists of the 1-10 mm fragments separated from

the Apollo 11 bulk sample 10002 at the Lunar Receiving Laboratory (LRL). Separate allocations (or other subdivisions) of material from a particular parent sample are indicated by the number following the parent sample number and separated from it by a comma, e.g. 10085,1 and 10085,31. Where such a sample has been further subdivided in our laboratory, an additional identifying number or letter is assigned to each fragment and is preceded by a hyphen, e.g. 10085,31-9.

The 10085 brown glass samples are typical Apollo 11 brown glass as described by many authors (see, for example, Keil et al., 1970). Samples were subjected to a microscope examination in a clean laboratory atmosphere prior to analysis. Two of the samples, 10085,31-9 and 10085,31-12, had been given an ultrasonic rinse in high-purity acetone -- a treatment which is essential in many cases to remove layers of lunar dust from the samples. In order to determine the extent of surface H contamination associated with this procedure, several fused silica discs were given an acetone rinse using exactly the same procedure as was used with the lunar samples. These discs had previously been chemically cleaned and vacuum baked at 300°C and showed no detectable ($<10^{14}$ atoms/cm^2) surface concentration of H. Following the acetone rinse, the silica discs were remounted in the scattering chamber and remeasured with the ^{19}F beam. Surface contamination ranging from only $\sim 10^{14}$ to 10^{15} H atoms/cm^2 were observed, and even these small surface concentrations disappeared almost entirely after a few times 10^{14} ions/cm^2 of illumination with the ^{19}F beam. Although these results show that acetone contamination

is not a problem for normal glass surfaces, the exotic surfaces of lunar samples could conceivably react quite differently to the acetone. However, measurement of the hydrogen distribution on the 10085,1 glass fragment and on a sample from a subsequent allocation (15533,4-1), both before and after exposure to an acetone rinse, resulted in no observable increase in the H content of the sample. We conclude, therefore, that the acetone rinse is not likely to be an important source of H contamination of the lunar samples.

The three 10085 brown glass fragments were mounted in the scattering chamber using aluminum foil to support the sample in the desired position, chosen to expose a smooth, dust-free face to the ^{19}F beam, and then placing a clean, H-free fused silica collimator with a 2-3 mm circular aperture directly over the sample. The resulting target assembly is kept in place in the target wheel with a copper alloy retaining ring. Hydrogen distribution measurements were performed according to the procedures outlined in the preceding section using a 10-15 nA beam of $^{19}F^{4+}$. The beam was collimated to about the same size as the smallest sample ($\sim$2 mm) so that most of the ^{19}F ions would strike the lunar samples, while the fused silica collimators prevent the halo of the ^{19}F beam from illuminating the target holder. Tests have shown that this fused silica material retains very little H after baking under vacuum at 300°C, so ^{19}F ions striking the fused silica instead of the lunar sample contribute a negligible amount to the γ-ray yield. However, since these collimators are fastened to the target wheel the integrated beam current includes a contribution from the ions incident on the collimator as

well as those hitting the lunar sample. Using a sample of the chlorite standard (1.64 percent H) mounted behind one of these collimators, we have determined the fraction of the ^{19}F beam illuminating the collimator to be normally about 0.2 for a collimator with a 2.4 mm aperture. The uncertainty associated with estimating this fraction for a particular distribution measurement does not affect the measured shape of the distribution (provided the fraction remains constant for each data point), but only the estimate of the absolute H content.

Although the density of the target medium need not be known in order to obtain a depth scale for the measured H profile in units of $\mu g/cm^2$, it is generally more convenient to deal with depths measured in the usual distance units. Calculation of the stopping power $dE/d(\rho x)$ proceeds as in Appendix D resulting in a value of -9.0 keV-cm^2-μg^{-1} for an "average" lunar composition (46% SiO_2, 4% TiO_2, 15% Al_2O_3, 14% FeO, 11% CaO, 9% MgO, 0.6% Na_2O, and 0.3% K_2O). The density of a glass of such a composition is estimated to be $\sim 2.6 g/cm^3$ by extrapolating data on commerical glasses and using empirical rules for calculating the density of a glass from its chemical composition (Morey, 1954; Stevels, 1948; Huggins and Sun, 1943). Although the density ρ increases as the FeO and TiO_2 contents increase at the expense of SiO_2 and Al_2O_3, the higher stopping cross sections of the heavier atoms tend to counterbalance the increasing density so that neither $dE/d(\rho x)$ nor dE/dx are as sensitive to the composition as ρ. Hence by assuming a nominal density of $2.6 g/cm^3$

and using the value 9.0 keV-cm^2-μg^{-1} for $-dE/d(\rho x)$ for all lunar glasses, without considering the specific composition of a particular sample, the uncertainty of $\sim$10% in the calculation of the depth scale is dominated by the uncertainties in the estimates of ρ and $dE/d(\rho x)$ for the "average" lunar glass and not by the unknown composition. For simplicity, we have used the same scale conversion for crystalline samples also. The heavy radiation damage associated with long-term solar wind bombardment should transform any exposed crystalline surfaces to a quasi-amorphous state (metamictized) to depths of at least 500-1000 Å as observed by Bibring, et al. (1972) for lunar dust grains. Consequently, the density of the surface layer (to depths of at least $\sim$0.1 μm, and possibly somewhat deeper if radiation damage is still quite heavy below this layer) might be better approximated by the density of a glass rather than that of the relatively undamaged crystalline material somewhat deeper within the lunar rocks.

One of the brown glass fragments, 10085,31-12, revealed a large surface-correlated H content, with a peak density in excess of 2×10^{21} H atoms per cm^3 (more than 1500 ppm H by weight) at a depth of 0.11 μm (Fig. 7). The H concentration profile drops sharply near a depth of 0.20 μm followed by a more gradual decrease with increasing depth to the limit of the measurement at $\sim$0.45 μm. The residual H concentration of more than 200 ppm at this depth is well in excess of bulk hydrogen analyses of Apollo 11 lunar materials, typically 50-100 ppm H (D'Amico et al., 1970; Epstein and Taylor,

1970; Friedman et al., 1970); however, the distribution has not yet begun to level off at this depth.

The measurement of the distribution was repeated twice on this sample. Each repetition showed a reduction in the H content of roughly twenty percent in the outer 0.2 μm and five percent between 0.2 μm and 0.4 μm deep as compared to the previous measurement of the distribution. Data from a remeasurement of the profile (third run) are plotted in Figure 7 to illustrate this gradual reduction in hydrogen content observed during the measurement of this sample as well as subsequent samples. This means, of course, that the measured profile is a slightly distorted representation of the initial distribution because the mobilization of the H due to the irradiation by the ^{19}F beam is continuously causing a slight modification of the distribution. However, similar profiles were obtained from several other lunar samples even though the sequence of beam energies chosen for the analysis was different for each sample. This indicates that the distortion is not great enough to change any of the essential features of the distribution, with the exception of the first few hundred angstroms. An increase in the H content within a few hundred angstroms of the surface has been observed on most samples following a few days of atmospheric exposure, but usually this surface H concentration is rapidly depleted during the first few minutes ($\sim 10^{14}$ ions/cm^2) of remeasurement with the ^{19}F beam. It is likely that this extremely mobile surface layer is primarily a very superficial H_2O contamination.

Sample 10085,31-12 was large enough to permit a relatively large (3.2-mm aperture) collimator to be used, allowing essentially all of the ^{19}F beam to illuminate the sample. The smaller size of the 10085,31-9 and 10085,1 fragments necessitated the use of smaller collimators with apertures of 2.4 mm and 2.0 mm respectively. A beam alignment problem encountered during the analysis of 10085,31-9 limits the usefulness of the data from this sample, but a definite enrichment in the H content of a layer roughly 0.2-0.3 μm deep was observed suggesting a profile with approximately the same shape, although with a much lower absolute H content, as the distribution measured on 10085,31-12. The H distribution obtained from the 10085,1 glass fragment (Fig. 8) also exhibits a similar depth dependence, with a total H content (in the 0.4 μm deep measured region) ∿1/3 as great as the value for 10085,31-12. The most obvious difference in the shapes of the distributions in Figures 7 and 8 (aside from the difference in absolute H content) is the much greater clarity with which the 10085,31-12 distribution shows a two-component shape due to the relative enhancement of the shallower, 0.02-μm deep component in the 10085,31-12 sample as compared to the somewhat flatter distribution in the 10085,1 sample.

Ultimately, it is the continuous mobilization of the H distribution which prevents the extension of these profile measurements to depths greater than ∿0.45 μm. Beyond this depth, the contribution of the 17.64 MeV (^{19}F energy) resonance in the $^{1}H(^{19}F,\alpha\gamma)^{16}O$ reaction becomes significant, and the relatively simple unfolding procedure

described in Section II of this thesis can only be used in cases where the profile is reasonably stable and reproducible. However, since the most interesting portion of the H distribution appears to consistently lie within the 0.45-μm range of the present measurements, it has not seemed necessary or fruitful to attempt to extend the measurements to greater depths.

A second sample allocation consisted of three Apollo 15 coarse fines. Handling and analysis procedures were the same as for the 10085 samples as described above. Sample 15413,5-2 is a 2 x 4-mm partially glazed pyroxene-rich crystalline rock fragment with a 1 x 3-mm area rich in pyroxene on one face. The sample was mounted, using a 2.4-mm aperture fused silica collimator, to expose this pyroxene-rich area to the ^{19}F beam. The H distribution measurement resulted in the profile shown in Figure 9. Once again there is a significant enhancement of H within about 0.2 μm of the surface. The shape of the profile is quite similar to the 10085 distributions, with an absolute H content comparable to that of the 10085,1 glass fragment.

Sample 15413,5-5 is a highly fractured fragment which appeared to be essentially all plagioclase. Due to its relatively small size, it was mounted using a 2.0-mm collimator. The usual analysis procedure resulted in a distribtuion which showed only a small enhancement of H, just barely above statistical uncertainties, in a layer again about 0.2 μm deep. In order to determine whether this apparent enhancement was due to a real, although small, H content

qualitatively similar to the distributions measured on the previous samples or merely the effect of statistical fluctuations, the counting statistics were improved by increasing the beam current to 50 nA and collecting 20 μC of beam charge per data point. The higher beam current is expected to cause a more rapid dissipation of the H content; nevertheless, the measurement resulted in a reproducible profile quite similar in shape to the distributions observed in 15413,5-2 and the 10085 samples, but at a concentration smaller by more than an order of magnitude than the H concentration over the same depth region in 10085,31-12.

Sample 15533,4-1 is a glass coated breccia fragment. The glass is probably a glaze rather than a splash glass. It is light but non-uniform in color and transparent in spots. The measured H distribution was quite flat with only a slight suggestion of an enhanced H content at ∿0.1 μm deep and a peak at zero depth corresponding to a small (∿5 x 10^{14} cm^{-2}) surface H concentration.

The profile obtained from these samples shows a wide variation in absolute hydrogen concentration, although the profile shapes are quite similar. The distribution measurements are summarized in the first part of Table 3. The limits shown on surface (zero-depth) concentrations pertain to the measured distributions. It is probable that somewhat larger surface concentrations may have existed prior to illumination with the ^{19}F beam. The total hydrogen content of a 0-0.4 μm deep region (excluding this surface concentration) is also given in units of 10^{15} H atoms/cm^2. The H contents

at depths of 0.1 μm and 0.4 μm are given in ppm H by weight. The measured profiles are also characterized by the depth x_p at which the peak H content is observed, and the full-width at half-maximum of the H distribution obtained by subtracting (in quadrature) the width of the resonance from the width of the peak in the measured excitation function. Since the uncertainties in the values given for the H content at various depths in a particular sample are affected by the aperture size of the fused silica collimator used with that sample, the aperture size is also indicated in Table 3.

The mobility of the H distributions observed in these lunar samples, especially in the outer 0.2 μm, is much greater than had been observed for the proton implantation profiles in feldspar, quartz, and fused silica test samples. One possible interpretation of this behavior is that we may be observing a distribution of terrestrial H_2O contamination absorbed into a porous surface region. Epstein and Taylor (1970) have shown that terrestrial H_2O exists in returned lunar soil samples in amounts comparable to their solar wind hydrogen content. Unless carefully cleaned, laboratory glass and other test samples exhibit a contamination hydrogen peak at zero depth but show no penetration of the surface, within the resolution of the measurement. However, this may not be true for the much more shocked and highly radiation-damaged lunar sample surfaces. A number of tests have been carried out to investigate this possibility. Samples 10085,31-12 and 15413,5-2 were subjected to a series of heating experiments with the idea that baking the

samples in a vacuum under certain conditions might drive off any superficial H_2O contamination without disturbing the implanted hydrogen. Both samples were baked for 100 hours at 150°C (simulating the conditions of lunar noon) at a vacuum of $\sim 10^{-9}$ Torr. Sample 10085,31-12 was subsequently baked for 24 hours at 290°C. Neither sample exhibited any significant change in the H distribution after baking. However, H_2O, apparently of terrestrial origin, is still retained in bulk lunar soil samples even at temperatures of 400-500°C (Epstein and Taylor, 1970).

The H distributions in three of the above samples (the 10085,1 fragment and samples 15413,5-5 and 15533,4-1) were remeasured after a prolonged storage period ($\sim$6 months) in a vacuum desiccator. All three samples had developed a relatively large ($\sim 10^{16}$ H atoms/cm^2) surface contamination, but this contamination appeared to be confined to the surface with little, if any, penetration beyond depths of a few hundred angstroms. Two of these samples (10085,1 and 15533,4-1) were also given an ultrasonic rinse in high-purity acetone with no observable change in the H distributions as a result of this treatment.

2. Apollo 15 glass-coated rocks 15015 and 15059

Samples were obtained from two Apollo 15 glass-coated breccias (rocks 15015 and 15059) sampled near the Lunar Module (LM) landing site. Sample handling procedures were modified to minimize contamination, especially from atmospheric H_2O. These rocks had been wrapped only in unsealed teflon bags before being placed in one of

the cloth sample collection bags for the return trip from the lunar surface. Hence they were exposed to atmospheric humidity in both the LM and Command Module (CSM) cabins and on earth prior to arrival at the LRL. LRL processing, however, is performed in a dry nitrogen atmosphere. The sealed sample containers received from the LRL were opened in our laboratory in a P_2O_5-dried, nitrogen-filled dry box and mounted in aluminum sample holders. These sample holders were then sealed in a clean vial and the vial was triply sealed using polyethylene bags and a second larger snap-cap vial. This package was then removed from the dry box and transferred to a polyethylene glove bag. The scattering chamber was then backfilled with dry nitrogen, the viewing window removed from the access port, and the mouth of the glove bag was clamped to the access port allowing the glove bag to inflate with dry nitrogen. After flushing the glove bag with dry N_2 gas for several minutes, the sample package was opened inside the nitrogen-filled glove bag and the sample holders installed in their mounts on the target wheel. The glove bag was then removed, the window immediately replaced and sealed, and the scattering chamber evacuated. This procedure eliminates any contact with water vapor, other than small residual amounts in the "dry" nitrogen gas, from the time the rocks were introduced into the LRL processing line.

The orientations of both rocks are well documented in lunar surface photography (Sutton et al., 1972). The 15015 samples (15015,39-1 and 15015,39-2) are adjacent surface chips from the lunar

bottom side of the rock. Samples 15059,32 and 15059,28 are surface glass chips from the top and bottom, respectively, of rock 15059. The lunar top surface of 15015 is heavily pitted, while there are no detectable microimpact pits on the bottom surface, suggesting that surface exposure has been primarily, possibly entirely, in one orientation (LRL, 1971). The microimpact pit density on the top surface of 15059 is very low indicating a short surface residence time. There are no detectable microimpact pits on the lunar bottom of 15059 (Hörz, 1971). Our own examination of samples 15015,39-2 and 15059,28 under a high power binocular microscope revealed no impact pits. Both samples are bubbly glass with some dust in cavities separated by smooth areas of a few millimeters square. Impact pits as small as ∿50 μm would have been easily observed on these smooth glass surfaces.

These samples were analyzed in the same manner as the Apollo 11 and 15 coarse fines; however, a glass collimator (3.2-mm aperture) was needed only for 15059,32 since the area of surface glass was large enough (0.2-0.5 cm^2) on the other samples to insure that only a negligible portion of the ^{19}F beam would be "spilled" on the aluminum holders.

The distributions obtained from the two 15015 chips are qualitatively similar (Figs. 10 and 11), but are not at all like those obtained from the coarse fine fragments discussed above. While the latter samples showed evidence of a surface H concentration which disappeared rapidly with illumination by the flourine beam, these

two rock chips displayed a larger and more persistent surface concentration (within about 200 Å below the surface) decreasing rapidly with depth to a flat distribution within 1500 Å of the surface for 15095,39-1 and 800 Å for 15015,39-2. It should be noted that for 15015,39-2 the dimensions of the beam spot were increased to more than double the usual size (2-3 mm). Consequently, the beam current density was decreased to less than half the normal value. (Beam current was not changed.) The accompanying reduction in local heating of the target by the beam may partially account for the relative stability of the H distribution on this sample.

The two chips from rock 15059 exhibited the same type of H distribution as was observed on the 15015 samples, concentrated mainly within a few hundred angstroms of the surface (Fig. 12). The chip from the top of the rock (15059,32) appeared to show somewhat greater penetration of the H distribution than the sample from the bottom surface (15059,28) reaching as far as 0.25-0.30 μm before decreasing to the same level as the flatter 15059,28 distribution. However, the amount of excess hydrogen in the region 0.05-0.30 μm of 15059,32 when compared to 15059,28 is only $\sim 10^{15}$ atoms per cm^2, indicating no strong solar wind excess in the top sample.

The 15015 samples were turned over (under dry nitrogen) to measure the H distribution on the <u>interior</u> rock surfaces. These surfaces were created in the process of breaking the samples from the parent rock and thus have never been exposed on the lunar surface. Since the chipping procedure was performed after introduction into

the LRL processing line, these surfaces have received no exposure to atmospheric humidity, but only to dry (20-50 ppm H_2O) nitrogen. The slightly smaller ($\sim 2 \times 10^{15}$ atoms/cm^2), more superficial surface H concentrations detected on each of these samples must be interpreted as contamination, probably H_2O, even though these surfaces were exposed only to a dry nitrogen atmosphere. While the measured distributions for the lunar exterior surface glass coatings are not inconsistent with a relatively unmodified solar wind proton implantation profile (with a mean penetration depth of $\sim$200 Å), it must be concluded that at least a significant portion (if not all) of the H concentrations observed on these surfaces (within the resolution of $\sim$200 Å) is due to H_2O contamination.

Data from these samples are also summarized in Table 3. The small ($\sim$40 ppm) H contents observed in the interior rock faces can be taken to represent the volume H content of the rock, since the flux of solar flare protons with sufficient energy to penetrate to these depths (several millimeters below the surface) is a negligible effect and since we have no evidence that H_2O contamination can penetrate a fresh, undamaged silicate surface to depths greater than a few hundred angstroms.

Each of the 15015 samples was removed from the scattering chamber and exposed to the laboratory atmosphere for at least 24 hours. Remeasurement showed no significant change in the H distributions in the lunar exterior surfaces. However, the initial exposure of these rocks to the LM cabin atmosphere may have saturated

an active surface layer so that subsequent exposure would produce no additional contamination.

With a solar wind proton flux of 6×10^{15} per cm^2 per year, the time necessary to accumulate the <u>total</u> H contents observed in the outer 0.4 μm of these glass-coated samples is on the order of only one year, implying that either these samples have all had extremely short exposure times or the implanted H has been essentially totally lost. In order to determine whether keV protons implanted in the lunar glass should be expected to be retained, the glass coating of 15015,39-2 was implanted with a dose of 2×10^{16} protons per cm^2 at an energy of ∿12 keV. The resulting H distribution was quite similar to the distributions obtained by implanting fused silica and crystalline silicate targets under similar conditions (see Section II, Part D), with quantitative retention verified within the uncertainties of the measurement. The artificially implanted distribution did not exhibit the high mobility under irradiation with the ^{19}F beam characteristic of the H distributions at similar depths in the 10085 and 15413 samples, but behaved in a similar manner to the distributions implanted into terrestrial silicate samples. This implies that the differences in the mobility of the H distributions in the 10085 and 15413 samples as compared with the artificially implanted distributions are probably not the result of bulk physical or chemical differences between the materials in question.

3. Apollo 16 glass-coated rocks 64455 and 65315

Rock 64455 is a heavily pitted ellipsoidal glass-coated feldspar-rich crystalline rock (Grieve and Plant, 1973). Sample 64455,24 is a 1-cm chip of the glass coating from the rock's western edge adjacent to an exposed patch of light-colored rock. Sample 64455,33 consists of two similar $\frac{1}{2}$ cm surface chips taken from this light-colored area.

Rock 65315 is described as friable white anorthosite with patches of relatively thick black glass coatings (LRL, 1973). These patches appear to be remnants of a more extensive glass coating which has been chipped away by repeated impacts to expose the underlying rock. The lunar top and northern faces are the most obviously pitted, but pits may also be present on the bottom face near the northern edge and on the southern face (LRL, 1973). The 65315,6 and 65315,20 chips are 1 cm and $\frac{1}{2}$cm samples of the patches of black glass coating from the southern and top faces of the rock, respectively. 65315,8 is a $1\frac{1}{2}$cm chip of the white anorthosite sampled adjacent to the 65315,20 glass chip on the lunar top of the rock.

In obtaining samples of glass and crystalline material from the same rock, our primary objective was to investigate whether the crystalline state of the medium would have any significant effects on the retention of implanted solar wind ions. However, prompted by a suggestion from A. Turkevich (1973), it was decided to measure fluorine depth distributions on these samples as well. The in situ chemical analysis of lunar highlands material performed by the

Surveyor 7 alpha-particle scattering experiment revealed a surprisingly high fluorine content (0.26 ± 0.11 percent F by weight) in two soil samples (Patterson et al., 1970). Somewhat less fluorine (0.07 ± .2 percent) was detected in a rock analysis although statistical uncertainties were quite large. Analyses of returned lunar soils have not shown such high fluorine contents, suggesting that fluorine may have been concentrated in micron-thick layers at the surface of the Surveyor 7 samples. Turkevich suggested that this fluorine could be the result of volcanic exhalations or gases from impact volatilization depositing on the surfaces of soil grains, and that the analysis technique using the $^{19}F(p,\alpha\gamma)^{16}O$ reaction could be used to investigate this possibility. Solar wind implantation could be considered as an alternative, although less likely, source. Since the Apollo 16 site was in a lunar highlands area geologically similar to the Surveyor 7 site, the Apollo 16 samples presented a good opportunity to look for surface fluorine enhancements.

The atmospheric exposure and sample handling history of the 64455 and 65315 samples was virtually unchanged from the description given above for the 15015 and 15059 samples. The H distributions were measured first on the 64455 samples with the results shown in Figures 13 and 14. The "exterior surface" data are measurements on the lunar exterior faces of the samples. As observed previously, the H in the first few hundred angstroms is rather labile, while the relatively small H contents at greater depths are much more stable. The 64455 distributions are all characterized by a maximum within two

or three hundred angstroms of the surface, similar to the profiles measured on the 15015 and 15059 samples. There is apparently no significant difference between the glass sample (64455,24) and the rock samples (64455,33). the interior samples all show a concentration of hydrogen within a few hundred angstroms of the surface which is systematically lower, although by less than a factor of two, than on the corresponding lunar exterior surface. For 64455,33-1 the H concentration remains higher in the exterior sample to a depth of at least 0.4 μm, while for 64455,33-2 and the 64455,24 glass, the exterior sample shows no excess below about 0.2 μm compared to the interior samples.

Once again, the relatively large H concentrations observed within a few hundred angstroms of the surfaces of the interior samples must be interpreted as terrestrial contamination since these surfaces were freshly created in chipping the samples from the rock in the LRL processing line. These surfaces have been exposed only to dry nitrogen, providing additional support for the conclusion, made as a result of similar observations on the 15015 and 15059 samples, that even the small residual H_2O content of the "dry" nitrogen is sufficient to significantly contaminate these surfaces.

All of the 64455 samples as well as the 15015 and 15059 samples, both interior and exterior, show an H content of ∿20-50 ppm by weight at depths of 0.2-0.4 μm. Although relatively small, these concentrations are distinctly above background. (Compare with the counting rates for depths below zero in Figures 12-14). For the

exterior samples, inward diffusion of solar wind hydrogen or direct implantation of 10-100 keV protons are possible sources; however, these cannot explain the results for the interior samples unless diffusion has extended essentially throughout the volume of the rock. It appears more reasonable to conclude that we are observing either indigenous lunar H or "inherited" solar wind hydrogen which was present in the materials from which 64455 was formed.

Following the measurement of the H profiles, a 30-nA proton beam was used to measure ^{19}F depth distributions. It should be noted that the penetration depths of the 16-18 MeV ^{19}F ions used in the H analysis ($\sim$8 μm) are well beyond the 1-μm range of these F distribution measurements and hence should not be expected to contribute to the measured F contents of this 1-μm layer.

The results of ^{19}F depth profile measurements on the 64455 samples are shown in Figures 15 and 16. The 64455,24 glass sample showed a fluorine-rich zone at an apparent depth of 0.35 μm and a width of $\sim$0.2 μm. Scanning the proton beam across the surface of the sample showed that this fluorine-rich zone is apparently not parallel to the surface, although the profile was not measured in detail for each beam position. The 64455,33-1 sample showed a peak within 0.1 μm of the surface, but this peak was not reproduced in the "second run" data. For this remeasurement the peak had apparently shifted inward to 0.1-0.15 μm deep. This apparent shift could be interpreted as a volatilization of fluorine from the surface due to irradiation with the proton beam, but it could also be due to a build-up of an

electrostatic charge on the silicate sample as the irradiation progressed. A surface potential of a few kilovolts would slow down the incident protons enough to cause a significant difference between the measured beam energy of the protons as they strike the sample. (In the calculation of the depth scale, it is assumed that this difference is negligible.) Since the average surface potential on the sample necessary to cause an apparent inward shift of 0.1 μm is 5.5 kV, this explanation does not seem unreasonable. The charging of a 1.5-cm diameter fused silica disc was measured by observing the shift in beam energy (relative to the resonance energy) necessary to obtain the maximum counting rate from a thin (5 $\mu g/cm^2$) evaporated CaF_2 surface coating. The average potential was determined to be 10 kV with fluctuations of ±5 kV, implying a magnitude for this charging effect on the 64455,33-1 sample (probably somewhat smaller than for the fused silica target) in reasonable agreement with the observed shift in the peak of the F distribution. (This effect is not important for the hydrogen measurements since the apparent inward shift of the H distribution resulting from a 10 kV surface potential is less than the resolution of ∿200 Å.) It would appear more difficult to ascribe the peak in the measured 64455,24 F distribution to a surface (zero-depth) concentration of F, since this would require an average surface potential of ∿20 kV for this sample. Although this seems unreasonably high, the possibility cannot be ruled out at this time.

Data for the lunar exterior surface of 64455,33-2, although incomplete, show no fluorine enhancement above a constant level of

∿50 ppm applicable to all three 64455 exterior samples. The interior surfaces of these samples also showed relatively uniform F distributions, except for small concentrations within ∿500 Å of the surface, with the 64455,33-2 interior having a relatively high F content of ∿100 ppm. The fluorine data for these samples are summarized in Table 4, giving the apparent depth and width (FWHM) of the peak in the distribution and the total F content in the 0-0.5 μm and 0.5-1.0 μm deep regions. The H distribution data are again summarized in Table 3.

For the 65315 samples, F distributions were measured first to eliminate the remote possibility that a portion of the observed F content could be due to ^{19}F ions implanted during the H measurements migrating out to within 1 μm of the surface. An additional procedure involving measurement of the yield of 11-MeV γ rays from $^{27}Al(p,\gamma)^{28}Si$ near the 992-keV (proton energy) resonance was also introduced. This reaction, although much weaker than $^{19}F(p,\alpha\gamma)^{16}O$, produces most of the counting background for the F analysis measurements due to the relatively high Al content of the lunar samples. If the Al content is reasonably uniform in a ∿1-μm surface layer, a step in the 11-Mev γ-ray yield is observed as the proton energy is increased past the 992-keV resonance. Any observable shift in the location of this step can be attributed to charging of the silicate sample, assuming that thin (∿0.1 μm), Al-free coatings can be ruled out. If a significant surface potential exists during the F distribution measurements, it should be detected by this procedure since the experimental conditions are identical, except for a ten percent difference in the proton beam energy.

Measurement of the F distribution in the 65315,6 glass chip revealed a much larger F content (Fig. 17) than was observed in the 64455 samples. An upper limit of ∿5 kV can be placed on the surface potential during irradiation as a result of the $^{27}Al(p,\gamma)^{28}Si$ measurement described above; however, this limit is not strong enough to rule out the possibility that the observed peak is actually a surface (zero-depth) concentration apparently shifted to a depth of 0.1 μm by a surface potential of ∿5 kV. The peak concentration corresponds to ∿2000 ppm F, with an average over the outer 0.5-μm layer of ∿1000 ppm. A remeasurement of the distribution resulted in an apparent decrease in the F content of this depth region by about a factor of 2, implying that F may have been volatilized by the proton beam. This discrepancy could also be due to a shift in the position of the beam spot on the sample, if large local variations in F content exist over the surface of the sample. However, a scan across the sample revealed no areas with a large enough F content to reproduce the original measurement.

The lunar interior side of this sample contained little F -- about an order of magnitude less than the exterior surface. The interior surface analyzed was mostly glass with small patches of white anorthosite.

Interior and exterior surfaces of the 65315,20 glass chip were also analyzed for F, as well as an interior face of the white anorthosite chip 65315,8. These surfaces contained only small amounts of F, compared with the 65315,6 exterior glass surface. However, the

near-surface enrichments of $\sim 10^{15}$ F atoms/cm^2 observed on the interior faces of both of these samples indicated that they have most likely been subjected to some form of terrestrial F contamination. Contamination with F has not been observed on any of the fused silica or other test samples or on fresh interior surfaces of chondritic meteorites prepared in this laboratory. It can be concluded from this observation that either the lunar samples (both exterior and interior surfaces) have an exceptional affinity for some unidentified form of F contaminant associated with the sample handling procedures used in this study for the lunar, meteoritic, and terrestrial samples alike; or the contamination is introduced in the LRL processing line. A likely source is the freon used to clean the tools, work areas, and containers used on the Apollo missions and at the LRL. The teflon bags in which samples are packaged and sealed are another possible source of F contamination.

The F data for these 65315 samples are again summarized in Table 4. H distributions were also measured and the data summarized in Table 3. Although the data for both exterior glass samples (65315,6 and 65315,20) show significant penetration of the H to depths up to ~ 0.3 μm, the prior irradiations to measure F distributions may have significantly depleted the original H content of these samples, rendering the measured profiles less accurate representations of the initial distributions than if the H measurements had been performed first. The large size of the 65315,8 sample prohibits mounting of the sample with the present sample holders to

irradiate the lunar exterior surface. Rather than break the sample into smaller pieces, it was decided to store this sample until it could be mounted in a new, larger scattering chamber.

4. Apollo 16 ALSRC samples

For a relatively small fraction of the returned lunar samples, the atmospheric exposure in the LM and CSM cabins and on Earth prior to introduction into the LRL processing line has been avoided by sealing the samples in an indium-sealed aluminum vacuum container (ALSRC) on the lunar surface. Thus, although these samples are still subject to possible H_2O contamination from the astronauts' cooling systems on the lunar surface and from the residual H_2O content of the "dry" nitrogen gas to which they are subsequently exposed, exposure to normal atmospheric humidity is eliminated as a source of H_2O contamination.

Four Apollo 16 samples returned in one of these vacuum-sealed sample containers were obtained for this study. Three of these (66044,8; 68124,3; and 68124,10) are 4-10 mm coarse fines and the fourth (68815,27) is a chip from a large breccia boulder. The sample handling procedures used are the same as those initiated with the 15015 samples, avoiding any exposure to the laboratory atmosphere.

Rock 68815 is a glassy, dark-matrix, dark-clast breccia in the classification of Wilshire et al. (1973). Track gradients, rare gas spallation ages, and microimpact pit densities give a concordant exposure age of $\sim 2 \times 10^6$ years for this rock, which is itself a chip

from the top of a large boulder (Behrmann et al., 1973). Sample 68815,27 is a surface chip with an exposed 2-mm × 4-mm light-colored region surrounded by darker gray material. A thin section prepared from small chips of the sample showed that the dark gray material was a very fine-grained matrix, perhaps devitrified glass, and the light-colored material was mostly crystalline plagioclase. The H distribution measured on this sample (Fig. 18), characterized by a broad peak extending to ∿0.2 μm followed by a more gradual decrease in the H concentration with increasing depth, is qualitatively quite similar to the distributions measured in the Apollo 11 and 15 coarse fines, most notably 10085,31-12; 10085,1 and 15413,5-2. The total H content of 2.3×10^{16} atoms per cm^2 is second only to the 5.5×10^{16} per cm^2 observed in the 10085,31-12 brown glass fragment. The lunar interior surface shows only a superficial surface H concentration, similar to the distributions measured on the interior surfaces of the other lunar rock chips, in addition to a uniform H content of only ∿20 ppm in the 0.4-μm deep measured region.

Figure 19 illustrates the evolution of the distribution in 68815,27 during the irradiation with the ^{19}F beam. Three successive data runs are presented with individual data points for a given run connected by straight line segments, except at the peak where a somewhat arbitrary curve has been drawn to estimate its shape. Despite the low beam current density (< 10^{14} ions/cm^2 in about 10 minutes for each data point), the H content is significantly reduced for each successive measurement. A slight suggestion of a shoulder in the

profile at ∿0.3 μm in the first run has evolved into a definite second peak by the third run. The slope changes more abruptly at a progressively shallower point from run to run, suggesting that the first peak represents a relatively loosely bound H component superimposed on a deeper, broader, more tightly bound distribution. This is the same sort of evolution of the profile under bombardment observed on Apollo 11 and 15 coarse fine samples.

The light-colored region on the lunar exterior surface of 68815,27 is predominantly feldspar, so a significant fraction of the exposed material (possibly beneath a thin metamictized layer) is crystalline. A scan across the surface of 68815,27 showed no significant variation in the H content below ∿0.1 μm, indicating no observable difference in the H distribution between the feldspar and the glass matrix.

Using a similar technique employing a resonance in the reaction $^{1}H(^{7}Li,\gamma)^{8}Be$ (Padawer and Schneid, 1969), a research group at Grumman Aerospace Corporation has also detected a concentration of H within ∿0.4 μm of the surface of a sample from rock 68815 (Padawer, 1973; Stauber et al., 1973). The sample subjected to this analysis (68815,25) was quite similar to 68815,27 in that a light-colored clast was embedded in the analyzed exterior surface. Since this technique is only ∿6 percent as sensitive (in terms of counts per incident ion per ppm H) as the $^{1}H(^{19}F,\alpha\gamma)^{16}O$ technique, in addition to having a poorer depth resolution (by a factor of ∿6), statistical uncertainties and resolution limitations permit only qualitative

comparisons with the results of this study. Over the same depth range, the $^{1}H(^{7}Li,\gamma)^{8}Be$ data (5 data points) are not inconsistent with the 68815,27 profile measured in this study, however the measured H content is lower by a factor of ∿3 relative to the 68815,27 results. Although variations of this magnitude across the surface of rock 68815 are not unreasonable, it is probable that the H content of 68815,25 prior to the ^{7}Li irradiation was somewhat higher than the measurements indicate. The mobility of the distributions observed in the present study may be greatly magnified by the much higher ion fluxes and total doses per data point used by Stauber et al. The analyzed area of 68815,25 sustained a power density input of ∿10 watts/cm^2 (Stauber et al., 1973), while the analysis of 68815,27 in the present study involved only ∿0.5 watt/cm^2.

Stauber et al. also subjected a splash-glass chip from rock 61016 (61016,135) to the $^{1}H(^{7}Li,\gamma)^{8}Be$ analysis. A rather large (∿2 × 10^{16} atoms/cm^2) concentration of H was observed within ∿0.1 μm of the surface, with an H content of 100-200 ppm from ∿0.1 μm to ∿2 μm deep.

The three coarse fine samples from the Apollo 16 ALSRC obtained for this study consisted of two crystalline anorthosite fragments (66044,8 and 68124,10) and a dark brown glass spherule (68124,3). Two opposite surfaces were analyzed on each sample. Surface A on each sample was analyzed for fluorine before performing the H distribution measurements, while the H analysis was done first on the B surface.

Sample 66144,8 is a 5-mm blocky anorthosite fragment. Surface A includes a 1-mm^2 gray area which may be glass, while surface B appears to be essentially all anorthosite. The sample was mounted using a 3.2-mm glass collimator. Neither surface revealed an H distribution which was remarkable in any way. A superficial surface H concentration of $\sim 2 \times 10^{15}$ per cm^2 on B was not observed on A; however, the previous irradiation of surface A for F analysis probably dissipated any superficial surface H from this surface. Only slight enhancements of the H content at depths greater than $\sim$0.1 μm were observed on these surfaces.

Surface A of 68124,3, a 5-mm glass spherule, appeared to be quite smooth, while several small pits could be seen in a cursory inspection of surface B. The H profiles measured on these two opposite surfaces are virtually identical, and quite similar to the data shown in Figure 18 for the 68815,27 interior surface. Similar results were obtained for the two analyzed surfaces of 68124,10, a 5-mm × 7-mm anorthosite fragment. The only notable difference in the H analysis for the 68124 samples is the slightly higher uniform H content in the 0.4-μm deep measured region for 68124,10 (30 ppm) as compared with 68124,3 (10 ppm).

Figure 20 shows the F distributions measured on both exterior and interior surfaces of 68815,27. The dominant feature is a narrow ($\lesssim$ 0.1 μm) peak $\sim$0.15 μm deep with a tail extending to 0.8 μm deep in the exterior sample. Moving the proton beam across the surface indicated that this sharp peak apparently has a sizeable ($\geq$ 1 mm)

lateral extent at a relatively constant magnitude. This thin F-rich layer may be a surface (zero-depth) F concentration which appears to be shifted inward due to a surface potential of several kilovolts, as discussed earlier. The excellent reproducibility of this distribution (data from two consecutive energy scans are plotted in Figure 20), requiring an extremely stable surface potential, makes this interpretation appear somewhat unlikely. However, the $^{27}Al(p,\gamma)^{28}Si$ measurement was not performed on this sample, so no definite conclusions can be made concerning the extent of the charging effect.

Contamination appears to be a problem with fluorine even with samples from the sealed sample container. The F profile for the 68815,27 interior has a peak within 0.1 μm of the surface. Further, a remeasurement of this distribution after an interval of about one week resulted in an observed F content twice as large as in the original measurement shown here. During this interval the sample remained undisturbed in the scattering chamber and was exposed only to dry nitrogen gas (for ∿2 hours) and a vacuum of $\sim 10^{-9}$ Torr. The 64455 samples, however, showed little change over this same period. No H contamination accompanied this increase in F content. The source of the apparent contamination has not been identified; however, it may be that this apparent increase is due to large local variations in F concentration from prior contamination, with an area of higher F contamination, not within the beam spot for the first analysis, illuminated during the remeasurement.

An exceptionally high F content was observed on 66044,8-B,

averaging nearly 2000 ppm F in a layer 0.5 μm deep (Figure 21). High F contents (1400 ppm) continue into the sample to at least 1.0 μm deep. An intentional shift in the position of the beam spot on the sample shows a significant variation in the F distribution, but the distribution measured on a particular spot appears to be reasonably stable under continual bombardment. 66044,8-A contains somewhat less F than the 66044,8-B surface, but the 820 ppm F within 0.5 μm of the surface is still quite high compared with most of the other samples listed in Table 4. Although the peak F concentration in 66044,8-A appears to be located at a somewhat greater depth than in 66044,8-B (0.10 μm compared with 0.03 μm), this difference can be explained entirely by the surface potentials measured using the 992 keV resonance in $^{27}Al(p,\gamma)^{28}Si$ and interpreting the peaks as true surface (zero-depth) concentrations. Average potentials of 7 ± 3 kV and 2 ± 2 kV were measured for surfaces A and B respectively, as shown in Figure 22. The sharper step observed for surface B indicates that fluctuations about the average potential were not as great as for surface B. The resonance width is only ∿0.1 keV; however, the estimated energy spread of the incident proton beam (∿1 keV) makes a significant contribution to the width of the step observed for 66044,8-B. Although additional broadening could be caused by a large depletion of Al within a few hundred angstroms of the surface in a particular sample, this alternative appears quite unlikely. Thus, additional broadening beyond that due to the energy spread of the proton beam must be interpreted as due to kilovolt fluctuations in the surface potential

on the sample during irradiation with the proton beam. Although the most likely interpretation for the peaks in the F distribution appears to be surface contamination, the large (1400 ppm) amounts of F observed below this surface concentration on 66044,8-B must be interpreted as an exceptionally large volume concentration of F. It is unlikely that such large amounts of terrestrial F contamination could penetrate so deeply (up to at least 1.0 μm), especially considering the lack of a penetrating tail on the surface peak. Consequently, the best interpretation for the observed large concentration of F in the outer micron of the 66044,8-B surface is that it is lunar F. However, a small particle of teflon lodged on this surface could conceivably account for these results.

The F distributions measured on the two opposite surfaces of 68124,3, the glass spherule, are qualitatively quite similar (Fig. 23); however, the amounts differ by about a factor of two. The apparent depth (~0.1 μm) of the peak F concentration can be explained entirely by interpreting the peak as a surface concentration with an apparent inward shift of more than 0.1 μm due to the surface potentials measured using $^{27}Al(p,\gamma)^{28}Si$ (see Figure 22).

For sample 68124,10, comparatively little F was observed in either face, but small peaks were observed in both. The apparent 0.17-μm depth of the peak in 68124,10-B can again be explained by the surface potential due to charging inferred from the $^{27}Al(p,\gamma)^{28}Si$ measurement (although insufficient data make the 14 kV estimate highly uncertain), interpreting the peak as a surface concentration. The

surface potential determination was not performed for 68124,10-A; however, the apparent 0.09 μm depth of the peak could easily be explained by shifting of a surface concentration due to a potential of ∿5 kV.

5. Simulation experiments

Borg et al. (1971) have observed metamictized coatings (rendered amorphous by radiation damage) 200-1000 Å thick on lunar soil grains by high voltage electron microscopy. Although the boundary between the amorphous layer and the underlying crystalline grain generally appears quite sharp, high nuclear particle track densities ($> 10^{11}$ tracks/cm^2) indicate that radiation damage may still be quite severe (but below saturation levels) to depths of a few tenths of a micron. If this type of radiation damage can render a silicate material porous to water, then the deep (∿0.2 μm) H concentrations observed in several of the lunar samples, most notably 10085,31-12 and 68815,27, might be explained as terrestrial H_2O contamination penetrating the surface of the lunar sample to the limit of the porous region.

In order to check the possibly greater extent of H_2O penetration into heavily radiation damaged silicate materials relative to undamaged samples, a set of fused silica samples was first baked at 300° C in vacuum to drive off surface contaminants and then irradiated with 86 keV ^{16}O ions. The irradiation doses of 2×10^{16} to 1.4×10^{17} ions/cm^2 (into a $\frac{1}{2}$ cm^2 area) should be more than enough

to damage a layer 0.20-0.30 μm deep to saturation (Hines and Arndt, 1960; Winterbon et al., 1970). Some of the artificially damaged fused silica surfaces were exposed to H_2O and then subjected to H distribution measurements. One set of irradiated samples was exposed to H_2O in vapor form only (laboratory atmospheric humidity for ∿1 week) and a second set was given a 24-hour exposure to distilled H_2O in addition to atmospheric exposure. A third set was kept under vacuum, except for a two-hour exposure to dry N_2 gas. Unirradiated samples were included with each set as controls.

Results of the subsequent H distribution measurements indicate that a small amount of H_2O (10^{15} to 2×10^{15} H atoms/cm^2) has penetrated to depths of up to 0.10 μm (Fig. 24) in all of the irradiated samples exposed to water in either liquid or vapor form. The distributions are similar to the H profiles measured on the 15015, 15059, and 64455 lunar samples, except the concentrations are smaller by less than a factor of 2 than the surface concentrations on these lunar samples and drop to zero by ∿0.10 μm deep in even the most heavily irradiated samples. The depth of the H_2O penetration is not comparable to the expected extent of the damage saturated region; however, scanning laterally across the irradiated samples indicated that penetration of the H_2O had occurred mainly in the area irradiated by the ^{16}O beam. The samples exposed only to dry N_2 for a short time showed no surface H_2O ($\lesssim 10^{14}$ H atoms/cm^2).

These results provide additional evidence for the identification of the near-surface H concentrations in 15015, 15059, and

64455 lunar samples as terrestrial H_2O. It seems improbable, in this light, that the large 0.2-μm deep concentrations on 68815,27 and some of the Apollo 11 and 15 coarse fines could be terrestrial H_2O.

6. Apollo 16 LSCRE foil

The hydrogen distribution was measured on both sides of an aluminum-coated platinum foil from the Apollo 16 Lunar Surface Cosmic Ray Experiment (LSCRE). The side with the aluminum coating (~0.1 μm thick) had been exposed to the April 18, 1972 solar flare event, which lasted for the first half of the mission. Both sides showed a large concentration of hydrogen within ~200 Å of the surface -- about 6×10^{16} per cm^2 for the exposed side and 3×10^{16} per cm^2 for the other side. This difference could be due partially to the solar flare exposure, but unequal surface contamination should be expected, especially considering that the two surfaces are of different metals. There is no evidence of any implanted hydrogen above that from H contamination, but, using the H observed at depths greater than 0.1 μm, an upper limit can be set on the exposure to 10-40 keV protons if one assumes that all such particles are retained in the platinum at the end of their range. The γ-ray yield is quite flat over the ^{19}F energy range corresponding to the implantation depths for 10-40 keV protons. Assuming that the difference in yield between the two sides of the foil over this range is due entirely to implanted solar flare protons, the implied integrated flux of protons in the 10-40 keV range

is 10^{15} per cm^2. At least part of the difference, however, can be attributed to the off-resonance yield from the higher surface concentration of hydrogen on the exposed side. So at best we obtain an upper limit of about 10^{15} protons per cm^2. This limit is questionable, however, due to the doubtful assumption that all implanted protons are retained at the end of their range. An artificial implantation of 20-keV protons was performed to test this assumption and resulted in about 40% retention at the implantation depth when the distribution was measured several hours after the implantation. Under illumination by the ^{19}F beam, however, the diffusion process was much more rapid than had been observed in implanted glass samples, so the effects of diffusion during the measurement of the distribution may have led to considerable losses of implanted H.

Data from the Apollo 16 Lunar Surface Cosmic Ray Experiment (Burnett et al., 1973) imply that if an inverse cubic proton energy spectrum is extrapolated from the MeV range down to 10 keV or lower, the integrated flux of 10-40 keV protons on the piece of aluminum-coated platinum foil should have exceeded $10^{16}/cm^2$. The upper limit of $10^{15}/cm^2$ suggests that the spectrum diverges from an inverse cubic behavior at an energy somewhat higher than 10 keV. Our implantation results, however, suggest that the retention of the solar flare protons at depths corresponding to 10-40 keV proton ranges may have been poor. Consequently, the above conclusion on the energy spectrun cannot be strongly defended.

B. Discussion

1. Depth distributions of H in lunar samples

In summary, three major features have been observed in the H distributions of one or another of the lunar samples analyzed in this study: (1) a narrow concentration peaking within ∿200 Å of the surface, (2) a broad distribution extending from the surface to ∿0.20 μm deep, and (3) a still broader distribution apparently peaking at ∿0.25 μm and extending at least to a depth of 0.45 μm. These features can coexist in a given sample, with (3) appearing as a shoulder on the tail of (2) followed by a more gradual decrease in H content with increasing depth. Samples 10085,31-12 (Fig. 7) and 68815,27 (Figs. 18 and 19) show these deeper features most clearly, while the 64455 samples (Figs. 13 and 14) exhibit typical narrow surface (within a few hundred angstroms) concentrations. The observation of this same feature on the "interior surfaces" of the lunar rock samples is the primary basis for the interpretation of this type of distribution as terrestrial contamination, probably H_2O. The consistently higher (except for 65315,20) surface H concentrations on the exterior surfaces compared to the interior surfaces, although possibly due to small amounts of implanted solar wind H, can be satisfactorily explained by a greater affinity for H_2O resulting from solar wind radiation damage even apart from the more extensive exposure to terrestrial H_2O experienced by the exterior surfaces.

Cadenhead et al. (1972) point out that a typical gas will achieve monolayer coverage in seconds even at pressures as low as

10^{-6} Torr. Hence, the observation of approximate H_2O monolayer equivalents ($\sim 2 \times 10^{15}$ H atoms/cm^2) on the surfaces of samples from the sealed rock box (ALSRC), which have been exposed to "dry" nitrogen (20-50 ppm H_2O), although not to room atmosphere, is not remarkable. The distributions observed on the interior surfaces of the lunar rock samples, which are almost certainly due to terrestrial H_2O contamination, are all consistent with coverage in the monolayer region. (Compare the calculated appearance of an H_2O monolayer shown in Figs. 13 and 14.) Thus, it should be expected that coverage (physisorption) in the monolayer region should have taken place on the exterior surfaces as well. Water vapor adsorption studies (Cadenhead et al., 1973; Cadenhead et al., 1972; Fuller et al., 1971) imply that a brief exposure to air results in an irreversible adsorption of water vapor onto previously pristine lunar sample surfaces. This irreversible adsorption is interpreted as a chemisorption since temperatures above 300°C are required to release the adsorbed H_2O; however, the extent of the chemisroption also appears to be limited to about a monolayer equivalent, implying that the chemisorption does not significantly penetrate more than a few atomic layers. Fuller et al. (1971) find no evidence of inherent porosity in the 500-Å thick metamict coatings on lunar dust grains observed by Borg et al. (1971). Hence, the somewhat larger, more strongly bound surface H concentrations observed on the exterior surfaces of rocks 15015, 15059 and 64455 as compared to interior rock surfaces can be interpreted as H_2O chemisorbed by a surface layer rendered

significantly more reactive than the fresh interior surfaces as a result of solar wind exposure. (Some other effect of the reducing environment of the lunar surface may be necessary to explain the apparent chemisorption on samples from the unpitted bottoms of rocks 15015 and 15059 if, indeed, these samples have had no solar wind exposure.) A physisorbed coverage comparable to that observed on the interior surfaces is probably superimposed on the more strongly bound chemisorbed component. This interpretation is supported by the results of the tests performed in this study to simulate the surface conditions due to radiation damage from ions of keV energies. Although the irradiations of fused silica samples with 5.4 keV/amu ^{16}O ions are expected to cause severe radiation damage over a depth range of ~0.25 μm, exposure to atmosphere resulted in an adsorption of H_2O in monolayer quantities with penetration confined essentially to a region 0-500 Å deep. Only slight evidence of penetration to a depth of 0.1 μm was observed. The observed H concentrations were somewhat larger and more strongly bound on the irradiated samples exposed to H_2O than on samples which had not been irradiated. (A similar observation has already been made concerning the H distributions on exterior surfaces of lunar rocks as compared to fresh interior surfaces.) A chemisorption has apparently occurred on these simulated surfaces as well as the actual lunar sample surfaces; however, the penetration of the chemisorbed H_2O does not agree with the radiation damage range of the ^{16}O ions. This suggests that whatever chemical alteration of the samples is

involved, it is essentially a surface effect of the irradiation, rather than a volume effect. A likely candidate is sputtering. The surfaces of lunar samples have been described as non-stochiometric and oxygen-deficient (Gammage and Becker,1971; Epstein and Taylor, 1971) and this reduced state has been attributed, in part, to fractional vaporization (by solar wind sputtering and/or impact volatilization) of oxygen relative to heavier atoms. This effect has probably also depleted the surfaces of the irradiated fused silica samples in O relative to Si (while an oxygen excess results at greater depth due to the use of ^{16}O in the irradiation). The chemisorption of H_2O, then, may be part of an oxidation process in which stochiometry is at least partially restored to the surface region from which the sputtered atoms were removed. The lack of a strongly bound surface H concentration on the 10085, 15413 and 15533 samples, which had been exposed to room atmosphere for a few months prior to analysis, may be the result of this oxidation process going to completion with the release of the H in the form of H_2 gas. For the 65315 samples, the prior irradiation (for F analysis) was probably sufficient to dissipate any surface H concentration. However, the 68124 samples also appeared to lack a strongly bound surface H component, since the small (10^{15} H/cm^2) surface concentrations dissipated rapidly on illumination with the ^{19}F beam. This provides an encouraging suggestion that perhaps the "dry" N_2 gas to which these samples were exposed has a low enough water content to prevent a significant chemisorption of H_2O.

The deeper features ($\gtrsim$500 Å deep) observed in the H distributions of the 68815,27 rock sample, the three 10085 glass fragments, and the 15413,5-2 rock fragment (and to a lesser extent in a few other samples) are almost certainly the result, either directly or indirectly, of exposure to solar radiation; although it is not clear exactly how these features are related to the irradiation history of these surfaces. Four possibilities will be considered here: (1) adsorption of a terrestrial contaminant (H_2O) by a region which has been heavily damaged by solar radiation, (2) an inward bulk volume diffusion of solar wind H, perhaps reaching an equilibrium with the surface erosion rate, (3) population of a distribution of radiation damage traps by solar wind H, with diffusion acting only as a means of populating traps and not directly influencing the shape of the H distribution, and (4) a relatively unmodified (except by erosion) implantation distribution for a "suprathermal" ($\sim$5 - 100 keV) solar proton component. Clearly, combinations of these proposed mechanisms should also be considered.

The possibility that a terrestrial contaminant, most likely H_2O, has penetrated beyond the region a few hundred angstroms deep, which might be affected by sputtering or other fractional vaporization effects, and into a region made porous or highly reactive to depths of $\sim$0.4 μm by extreme radiation damage in these few samples cannot be ruled out; but it appears unlikely for a number of reasons. First, the identification as H_2O contamination of H concentrations essentially confined to the 0-500 Å deep region even on exterior

surfaces of heavily pitted rocks such as 64455 indicates that prolonged exposure to solar radiation has not made these surfaces porous to H_2O contamination. Second, exposure of artificially damaged fused silica surfaces to H_2O, even in liquid form, provides no evidence for the penetration of H_2O to depths greater than $\sim$0.1 μm. Third, protection against exposure to atmosphere appears to have prevented the chemisorption of H_2O on the 68124 samples. The H distribution on the pitted 68124,3-B surface was essentially identical to that on the interior surface of 68815,27 indicating that only monolayer physisorption appears to have occurred, with this small surface conentration dissipating rapidly under illumination with the ^{19}F beam. Since H_2O contamination has had such a small effect on these samples, it appears improbable that it could have had such a profound effect on the 68815,27 exterior surface as would be implied by interpreting the observed distribution as extensive penetration of terrestrial H_2O.

Taking this evidence at face value, the bulk of the H content at depths greater than $\sim$500 Å is best interpreted as true lunar H rather than terrestrial contamination. The concentration of this H near (within $\sim$0.5 μm) the surfaces of the samples is consistent with a solar wind origin; however, the details of the depth distributions imply extensive modification of the implantation distribution. Processes which may have significant effects include saturation, solid state diffusion, surface erosion, and radiation damage.

Since the flux of solar wind protons, $\sim 6 \times 10^{15}$ cm^{-2} - yr^{-1}

(Geiss et al., 1970; Bame et al., 1970), is sufficient to saturate an exposed surface with H in a very short time (10 - 100 yr), the turnover of the top soil layers should insure that most soil fragments have been exposed long enough to reach saturation at some time in lunar history. However, very few grains (other than ilmenite) are actually found with saturated surface layers (Eberhardt et al., 1970; Kirsten et al., 1971), implying that diffusive losses may be extensive even for concentration levels well below saturation. While many lunar rocks have apparently been tumbled so that all faces have been exposed for times > 10^5 yr, a significant number exhibit no microimpact pits on their lunar bottom surfaces and hence have apparently been exposed in only one orientation (Morrison et al., 1972). Rocks 15015 and 15059 appear to fit this latter category; however, the surface of rock 68815 from which sample 68815,27 was taken has an exposure age of $\sim 2 \times 10^6$ years, and has therefore certainly had adequate exposure to reach a balance between the rate of implantation and the rate at which H is lost from the surface by diffusion and erosion.

The apparent penetration of rare gases to depths of up to a few microns in lunar soil grains has been attributed to solid state diffusion of solar wind ions (Kirsten et al., 1970). Unfortunately, little is known about diffusion of gases in lunar materials, except by inference from the known properties of terrestrial materials. However, if a bulk diffusion process is assumed for the redistribution of implanted solar wind protons, an equilibrium distribution may eventually be reached due to a balance between the rate at which the

diffusion front progresses into the material and the rate at which the surface is being eroded by solar wind sputtering. The characteristic depth of such a distribution would be given by D/v where D is the diffusion coefficient defined by Fick's law and v is the atomic erosion rate. Using an erosion rate of 0.5 Å/yr and the characteristic depth of 0.2 μm for the measured distributions, an estimate of 10^{-13} cm^2/yr is obtained for D. This is to be compared with the following known diffusion coefficients for H in fused silica at temperatures of 100-150°C (lunar daytime temperatures): $\sim 10^{-2}$ cm^2/yr for interstitial diffusion of H_2, $\sim 10^{-4}$ cm^2/yr for diffusion of H^+ to form OH^-, and $\sim 10^{-9}$ cm^2/yr for diffusion of OH^- (Brückner, 1971). Hence it appears that bulk diffusion should be much <u>too fast</u> to account for the observed distributions. However, the mobility of any diffusing species is influenced by local radiation damage, with the result that the diffusing particles can be "trapped" in radiation damage defects at low temperatures and released in the healing process at higher temperatures ($\gtrsim$ 500° C) (Matzke, 1966). A weak form of trapping, with a finite mean trapping time, might result in a diffusion coefficient of the right order of magnitude (10^{-13} cm^2/yr at $\sim$100° C); however, the shape of the H depth distribution would be determined by diffusion-erosion equilibrium only if the distribution of traps were reasonably uniform as a function of depth. The observation of 200-1000 Å thick metamict coatings on lunar dust grains (Borg et al., 1971) indicates that radiation damage is quite severe in this depth range. However, high densities of nuclear particle tracks (> 10^{11} tracks/cm^2) were

also observed in the underlying grain. In a bright-field micrograph of an Apollo 11 grain (Fig. 3 of Borg et al., 1971) the authors point out that "very few tracks with length greater than 0.5 μm can be seen." This suggests that the radiation damage distribution may be quite steep over a 0.5-μm depth range, resulting in a distribution of traps which decreases rapidly with increasing depth over this range. Hence, the distribution of radiation damage traps may be a more important factor than diffusion in determining the depth distribution of H in lunar samples.

A number of studies concerned with the trapping of rare gases in radiation damaged solids have led to a partial understanding of the interactions of the implanted rare gas atoms with radiation damage (Kelly and Brown, 1965; Matzke, 1966; Matzke and Whitton, 1966; Kelly et al., 1968; Ducati et at., 1972). At low implantation doses, gas release is governed by normal diffusion kinetics. However, if the doses are high enough ($\sim 10^{16}$ ions/cm^2) three new processes appear. A small but significant fraction of the gas is released at temperatures between the bombardment temperature and the onset of release by normal volume diffusion. This is interpreted as diffusive motion which is short-circuited towards the surface by interconnected regions of radiation damage, and is given the name "damage diffusion" (stage I). Normal volume diffusion (stage II A) is replaced by diffusion with weak trapping (stage II B) at high doses, characterized by a higher temperature release. Gas atoms are believed to be trapped in defects produced by the heavy radiation damage, possibly small vacancy clusters.

Large activation energies are required for escape from a trap; however, trapped gas atoms are released when the temperature is sufficiently high to allow healing (annealing) of the disordered regions and, hence, elimination of the traps. Thermal release profiles may be different for the various rare gases if escape from traps is important at lower temperatures, but release at annealing temperatures is common to all of the rare gases. A third process, bubble diffusion (stage III), is important at much higher temperatures and involves the motion of gas-filled bubbles.

The rare gas contents of lunar samples are only a small residue of the amounts implanted during surface exposure. Ducati et al. (1972) suggest that most of the solar wind gas atoms are lost from the heavily damaged metamict coatings at lunar daytime temperatures by the "damage diffusion" mechanism discussed above (stage I). The remaining gases may diffuse inward to populate traps associated with the high track densities observed beneath the metamict coatings by Borg et al. (1971), or may be retained in the metamict layer in those traps which are not connected with the surface. Duplication of the lunar sample He release patterns for synthetic glass implanted with relatively low He^+ doses ($< 10^{15}$ ions/cm^2) but pre- or post-damaged with high <u>proton</u> doses (6×10^{16} ions/cm^2) represents convincing evidence for the proposed dependence on gas-damage interactions, since samples implanted only with a low dose of He^+ show a much different release pattern. At low doses normal volume diffusion results in a low-temperature peak in the differential release profile, while at

high doses a second peak appears at a higher temperature (consistent with temperatures necessary for partial annealing) at the expense of the first peak. Observation of this same effect with relatively low He^+ doses in pre- and post-damaged samples argues strongly against interpreting the higher temperature release as simply the effect of having high rare gas concentrations, independent of the radiation damage.

For hydrogen, the situation is complicated by the possibility of chemical effects. Epstein and Taylor (1970, 1971, 1972) have shown that H exists in lunar samples in forms which are thermally released as both H_2O and H_2. The high D/H ratio in the released H_2O (up to 133 ppm) as compared to the H_2 (as low as 18 ppm) has led them to identify the H_2O as primarily terrestrial (typically $\sim$150 ppm D) contamination while most of the H_2 is undoubtedly related to the solar wind (< 10 ppm H). The H_2/H_2O ratio ranges between 2 and 5; however, the variation of D/H ratios with temperature indicates that there is significant exchange of terrestrial and lunar H between the two chemical forms.

Lord (1968) has shown that artificial implantation of 2-keV protons into terrestrial silicate minerals (olivine and enstatite) is followed by thermal release of H_2 gas. A retention coefficient of 0.9 for doses as high as 5×10^{16} ions/cm^2 ($\sim$0.1 saturation dose) was obtained by comparing the quantity of H_2 released to the total proton dose. The implications of this result for the lunar samples, that implanted solar wind H would probably be released as H_2 rather than

H_2O (or some other product of chemical interaction with the medium), are consistent with the interpretation based on the different D/H ratios of the two thermally released chemical forms. However, infrared absorption lines characteristic of OH and OD groups have been observed in silicate targets following bombardment with MeV protons and deuterons, respectively (Zeller et al., 1968), suggesting that formation of hydroxyl groups by interaction of implanted solar wind protons and the lunar silicates may be an important process. The release of implanted H primarily in the form of H_2 from lunar and terrestrial samples indicates that either only a small fraction of the retained H was in the form of hydroxyl, or that the O-H bonds are preferentially broken in the thermal release experiments. Since most of the H_2 is released from lunar samples at about the same temperatures as He (Gibson and Johnson, 1971) and in agreement with temperatures ($\sim$500° C) at which partial healing of radiation damage is expected (Matzke, 1966), one might expect that He and H_2 gas are trapped together in the same sites. Indeed, small gas bubbles ($\sim$80 Å diameter) have been observed in breccia and soil grains and attributed to solar wind (Phakey et al., 1972). Gentle room-temperature crushing of a breccia sample (Funkhouser et al., 1971), however, resulted in appreciable ($\sim 10^{-3}$ of total content) rare gas release but very little H_2 ($2H_2/He \simeq 0.01$ compared to $\sim$8 for thermally released gases) and no detectable H_2O. A similar result was obtained by crushing a sample of fines (Epstein and Taylor, 1972) which released normal amounts of H_2 on heating. This suggests that H does

not exist as molecular H_2 gas populating the same voids, bubbles and grain boundaries as He, but rather in an atomic or ionic state with chemical binding preventing release at room temperatures. Formation of hydroxyl groups is one possibility, but the diffusion of OH in silicates appears to be too fast to retain OH near the surface without significant radiation damage trapping effects. It appears likely that both H and He are trapped in vacancies and vacancy clusters, with the H forming a chemical bond with one of the surrounding atoms, while the trapping for He is purely a physical effect. Hence, room-temperature crushing would release He but not H, while the healing of defects at $\sim 500^\circ$ C would result in the release of both H and He from their substitutional sites, with the H atoms combining to form H_2.

Since radiation damage appears to influence the mobility of implanted ions so strongly it is reasonable to suppose that the observed H depth distributions could reflect the concentration of traps as a function of depth. The thickness of the metamict coatings (~ 500 Å) has been correlated with the radiation damage range of ions of mean solar wind velocities. The formation of these metamict layers is attributed to interconnection of a high density of radiation damage islands, so most traps may be interconnected with each other and with the surface, providing an explanation for the almost total loss of solar wind H from this region. One would expect, then, to find a peak concentration of isolated traps below this damage-saturated layer where the radiation damage due to solar wind particles with higher-than-average velocities is still quite heavy, but not

severe enough to interconnect the isolated traps. Calculations of radiation damage ranges from theoretical considerations (Winterbon et al., 1970, Schiøtt, 1966) agree well with experimentally determined damage ranges (Hines and Arndt, 1960) for ions of solar wind velocities in quartz, and indicate that damage from solar wind He should extend deeper than damage due to either H or heavier solar wind ions of the same velocity. Using optical techniques to measure the thickness of a layer in which saturated radiation damage has altered the refractive index, Hines and Arndt (1960) found a radiation damage range of 0.19 μm for 3.8 keV/amu He^+ ions. Bulk solar wind energies as high as 3.5 keV/amu have been detected in 3 hour averages of satellite data (Wolfe, 1972). Hence the observation of a rapid decrease in H content with increasing depth at ∿0.2 μm deep in several of the samples analyzed in this study is consistent with an interpretation in which the observed depth of the H-rich layer is related to the maximum range over which solar wind is effective in producing radiation damage. A small fraction of the implanted solar wind H may diffuse inward to populate these traps, rather than escape to the surface with the bulk of the solar wind H. The more gradual decreases with increasing depth between 0.2 μm and 0.4 μm deep may represent a slow escape of H from these traps with a subsequent inward diffusion, or it may reflect a more gentle gradient in the concentration of traps. Since this region is beyond the damage range of solar wind ions and since solar flare ions are too penetrating to result in a noticeable damage gradient in this depth region, such

a gradient could only be due to ions of intermediate energies ($\sim$10-100 keV) such as the suprathermal protons observed by Frank (1970).

The possibility of an appreciable flux of suprathermal protons suggests an alternative explanation for the observed H depth distributions, that of direct implantation of suprathermal protons resulting eventually in an equilibrium with surface erosion and involving only minor modifications due to diffusion. Such an equilibrium would be reached in a time given by R_{max}/v where R_{max} is the maximum range of the implanted ions and v is the erosion rate. For $R_{max} \approx 0.5$ μm and $v \approx 0.5$ Å/yr the required time is $\sim 10^4$ yr. In Appendix E, the procedure for calculating the depth distribution resulting from a spectrum of incident energies is outlined. A convolution of the flux spectrum with a function representing the equilibrium depth profile due to a monoenergetic portion of the spectrum must be performed. The form of this function for solar protons as well as for normal incidence and an isotropic angular distribution (neglecting the effects of range straggling) are shown in Figure 25. Since the exposure age of 2×10^6 yr for 68815,27 is well in excess of the time necessary to reach equilibrium, this sample was chosen as representative of an equilibrium distribution. Figure 26 shows an example of the kind of long-term flux spectrum needed to give such a distribution, with suprathermal proton data from Frank (1970) plotted for comparison. It should be noted, however, that these data represent the peak flux during one of several events

(similar to solar flares) observed by Frank and, consequently, should not be considered as representative of a long-term average. Figure 27 shows the H distribution resulting from the hypothetical long-term spectrum compared to the initial set of data from 68815,27, as well as the tail of a distribution chosen to overestimate the penetration of present-day solar wind protons ($\sim 10^8$ cm^{-2}-sec^{-1} between 1 and 2 keV and $\sim 10^7$ cm^{-2}-sec^{-1} between 2 and 3 keV) calculated for normal incidence and including theoretical estimates of the straggling in projected range (Schiøtt, 1966). The implied long-term suprathermal proton fluxes are lower than the fluxes in the events observed by Frank by almost an order of magnitude, indicating that this proposed explanation of the observed H profiles deserves serious consideration. However, the long-term average flux in this range may well be many orders of magnitude lower than the peak fluxes indicated by the data in Figure 26.

Consideration of the various processes which might affect the shape of the measured profiles has led to the following conclusions:

(1) Essentially all of the implanted solar wind H has been lost from the $\sim$500-Å thick amorphous layer in which it is stopped.

(2) While a portion of the observed H contents of the 0-500 Å deep surface layer may be a remnant of implanted solar wind, most of the H observed in this region has been attributed to H_2O contamination, both physisorbed and chemisorbed. It is doubtful that the extensive penetration necessary to explain the deeper features of the H profiles

of some samples is possible, especially for the vacuum-sealed sample 68815,27.

(3) The deeper features may reflect a steep gradient in the concentration of radiation damage traps, with the traps populated by diffusion of solar-wind (and/or suprathermal) protons. The high mobility of the H under bombardment with the ^{19}F beam, especially in the 0-0.2 μm region, suggests that this interpretation, involving high levels of radiation damage to depths up to about 0.2 μm, is more probable than the direct implantation of suprathermal protons unaffected by radiation damage or diffusion. The extent of radiation damage apparently decreases from saturation near ∿500 Å to a fairly low level at ∿0.2 μm deep. The damage to these depths is probably due primarily to He ions from high velocity solar wind streams which can cause radiation damage to significantly greater depths than protons of the same velocity and are much more abundant than the heavier ions (which have comparable ranges). The thermal release of H_2, apparently of solar wind origin, at ∿500° C is consistent with the annealing of these traps. The mobility of the H in the 0-0.2 μm deep region under illumination with the ^{19}F beam may not be a temperature effect but may actually be due to collisions between fast ^{19}F ions (10^{14} ions/cm^2 for each data point) and trapped H atoms, knocking the H out of traps; or, perhaps, may be due to the interaction of secondary electrons produced by the ^{19}F ions with the chemical bonds, resulting in the release of some of the previously bound H. Once released from isolated traps, the H may be able to escape to the surface through inter-

connected regions of radiation damage. This hypothesis would explain why the distribution is stable under a bakeout to 300°C, but highly mobile under irradiation even though the surface temperature of the irradiated spot is probably somewhat lower than 300°C.

(4) The portion of the H distribution extending from ~0.2 μm deep to depths greater than 0.4 μm, characterized by a more gradual decrease with increasing depths, is best interpreted as either an inward diffusion of H that has escaped from traps in the highly damaged 0 - 0.2 μm deep region into a region with relatively uniform, low-level damage from solar flare ions; a population of traps by diffused solar wind and/or suprathermal H reflecting a gradient in the trap concentration caused by damage from suprathermal ions; or a direct implantation of suprathermal protons. The first interpretation does not depend on any long-term suprathermal ion flux, but does require a rather low diffusion coefficient. This possibility is not inconceivable, however, since the diffusion of OH may be strongly dependent on the chemistry of the medium, or weak trapping in solar-flare damage tracks may slow the diffusion process significantly. However, suprathermal ions have been detected and track gradients over the 0 - 0.5 μm depth range have been observed in lunar soil grains, so such a diffusion process would probably be strongly affected by the resulting gradient in the concentration of traps. Higher long-term fluxes ($\sim 10^{13}$ protons/cm^2 - yr) are needed in order to explain the observed distribution in terms of direct implantation of suprathermal protons (with only minor diffusion

effects) as compared with the fluxes necessary to create a sufficient density of traps; however, even these fluxes are almost an order of magnitude lower than the events detected by Frank (1970). Thus, further investigations are necessary in order to distinguish between the possibilities implied by these results.

Although the shape of the H profiles between a few hundred angstroms and $\sim$0.4 μm deep, with the alternative interpretations discussed above, is quite consistent; the absoulte H content in this region shows a rather large sample-to-sample variation (Table 3). The profile shapes are all consistent with the existence of a small uniform volume concentration (averaging about 40 ppm H by weight), underlying varying amounts of surface contamination and a "deep" (0.05 - 0.4 μm) component, with a relatively well defined shape, which has been attributed to implanted solar protons. Variations in the absolute amount of this component must either be due to differences in exposure time or differences in the implanted material. Although we cannot rule out a short (possibly zero) exposure age as an explanation for low H content in unpitted surfaces, the cratering rate for rocks (10 - 100 pits with spall diameters > 1 mm per cm^2 per million years) implies that any surface with an appreciable number of visible pits ought to have reached an equilibrium between the incident proton flux and the rate of loss of H by diffusion and erosion. Thus, differences in the retention properties of the lunar materials must account for the bulk of the observed variation. Ilmenites have been found to retain solar wind rare

gases much better than the silicate minerals. Glasses are more open structures than crystallized minerals, and should, therefore, be subject to larger diffusive losses. However, Ti-rich glass fragments were found to retain rare gases better than silicate minerals, although not nearly as well as ilmenite (Kirsten et al., 1972). Most of the glass samples analyzed in the present study are dark in color and could probably be classified as Ti-rich. However, the degree of devitrification may well be important in determining the trapping efficiency of a particular sample. Hence even the extremely fine crystalline grains in a devitrified glass such as the 68815,27 matrix material may provide large numbers of radiation damage traps that the open structure of the actual glass would not. If this interpretation is correct, the low "deep" (0.1 - 0.4 μm) H contents of exposed splash glasses, such as the coating on 15059,32, may be due to rapid quenching resulting in an extremely low degree of crystallization. Such a uniformly open structure may be incompatible with the formation of traps by radiation damage.

The observed widths of the H distributions (about 0.2 μm) in samples such as 68815,27, the 10085 brown glass fragments, and 15413,5-2 are in good agreement with the chemical etching results of Eberhardt et al. (1970) on ilmenite grains. These authors showed that a 50 percent reduction in the content of each of the rare gas isotopes ^{4}He, ^{20}Ne, ^{36}Ar, ^{86}Kr and ^{132}Xe could be obtained by removing a surface layer 0.15 - 0.20 μm thick by etching with HF. The observation that the depth of the distribution is essentially

independent of the mass of the implanted atom is a strong argument against any proposed redistribution mechanism which depends on normal volume diffusion, since diffusion coefficients for rare gases are quite sensitive to the atomic weight. A population of radiation damage traps by all of the rare gases seems favorable.

An alternative origin for some of the "deep" (> 0.1 μm) hydrogen is that it is indigenous to the lunar sample rather than being incorporated as a result of the lunar surface exposure of the sample. This interpretation is particularly suggestive for the 64455 samples in which the "deep" H concentrations, although small, are similar for the interior and exterior samples. On the other hand, for 68815,27 the large difference in H content at ∿0.4 μm deep between the interior and exterior samples strongly argues for a solar particle origin for most of the H at this depth in the exterior sample. The deep H in the Apollo 11 and 15 coarse fine samples appears to be more like that of 68815, although here we do not have interior and exterior samples for comparison. The possibility of H in interior samples unrelated to the recent surface exposure of the rock can be tested by bulk H analysis of interior samples.

Rock 64455 is regarded as a crystalline rock (Grieve and Plant, 1973; Wilshire et al., 1973) although it is quite possible it has been formed by metamorphism of a breccia. Consequently if, prior to metamorphism, the rock contained a component of surface irradiated material, then it is possible that a fraction of the H from this material has survived the heating and thus has been "inherited" by

64455 in its present form. High voltage electron microscope studies (Macdougall et al., 1973; Hutcheon et al., 1972) have shown that essentially all Apollo 14 breccias show evidence for such a pre-irradiated component.

An intriguing alternative hypothesis is suggested by the observations of rusty regions ("goethite") around metal grains on a thin section of an interior sample of 64455 by Grieve and Plant (1973). Similar observations have been made on other Apollo 16 rocks, notably 66095 (Taylor, 1973; El Gorsey et al., 1973). Grieve and Plant argue that, because the rust was seen in the interior portion of the rock, it is lunar in origin; however, it would appear difficult to rule out the possibility that the rust formed during the thin-section making process. Nevertheless, our observation of the roughly uniform deep H concentrations in both interior and exterior samples of 64455 are consistent with the conclusions of Grieve and Plant and the hypothesis of indigenous lunar "goethite," but do not establish a lunar origin. The techniques employed in the present study are potentially useful to the investigation of this problem, particularly if an attempt is made to extend the measurements to greater depths on interior samples, because H can be detected in the interior portions of samples which are shielded from atmospheric exposure with a sensitivity of $\sim$20 ppm.

2. Depth distributions of F in lunar samples

The results of F depth distribution measurements on Apollo 16 samples provide evidence for an enhanced F content within one micron of the surface, compared to bulk values as measured by Jovanovic and Reed (1973) on other Apollo 16 rocks (<50 ppm F) and soils (50 - 100 ppm F). The ^{19}F content of one surface of the anorthosite fragment 66044,8 was nearly 2000 ppm in the outer 0.5 μm and ∿1400 ppm in the underlying 0.5 μm region. The F content of the opposite face was less than half these values indicating that F distributions are characterized by large local variations. F contents of 400 - 1000 ppm in the 0 - 0.5 μm deep layer were found in three samples: glass chip 65315,6 glass spherule 68124,3, and rock chip 68815,27. Some of these samples had received doses of ^{19}F ions previously for the H analysis, but the amounts of F observed are much larger than the previous ion dose. In addition, the range of the 17-MeV ^{19}F ions is about 8 μm (Northcliffe and Schilling, 1970) and it is extremely doubtful that any appreciable amount of the implanted ^{19}F could migrate to within one micron of the surface.

The details of the distributions were highly variable from sample to sample, with 68815,27 (Fig. 20) showing one of the most striking profiles. In light of the surface potentials measured on other samples using the $^{27}Al(p,\gamma)^{28}Si$ reaction, it appears quite possible that charging of the sample by the proton beam could cause a high enough surface potential to account for the observed peak as a surface (zero-depth) F concentration. The 8-kV surface potential

necessary to account for the apparent depth of the peak, assuming it is actually at zero depth, is not unreasonable. However, the excellent reproducibility of this distribution (data from two consecutive energy scans are plotted together in Figure 20), requiring an extremely stable surface potential,makes this interpretation appear somewhat unlikely. In spite of this reservation, charging seems to be a slightly more probable explanation than any of the alternatives.

For the 68124 samples, the apparent depth of the peak F content agrees reasonably well with the expected position of a surface concentration due to the measured surface potentials of 8 and 10 kV on the two 68124,3 surfaces and 14 kV on 68124,10-B. For 66044,8-B, only a small (~2 kV) surface potential was detected, but a narrow peak was observed apparently much closer to the surface than the similar feature in 68815,27. Although the measured potentials do not correspond as well to the apparent depths of the peak concentrations for the 65315 samples, the discrepancies are not so great that surface (zero-depth) concentrations can be ruled out.

The unresolved question of contamination makes it premature to identify the observed F contents in these samples as true lunar F with absolute certainty although the large F contents observed in several samples <u>beneath</u> a fairly narrow peak near the surface are probably real. It is interesting to note that three of the four samples richest in F were from the sealed rock box (ALSRC) and that the interior surface of one of these, 68815,27, showed relatively large amounts of F, apparently due to contamination. Nevertheless,

the F contents of interior rock surfaces are all less than 200 ppm, so a lunar origin for much of the observed F in the exterior surfaces does not appear unreasonable. Although the concentrations in the outer 0.5 μm of all the samples analyzed in this study are somewhat lower than the Surveyor 7 fluorine levels, the value of 1900 ppm (0.19%) for 66044,8-B is within the uncertainties of the Surveyor measurements. Hence the results of this study are not incompatible with the interpretation of the high F contents measured in the Surveyor 7 soils as a real surface-correlated lunar fluorine concentration. The contamination question will have to be answered more definitely before firmer conclusions can be drawn.

IV. OBSIDIAN HYDRATION PROFILES

Exposure of fresh surfaces of natural obsidian to ambient water, either as ground moisture or atmospheric humidity, results in a slow diffusion process with the eventual formation of a hydration rind (Friedman and Smith, 1960). Microscopic examination of a thin-section cut perpendicular to such a surface reveals a well-defined band up to ~20 μm in thickness. The thickness of this hydration rind can be measured under the microscope with a resolution of ~0.2 μm and correlated with the age of a given surface if the hydration rate is known. The hydration rate is believed to be essentially independent of the relative humidity (above some minimum value of a fraction of one percent). The temperature and the chemical composition are observed to be much more important rate controlling variables. Using radiocarbon dating techniques as a calibration, a hydration rate is estimated for a given area, where a single effective temperature and obsidian chemistry can be assumed. The result is a relatively simple technique for archaeological dating of obsidian artifacts, since fresh surfaces are exposed in the chipping process used by the artisan to fashion the desired implement.

The $^{1}H(^{19}F,\alpha\gamma)^{16}O$ technique for depth analysis of hydrogen represents a unique probe for the direct measurement of obsidian hydration profiles. Results of such measurements on a variety of obsidian samples are presented and discussed in this section.

A. Experimental Results

A number of obsidian samples with estimated (from known exposure age) or optically measured hydration bands of < 2 μm were collected, along with several much older samples with thicker hydration layers. Samples were prepared by selecting a clean surface and cutting or chipping a ~1-cm^2 sample of exterior surface. The samples were then degreased with trichloroethylene and rinsed in methanol prior to mounting in the scattering chamber.

Hydration profile measurements were performed by first collecting raw data in the form of γ-ray counts per 3 μC of $^{19}F^{4+}$ vs. E_o, the ^{19}F bombarding energy, as described in Section II. The counting rate $Y(E_o)$ was related to water concentration with the assumption that all of the detected H could be identified as "water."

The results of obsidian hydration profiles measured in this manner are given in Table 5. Samples 1 - 4 had sufficiently narrow hydration layers that the entire hydration profile could be measured without encountering the resonance at E_{R2} = 17.64 MeV, as shown in Figure 28 for samples 2 and 4. The hydration layer thicknesses listed in Table 5 for these samples were obtained by subtracting (in quadrature) the resonance width Γ_1 from the measured energy-width of the excitation function and converting the result to a depth using the calculated stopping power, $dE/d(\rho x)$ (Appendix D), and the density ρ = 2.4 g/cm^2. The H_2O content (in weight percent) of the thin hydrated layer is calculated from the peak counting rate with a correction for the finite width Γ_1 of the resonance, i.e.

$$Y_{max} \propto W \tan^{-1}\left(\frac{h[-dE/dx]}{\Gamma_1}\right),$$

where W is the H_2O content, Y_{max} is the peak yield, and h is the hydration layer thickness. (This expression follows directly from the equations of Appendix A for the case of a distribution confined to a thin layer.) These distributions were not nearly as labile under irradiation with the ^{19}F beam as the H distributions in lunar samples. Excellent reproducibility was found for repeated measurements.

Samples 1-3 were hydrated artificially by heating freshly exposed surfaces of a single obsidian sample for periods of 1,2 and 4 days, respectively, at 75°C in a humid atmosphere (Friedman, 1973). A progressive increase in the thickness of the hydration layer with time is observed, in qualitative agreement with the expected trend of the hydration layer thickness proportional to the square root of the hydration time (Friedman and Smith, 1960). Sample 4 is a surface with an exposure age of ∿10 years at normal temperatures.

Figure 29 illustrates the unfolding procedure described in Section II for a sample with a hydration layer ∿1.2 μm thick (sample 5). Data from an unhydrated obsidian sample (H_2O content uniformly 0.3%) were subtracted point by point from the raw data for the hydrated sample to minimize the effects of beam-dependent background above ∿20 MeV ^{19}F energy. The profile was then unfolded as described in Section II to leave only the contribution of the resonance at E_{R1} = 16.45 MeV. These reduced data were then fitted with

the calculated depth and water content scales, adding back the 0.3% H_2O which was subtracted in a previous step. The result is the hydration profile shown in Figure 29b. The same procedure was used to obtain hydration profiles for samples 6 - 10, with two of these profiles shown in Figure 30. Samples 5 - 10 have all hydrated naturally and their hydration bands have all been measured by the optical thin-section technique described previously. In general, the hydration-band thicknesses measured in this way show good agreement with the depth at which the H_2O concentration gradient is a maximum. Samples 6 - 9 are artifacts collected from the same archaeological stratum and thus are probably of the same approximate age and have had the same temperature history. Consequently, differences in the hydration profiles may be controlled primarily by sample to sample differences in chemical composition.

In addition to the samples listed in Table 5, several samples with much greater exposure ages were also obtained. These samples have hydration rinds much thicker than the 2-μm limit of the present measurement technique, but the H_2O content of the outer 2-μm layer should be representative of the final saturation H_2O content for a given sample. Table 6 lists the measured H_2O content in these samples and in freshly exposed surfaces from the same obsidian sample.

Using the resonance at a proton energy of 1.318 MeV in the reaction $^{23}Na(p,\gamma)^{24}Mg$, we have also measured the sodium depth distributions to a depth of ∿1 μm in two samples with hydration layers less than 0.2 μm thick (samples 1 and 4 of Table 5) and in ancient and

fresh surfaces from the same obsidian source. This was done to check a hypothesized ionic-exchange diffusion mechanism predicting a sodium depletion in the hydrated layer (Bikerman, 1970). No significant variation of Na content (typically ~3% Na_2O) was detected; however, the resolution was limited by counting statistics to a detection threshold of about a ten percent variation in the Na content.

B. Discussion

The detailed hydration profiles measured by this technique can be used to obtain information about the mechanism of water diffusion into obsidian and the factors which influence hydration. The general shape of the measured profiles agrees qualitatively with the idealized profile suggested by Friedman et al. (1966), characterized by a saturated hydration plateau followed by a steep diffusion front, rather than the more conventional exponential profile suggested by Marshall (1961). However, the presence of a second step in some of the hydration profiles (Fig. 30) suggests that more than one mechanism of water diffusion and binding may be important in the hydration process. The good general agreement between the optically measured hydration band thickness and the depth at which the H_2O concentration gradient is a maximum verifies the interpretation of Friedman et al. (1966); with the border between the hydrated and unhydrated regions made visible in ordinary light due to a difference in index of refraction between the hydrated and unhydrated region. The bright appearance of this border under crossed polarized light

is due to stress birefringence at the point of maximum stress (due to the change in volume associated with hydration), and it is not surprising that this point should be correlated with the H_2O concentration gradient. It should be noted, in this regard, that H depth distributions have also been measured for a number of tektite samples (which do not have visible hydration bands); and these distributions were characterized by a gently-sloping exponential diffusion profile, rather than the steep diffusion fronts observed in hydrated obsidians.

Evidence for the effects of chemical composition can be found by inspection of the data in Table 6 and for samples 6 - 9 in Table 5. A comparison of the H_2O content of hydrated and unhydrated samples from the same source shows a consistent correlation of the final saturation level with the intrinsic H_2O content. It is also apparent from the data for a set of obsidian samples from the same source, and presumably with the same exposure history, that the saturation H_2O content and the thickness of the hydration layer are weakly correlated (Table 5, samples 6 - 9). This suggests that the chemical factors which control the saturation level also control the rate of growth of the hydration rind.

Finally, a progressive increase in the thickness of the artificially hydrated layer with the exposure time at 75°C is observed (Table 5, samples 1 - 3). The ability of this technique to resolve and accurately measure such thin hydration layers as can be prepared under controlled laboratory conditions on a reasonable time scale makes this type of experiment particularly promising. The investigation

of the effects of chemical composition and temperature on the hydration rate can be carried out under controlled conditions. The contribution of such an investigation toward understanding the hydration process could have great potential value in terms of the establishment of a precise hydration rate for a particular set of conditions. This rate could then be used to obtain a more accurate date for obsidian artifacts than is currently possible.

V. CONCLUSION

A. Lunar Sample and Obsidian Analyses

Despite the implicit ambiguity in the interpretation of the origin of the H observed in lunar samples, the $^{1}H(^{19}F,\alpha\gamma)^{16}O$ depth analysis technique has been shown to provide a reasonably accurate and reproducible measurement of its distribution, limited only by the mobility of the hydrogen under irradiation with the ^{19}F beam. Simply decreasing the beam current density will help to control this problem, as has been demonstrated for one of the larger glass-coated rock chips (15015,39-2). For smaller samples, significant decrease in beam current density could only be achieved at a sacrifice in counting rate, leading to large statistical uncertainties, unless the NaI(Tℓ) detector can be placed closer to the irradiated sample. This is not possible with the present scattering chamber, but has been successfully done with a new UHV scattering chamber of an improved design. Nevertheless, the results of this study have provided an insight into the interaction of solar corpuscular radiation with lunar materials which could not be obtained by more conventional techniques.

The potential usefulness of the $^{1}H(^{19}F,\alpha\gamma)^{16}O$ depth analysis technique for the study of solid state diffusion processes involving H has been demonstrated by the obsidian hydration profile measurements performed in this study. The reproducible profiles obtained on a variety of obsidian samples have verified the correspondence

between the location of the stress birefringence line visible under the microscope, and the depth at which the H concentration gradient is a maximum, for hydration rinds up to 2 μm thick. This technique appears to be particularly well suited to the measurement of very thin (< 0.5 μm) hydration layers where the order-of-magnitude improvement in resolution over optical techniques can be used to best advantage. An investigation of the dependence of the hydration rate on chemical composition using obsidian samples hydrated under controlled conditions appears to be a particularly promising application of this technique. The results of such a study would be valuable in establishing the reliability of the age assigned to an obsidian artifact on the basis of the thickness of its hydration rind.

The measurement of fluorine depth distributions using the $^{19}F(p,\alpha\gamma)^{16}O$ reaction has already been demonstrated (Möller and Starfelt, 1967). The application of this technique to lunar samples has been somewhat inconclusive due to the suggestion of significant contamination and also due to the problems caused by charging of the silicate samples with the ion beam. The zero-point of the depth scale could be redefined based on the $^{27}Al(p,\gamma)^{28}Si$ measurements, if these measurements were performed with sufficient care to improve the uncertainties in the surface-potential determinations. Even then, however, the large potential fluctuations apparent on several samples would cause a significant degradation in the depth resolution. The charging problem could be solved quite easily by depositing a

thin conducting film onto the sample surfaces to be analyzed; however, it is not clear that elimination of the uncertainties caused by sample charging would justify this destructive procedure. Nevertheless, if further investigations are able to demonstrate that contamination can account for only a small portion of the large F contents observed in a 1-μm thick surface layer on several of the lunar samples, the results of this study will have an unambiguous interpretation as true lunar F, providing possible evidence for recent exhalations of volcanic gases from the moon.

B. Additional Applications of Nuclear Techniques for Depth-Sensitive Analysis

The $^{19}F(p,\alpha\gamma)^{16}O$ technique is also being used to determine the F content of chondritic meteorite samples. The carbonaceous chondrites are of special interest because their compositions are presumed to reflect cosmic elemental abundances. Samples with fresh surfaces were obtained by chipping from three carbonaceous chondrites (Allendé, Erakot and Murchison). Preliminary results on three samples of Allendé matrix material and two samples from Murchison indicate that a range of ∿40 ppm to ∿70 ppm F may be applicable to both of these meteorites. The F determination for one Erakot sample also fell in this range. These measurements are significantly lower than most previous F determinations in carbonaceous chondrites, except for the 66 ppm determined by Reed (1964) in the carbonaceous chondrite Lancé. A more extensive data set

must be obtained from a particular meteorite in order to establish a value representative of the meteorite as a whole; however, the sensitivity of this technique appears to be at least competitive with the n-activation, γ-activation and emission spectrography techniques used previously (Reed, 1971).

Another application of resonant nuclear reaction techniques takes advantage of their particular sensitivity to surface contamination, using a variety of reactions to identify contaminants on surfaces for which cleanliness is critical. A particular example is a series of measurements performed on electroplated lead samples in an effort to identify the source of residual RF losses in superconducting lead cavities being developed for a heavy ion accelerator. In a previous study (Tombrello and Leich, 1971), the alpha particle yield from the 0.2-MeV wide resonance in the reaction $^{16}O(^{3}He,\alpha)^{15}O$ at 2.36 MeV(^{3}He energy) was measured to determine the surface concentration of ^{16}O to be $\sim 3 \times 10^{16}$ cm^{-2}. Subsequent measurements have used the resonance in the reaction $^{12}C(d,p\gamma)^{13}C$ at a deuteron energy of 1.446 MeV (Ajzenberg-Selove, 1970) to determine carbon concentrations and have also included F and H determinations using the $^{19}F(p,\alpha\gamma)^{16}O$ reaction. The results for untreated lead samples show 5×10^{16} C/cm^2, 2×10^{16} H/cm^2 and 5×10^{15} F/cm^2. In each case the thickness of the contaminated layer was shown to be < 300 Å. Samples treated in a chelating agent (trade name Versene) show decreases in the C and H concentrations by factors of 2 and 5 respectively, but F is increased by a factor of 2. A vacuum bakeout

at 250°C, however, decreased the C, H, and F concentrations by factors of 5, 10, and 100, respectively, suggesting that if dielectric losses are a limiting factor in the performance of the superconducting resonators, a vacuum-baked resonator should show a marked inprovement in Q value compared to cavities that have not been baked. However, the thickness of dielectric implied by these measurements is much too small, even for the untreated samples, to account for the observed losses (Dick, 1973).

Additional possibilities for the application of these techniques are numerous. As an extention of our investigation of depth distributions of implanted solar ions in lunar materials, the reaction $^{4}He(^{10}B,n)^{13}N$ looks particularly promising as a depth analysis probe for He with a depth resolution of $\sim$300 Å. The H/He ratio of $\sim$8 for lunar soils implies that neutron counting rates from the resonance at 3.78 MeV(^{10}B energy) (Ajzenberg-Selove, 1970) will probably be an order of magnitude lower than the γ-ray counting rates from $^{1}H(^{19}F,\alpha\gamma)^{16}O$ on lunar samples. This may represent a serious limitation if the He distributions are mobilized by the ion beam to the same extent as H. The best possibility for studying implanted solar wind ^{12}C involves the $^{12}C(^{3}He,n)^{14}O$ reaction and the detection of the delayed γ rays following the β^{+} decay of the residual ^{14}O nucleus. (The $^{12}C(d,p\gamma)^{13}C$ reaction discussed earlier is not useful due to copious background from silicate targets.)

The $^{1}H(^{15}N,\alpha\gamma)^{12}C$ reaction represents an alternative way to measure H distributions. The estimated depth resolution using

the resonance at 6.39 MeV (^{15}N energy) (Ajzenberg-Selove, 1971) is better than 100 Å near the surface, and the maximum depth which can be studied without interference from other resonances in the $^{1}H(^{15}N,\alpha\gamma)^{12}C$ reaction is about 3 μm. Hence, significant improvements in resolution and depth range could be obtained at an order-of-magnitude sacrifice in counting rate compared to the present technique using $^{1}H(^{19}F,\alpha\gamma)^{16}O$.

The importance of resonant nuclear reaction depth analysis techniques for the investigation of solid-state diffusion problems has been demonstrated by our study of hydration profiles in obsidian. Clearly, a more general class of solid-state diffusion, weathering and corrosion problems involving chemical surface reactions can be studied using similar techniques.

APPENDIX

A. Depth-Sensitive Analysis with Charged Particle Induced Nuclear Reactions

Consider the general case of a nuclear reaction A(a,b)B involving compound nucleus formation with an entrance channel consisting of a charged particle projectile a and a target nucleus A, and an exit channel characterized by an emitted particle or quantum b and a residual nucleus B. Let the reaction cross section be given by $\sigma(E)$ where E is the kinetic energy of the projectile a. Suppose that nuclei A are distributed near the surface of a solid medium with number density A(x) for a given depth x in the sample. If the sample surface is irradiated with a beam of particles a of energy E_o, the gradual slowing down of the a ions due to electronic collisions, characterized by an energy dependent stopping power [dE/dx] (a negative quantity) results in an ion energy at depth x' given by

$$E(x') = E_o + \int_o^{x'} [dE/dx]dx \ . \qquad (A.1)$$

(Normal incidence is assumed and energy straggling is neglected for the moment.) Without loss of generality we may write the reaction yield per incident particle a of energy E_o as

$$Y(E_o) = \int_o^\infty \sigma(E(x'))\ A(x')dx' \ . \qquad (A.2)$$

Hence, the excitation function $Y(E_o)$ is, in a sense, a convolution of the reaction cross section with the distribution function $A(x)$.

Although it is possible, in principle, to unfold (or deconvolute) the function $A(x)$ from a measurement of the excitation function $Y(E_o)$ for a more general form of $\sigma(E)$, the process is greatly simplified if the cross section is dominated by a single resonance at energy E_R. Then, following the treatment of Fowler, Lauritsen, and Lauritsen (1948), the cross section is given by the Breit-Wigner dispersion equation,

$$\sigma(E) = \sigma_R \frac{\Gamma^2/4}{(E - E_R)^2 + \Gamma^2/4} \qquad (A.3)$$

where $\sigma_R \equiv \sigma(E_R)$ is the cross section at the resonance energy and $\Gamma(<<E_R)$ is the full-width of the resonance at half-maximum intensity (FWHM). (The quantity σ_R includes wavelength and barrier penetration factors which need not be considered explicitly.) Since this form of the cross section consists of a sharp spike at E_R, the effect of equation (A.2) for $E_o > E_R$ is to pick out the value of $A(x_R)$ where

$$x_R = \int_{E_o}^{E_R} \frac{dE}{[dE/dx]} \ , \text{ viz.}$$

$$Y(E_o) \simeq \frac{\sigma_R \Gamma^2}{4} A(x_R) \int_o^\infty \frac{dx'}{(E(x') - E_R)^2 + \Gamma^2/4} , \qquad (A.4)$$

provided that A(x) varies slowly over distances of order $\Gamma/[-dE/dx]$ near x_R, i.e.,

$$\left|\frac{1}{A} \frac{dA}{dx} \frac{\Gamma}{[dE/dx]}\right| << 1. \qquad (A.5)$$

Substitution of equation (A.1) in equation (A.4) and a change of variables leads to

$$Y(E_o) \simeq \frac{\pi \sigma_R \Gamma A(x_R)}{4[-dE/dx]_R} \left[1 + \frac{2}{\pi} \tan^{-1} \left(\frac{E_o - E_R}{\Gamma/2}\right)\right] . \qquad (A.6)$$

The subscript R on the stopping power factor means that it is to be evaluated at E_R. For beam energies sufficiently greater than E_R, i.e., $E_o - E_R >> \Gamma/2$, equation (A.6) reduces to

$$Y(E_o) \simeq \frac{\pi \sigma_R \Gamma}{2[-dE/dx]_R} A(x_R) . \qquad (A.7)$$

Hence the function $A(x_R)$ is obtained directly from the excitation function $Y(E_o)$ using equation (A.7) and the relation

$$x_R = \int_{E_o}^{E_R} \frac{dE}{[dE/dx]} .$$

In practice, the stopping power may vary only slightly over the range from the resonance energy up to the maximum beam energy E_o, so that a useful approximation is

$$x_R \simeq \frac{E_o - E_R}{[-dE/dx]_R} \tag{A.8}$$

The inequality A.5 is an expression of the finite depth resolution (due to the resonance width Γ) associated with the determination of the distribution A(x) from a measurement of the excitation function $Y(E_o)$. Setting A(x) = constant $\times$ $\delta(x-x')$ we obtain an estimate of the resolution $\delta x \simeq \frac{\Gamma}{2[-dE/dx]}$ from the half-width at half-maximum of the distribution inferred from measurement of the excitation function as described above. The effects of energy straggling and the finite energy width of the ion beam (both of which have been neglected to this point) on the resolution can be expressed by:

$$\delta x = \frac{\sqrt{\Gamma^2 + (\delta E_o)^2 + \Omega^2(x_R)}}{2[-dE/dx]} \quad , \tag{A.9}$$

where δE_o is the FWHM spread in the beam energy and $\Omega(x_R)$ is the FWHM energy straggling at depth x_R.

B. Special Procedures for Clean UHV Systems

Special techniques necessary to maintain the cleanliness required in UHV systems include procedures applying to the assembly

and operation of such a system. Selection of materials is one of the first considerations, since low vapor pressure materials must be used exclusively. For this reason, the UHV scattering chamber described in Section II of this thesis is constructed primarily of type 304 stainless steel with metal-to-metal seals using OFHC copper gaskets. The target wheel, however, was machined from a common aluminum alloy, and the electrical connections make use of glass insulators, a sliding beryllium-copper alloy contact, a copper wire with ceramic insulation, and a ceramic-sealed kovar electrical feedthrough. All permanent joints are heliarc welded. All parts must be chemically cleaned before assembly using procedures described in various sources on vacuum technology (see, for example, Espe, 1966). These procedures include a degreasing step using an organic solvent such as trichloroethylene to dissolve oils and grease, one or more acid baths to remove surface layers which may be rich in adsorbed gases, a thorough deionized water rinse to remove all traces of acid, and an ultrasonic rinse in methanol or acetone. This sequence can be followed by drying with a hot air blower, after which parts are placed in clean polyethylene bags until all parts are prepared for assembly. Clean polyethylene gloves should be worn for the assembly as any fingerprints can act as essentially infinite gas sources at ultrahigh vacuum. After assembly, the entire system is baked at $\sim 300^{\circ}C$ to drive adsorbed gases from the vacuum system walls. This procedure is important to minimize this major source of gas.

The most important operational procedures are concerned with opening the system to atmospheric pressure and the subsequent pumpdown. The specific procedures are tailored to the particular system, but a common objective is to minimize both the pumpdown time and the base pressure. This is most effectively done by backfilling the system with dry nitrogen gas and minimizing exposure to room atmosphere. For the present system the procedure is as follows: A liquid nitrogen trapped gas line is connected to the roughing line, evacuated, and then filled with dry nitrogen to a pressure slightly above one atmosphere. The metal sealed roughing valve is then opened allowing dry N_2 gas to fill the system. The viewing window is then removed from the scattering chamber and the mouth of a polyethylene glove bag is clamped to the resulting access port. The glove bag, containing all of the necessary targets and tools, is allowed to inflate and flush with dry N_2 before new targets are exchanged with the old ones. When this operation is completed, the glove bag is removed, the viewing port is immediately replaced and sealed, and the N_2 gas line is disconnected. The system is then pumped down to a pressure of $\sim 10^{-2}$ Torr using the molecular sieve sorption pump refrigerated with liquid nitrogen. The ion pump is started at this pressure. The titanium sublimation pump is typically started at $\sim 10^{-5}$ Torr with a duty cycle decreasing from 1 at pressures above 10^{-6} Torr to less than 0.01 below 10^{-8} Torr. Normally three or four days are needed to attain a vacuum of $\sim 10^{-9}$ Torr.

Periodic bakeouts are helpful not only to maintain a clean

vacuum system but also to remove surface contamination from target samples. Baking to 300°C has been found to eliminate surface contaminants far more effectively than any other procedure.

C. Analyzed Standards and Detection Efficiency

The following samples with their analyses by weight percent were used as standards to establish the conversion from counting rate to absolute concentration:

1) Belvidere Mountain chlorite (Albee, 1971): MgO (33.88), SiO_2 (32.18), Al_2O_3 (16.07), H_2O (14.64), FeO (1.38), plus minor constituents (< 1% each) including Fe_2O_3, CaO and CO_2.

2) Durango apatite (Young et al., 1969): CaO (54.02), P_2O_5 (40.78), F (3.53), RE_2O_3 (1.43), plus minor constituents (< 1%) including Cl, SO_3, SiO_2, and Na_2O.

3) CaF_2: 300 $\mu g/cm^2$ CaF_2 deposited by vacuum evaporation on a tantalum substrate.

The peak counting rate from a 300 $\mu g/cm^2$ CaF_2 target due to the 872 keV resonance in $^{19}F(p,\alpha\gamma)^{16}O$ is calculated to be $\sim$5% less than the counting rate from an infinitely thick target. Correcting for this thickness effect, the measured counting rate can be compared directly with the total thick target yield from CaF_2 determined by Chao et al. (1950) to be 3.7×10^{-7} per incident proton. The result implies a detection efficiency $\eta = 0.0230$. Using the relative stopping powers of CaF_2 and apatite, calculated as in Appendix D, the counting rate measured from the apatite

standard results in a value for η of 0.0215. Using the chlorite standard, a similar value for η is obtained. We take the mean of these results to be the best estimate of the detection efficiency, i.e. $\eta = 0.022$.

D. Calculation of Stopping Powers of Complex Substances

The stopping power of a compound Y_nZ_m for a given energetic ion can be calculated from the atomic stopping powers of the elements Y and Z using Bragg's rule of additivity of atomic stopping cross sections:

$$\varepsilon(Y_nZ_m) = n\varepsilon(Y) + m\varepsilon(Z), \qquad (D.1)$$

where $\varepsilon = \frac{1}{N}\left|\frac{dE}{dx}\right|$ and N is the number of atoms or molecules per unit volume. Since the stopping power data of Northcliffe (1963) and Northcliffe and Schilling (1970) are in the form $dE/d(\rho x)$, it is convenient for purposes of calculation to rewrite equation D.1 as

$$\left[\frac{dE}{d(\rho x)}\right]_{Y_nZ_m} = \frac{n\,A_Y\left[\frac{dE}{d(\rho x)}\right]_Y + mA_Z\left[\frac{dE}{d(\rho x)}\right]_Z}{n\,A_Y + m\,A_Z}, \qquad (D.2)$$

where A_Y and A_Z are the atomic weights of Y and Z respectively. Generalizing this expression to a sample with a complex composition, we obtain

$$\left[\frac{dE}{d(\rho x)}\right]_{sample} = \sum_i f_i \left[\frac{dE}{d(\rho x)}\right]_i , \qquad (D.3)$$

where f_i is the weight fraction of the ith element, $[dE/d(\rho x)]_i$ is the stopping power for a pure substance of element i, and the stopping power for the particular sample composition is obtained by summing the product of these two quantities over all chemical constituents of the sample.

A good estimate to $dE/d(\rho x)$ for a sample of complex composition can be made simply by calculating the average atomic weight and atomic number for the sample composition and finding $dE/d(\rho x)$ by interpolation using these average values (Schiøtt, 1970). For typical silicates, stopping powers obtained in this way differ by less than 5% from the calculations using equation D.3.

Using equation D.3 and stopping powers taken from Northcliffe (1963) and Northcliffe and Schilling (1970) the stopping powers of a variety of lunar sample compositions for 16.5 MeV ^{19}F ions were found to vary from -8.7 keV-cm^2-μg^{-1} to -9.3 keV-cm^{2}μg^{-1}. The mean of -9.0 keV-cm^2-μg^{-1} was taken as a reasonable estimate for all of the lunar samples analyzed in this study. A value of -9.4 keV-cm^2-μg^{-1} was found for unhydrated terrestrial obsidian, with the additional H_2O content in the hydrated region resulting in a stopping power of -9.6 keV-cm^2-μg^{-1}. A stopping power of -0.21 keV-cm^2-μg^{-1} was calculated for 0.872 MeV protons in lunar materials.

A relative uncertainty of about 5 percent should be

associated with the calculated stopping powers due primarily to uncertainties in the stopping power data and interpolations used to obtain the $[dE/d(\rho x)]_i$ in equation D.3. Although 10 percent deviations from Bragg's rule have been reported for SiO_2 (Thompson and Mackintosh, 1971), other studies indicate that deviations are not larger than ∿2 percent for SiO_2 or Al_2O_3 (Nicolet and Feng, 1973). Thus the possibility of deviations from Bragg's rule have been disregarded for the purposes of this study.

E. Implantation of Interplanetary Ions in Lunar Samples

Since most implantation experiments in the laboratory are performed with a monoenergetic beam at normal incidence and a limited exposure, the resulting depth distributions of the implanted ions are usually considered to represent a distribution in projected range. This is not the case for lunar samples, where even neglecting modifications due to diffusion, the distributions of implanted ions are governed by the combined effects of an extended spectrum of implantation energies, the angular distribution of the incident ions, and the gradual erosion of sample surfaces. In the following, we will consider these effects, assuming that diffusion plays a negligible role so that all implanted ions are frozen into the solid at the end of their range.

First, consider the case of a monoenergetic beam of protons normally incident on a lunar sample with energy E_o and a corresponding projected range R_o. Neglecting range straggling and the effects of

erosion, the resultant H distribution would be given by

$$H_N(x) = \phi_o \tau \delta(x - R_o) \qquad (E.1)$$

where ϕ_o is the incident flux, τ is the irradiation time, and x is the depth in the sample. The effects of erosion can be accounted for by replacing x by $x - v(t - t_o)$ where v is the erosion rate (assumed constant) and t is the time extending from the beginning of the irradiation at $t = 0$ to its termination at $t = t_o$. Integrating over t gives

$$H_N(x) = \phi_o \int_o^{t_o} \delta(x - R_o - v[t - t_o])dt,$$

hence,

$$H_N(x) = \frac{\phi_o}{v}[U(x - R_o + vt_o) - U(x - R_o)], \qquad (E.2)$$

where U(x) is the Heaviside step function. Assuming that the irradiation time is long enough to erode a layer of thickness greater than R_o (i.e., $t_o > R_o/v$), an equilibrium (independent of t_o) distribution will result, given by

$$H_N(x) = \frac{\phi_o}{v}[U(x) - U(x - R_o]. \qquad (E.3)$$

Thus, the equilibrium distribution for a monoenergetic, normally incident proton beam is a constant H content ($= \phi_o/v$) extending from the surface to the projected range R_o. The effect of range straggling on this distribution is to smooth out the drop from the constant (ϕ_o/v) content for $x < R_o$ to zero for $x > R_o$ by

replacing $U(x - R_o)$ in equation E.3 by an error function:

$$U(x - R_o) \rightarrow \frac{1}{2}\left[1 + \text{erf}\left(\frac{x - R_o}{\sqrt{2}\,\sigma_o}\right)\right],$$

where σ_o is the range straggling parameter.

Normal incidence for a sample from one of the Apollo sites is a good approximation for ions reflected toward the moon from the Earth's bowshock. For ions incident from a solar direction, however, the rotation of the moon results in the equivalent of isotropic incidence in a half-plane. Once again neglecting range straggling and erosion, the resultant H distribution would be

$$H_S(x) = \frac{\phi_o}{2\pi}\tau \int_{-\frac{\pi}{2}}^{\frac{\pi}{2}} \delta(x - R_o \cos\theta)\,d\theta ,$$

where θ is the angle of incidence measured from the normal. Integrating gives

$$H_S(x) = \frac{\phi_o\,\tau}{\pi\sqrt{R_o^2 - x^2}}\,[U(x) - U(x - R_o)], \qquad (E.4)$$

and including erosion in the same manner as above results in

$$H_S(x) = \frac{\phi_o}{2v}\left[1 - \frac{2}{\pi}\sin^{-1}\left(\frac{x}{R_o}\right)\right]\left[U(x) - U(x - R_o)\right] . \qquad (E.5)$$

For completeness, we also consider the opposite extreme from normal incidence, that of an isotropic angular distribution in three dimensions. We take ϕ_o to be the proton flux per 4π steradians at energy E_o. Neglecting straggling and erosion,

$$H_I(x) = \frac{\phi_o \tau}{2} \int_0^{\frac{\pi}{2}} \delta(x - R_o \cos\theta) \sin\theta \, d\theta$$

which results in

$$H_I(x) = \frac{\phi_o \tau}{2R_o} [U(x) - U(x - R_o)]. \qquad (E.6)$$

With erosion, this leads finally to the equilibrium distribution

$$H_I(x) = \frac{\phi_o}{2v} \left(1 - \frac{x}{R_o}\right) [U(x) - U(x - R_o)] \, . \qquad (E.7)$$

The equilibrium distributions resulting from these conditions (neglecting range straggling) are plotted in Figure 25 for comparison. It should be noted that the shape of the equilibrium distribution for monoenergetic protons incident from a solar direction ($H_S(x)$) is intermediate between the corresponding distributions for normal ($\frac{1}{2} H_N(x)$) and isotropic ($H_I(x)$) incidence.

To treat an extended spectrum of energies, one has only to select the appropriate source function and replace R_o by a range-energy relation $R(E)$ and ϕ_o by $(d\phi.dE)$ and integrate over the

spectrum of incident energies. Hence the H distribution H(x) would be given by

$$H(x) = \int_0^\infty P(x,E)\, \frac{d\phi}{dE}\, dE \qquad (E.8)$$

where

$$P(x,E) = [U(x) - U(x - R(E))] \begin{cases} & 1/v \\ [1 - \frac{2}{\pi} \sin^{-1}(\frac{x}{R(E)})]/2v & \\ [1 - \frac{x}{R(E)}\ ]/2v & \end{cases} \qquad (E.9)$$

for normal, solar angle, and isotropic incidence respectively. The effects of straggling complicate the mathematics considerably, but if a gaussian range distribution defined by the straggling parameter $\sigma(E)$ is assumed, analytical expressions can be derived for $P(x,E)$ for both normal and isotropic incidence. For normal incidence,

$$P(x,E) = \frac{U(x)}{2v} \left[1 + \text{erf}\left(\frac{R(E) - x}{\sqrt{2}\ \sigma(E)}\right)\right] . \qquad (E.10)$$

For isotropic incidence the expression is considerably more complicated and is not given here.

F. Lunar Sample Inventory

Following is a list of all lunar samples allocated for this study:

10085,1: One brown glass fragment with 2-mm x 1.5-mm analyzed surface characterized by rough texture and small pits.

10085,31: Two brown glass fragments. 10085,31-9 appears to be a chip from a $\frac{1}{2}$ - cm glass spherule. The analyzed surface is a 2.5-mm diameter convex surface of shiny glass. 10085,31-12 was an angular fragment ∿3-mm x 5-mm which broke into two pieces subsequent to the analysis of a 3.2-mm, shiny, slightly concave surface.

15083,2: One 1.5-mm x 1.5-mm white crystalline grain (probably plagioclase) which broke into two pieces on mounting and was not analyzed.

15413,5: Two samples. 15413,5-2 is a 2-mm x 4-mm partially glazed pyroxene-rich crystalline rock fragment. The analyzed surface contained an area ∿1-mm x 3-mm rich in pyroxene. 15413,5-5 is a highly fractured 1.5-mm x 2.5-mm fragment which appeared to be essentially all plagioclase.

15533,4: One 3-mm x 2.5-mm glass coated breccia fragment.

15015,39: Two surface glass chips from the unpitted lunar bottom of rock 15015, a glass coated breccia. The glass surfaces are 5 mm x 4 mm for 15015,39-1 and 7 mm x 7 mm for 15015,39-2. The analyzed interior surfaces are dark matrix breccia.

15059,28: One surface glass chip from the unpitted lunar bottom of rock 15059, a glass coated breccia similar to 15015. A 5-mm x 6-mm glass coated area was obtained for analysis by breaking the original 15059,28 sample into two roughly equal pieces.

15059,32: One surface glass chip from the lightly pitted lunar top of rock 15059. The 4-mm x 4-mm glass coated area was analyzed.

64455,24: One surface glass chip from rock 64455. Exterior surface is 1-cm x 1-cm smooth black glass. Interior surface is light colored rock.

64455,33: Two light colored anorthositic rock surface chips, 0.38 grams total weight.

65315,6: Three black surface glass chips from rock 65315, only one analyzed. Exterior 12-mm x 7-mm surface contained two possible impact pits visible to the naked eye. Interior surface is mostly white anorthosite with some

patches of black glass. The 1-mm thick glass cracked in its mount, but the pieces stayed together for exterior surface analysis. Interior surfaces of two of the three pieces were analyzed separately.

65315,7: One large (13-mm x 16-mm) rounded surface anorthosite chip not mounted for analysis because of large size.

65315,8: One large (10-mm x 10-mm x 7-mm), blocky surface anorthosite chip. The surface analyzed is a clear white interior surface. The sample was too large to mount for analysis of the exterior surface.

65315,20: Two black surface glass chips, only one (~5 x 4 mm) analyzed, showing some white anorthosite on both interior and exterior surfaces.

66044,8: One 3-mm x 5-mm blocky light-colored anorthosite fragment returned in sealed rock box. Surface A contains one gray area which may be glass, while Surface B is essentially all anorthosite.

68124,3: One 5-mm dark brown glass spherule (~0.2 gram) returned in sealed rock box. Surface B has a few small pits, but Surface A is smooth and shiny.

68124,10: One 7-mm x 5-mm white anorthosite fragment with translucent areas which may be single feldspar crystals. This sample was also returned in the sealed rock box.

68815,27: One 1-cm x 7-cm surface breccia chip from rock 68815 returned in sealed rock box. The exterior surface contains a light-colored but inhomogeneous region about 1.5-mm x 4-mm surrounded by dark matrix material. The interior surface is similar dark matrix material.

REFERENCES

Ajzenberg-Selove, F. and Lauritsen, T. 1959, Nucl. Phys. 11, 1.

Ajzenberg-Selove, F. 1970, Nucl. Phys. A152, 1.

Ajzenberg-Selove, F. 1971, Nucl. Phys. A166, 1.

Ajzenberg-Selove, F. 1972, Nucl. Phys. A190, 1.

Albee, A. L. 1971, private communication.

Amsel, G. and Samuel, D. 1962, J. Phys. Chem. Solids 23, 1707.

Amsel, G., Béranger, G., de Gélas, B. and Lacombe, P. 1968, J. Appl. Phys. 39, 2246.

Bame, S. J., Asbridge, J. R., Hundhausen, A. J. and Montgomery, M. C. 1970, J. Geophys. Res. 75, 6360.

Behrman, C., Crozaz, G., Drozd, D., Hohenberg, C., Ralston, C., Walker, R. and Yuhas, D. 1973, in Lunar Science IV, Lunar Science Institute, Houston, p. 54.

Bibring, J. P., Duraud, J. P., Durrieu, L., Jouret, C., Maurette, M. and Meunier, R. 1972, Science 175, 753.

Bikerman, J. J. 1970, Physical Surfaces, Academic Press, New York, p. 190.

Borg, J., Maurette, M., Durrieu, L. and Jouret, C. 1971, Proc. Second Lunar Sci. Conf. 3, 2027.

Brückner, R. 1971, J. Non-Crystalline Solids 5, 177.

Burnett, D., Hohenberg, C., Maurette, M., Monnin, M., Walker, R. and Woolum, D. 1973, in Apollo 16: Preliminary Science Report, NASA, Washington, D. C., p. 15-19.

Cadenhead, D. A., Wagner, N. J., Jones, B. R. and Stetter, J. R. 1972, Proc. Third Lunar Sci. Conf. 3, 2243.

Cadenhead, D. A., Jones, B. R., Buerget, W. G. and Stetter, J. R. 1973, in Lunar Science IV, Lunar Science Institute, Houston, p. 109.

Chao, C. Y., Tollestrup, A. V., Fowler, W. A. and Lauritsen, C. C. 1950, Phys. Rev. 79, 108.

Choudhury, A., Palmer, D. W., Amsel, G., Curien, H. and Baruch, P. 1965, Solid State Communications 3, 119.

D'Amico, J., DeFelice, J. and Fireman, E. L. 1970, Proc. Apollo 11 Lunar Sci. Conf. 2, 1029.

Dick, G. J. 1973, private communication.

Ducati, H., Kalbitzer, S., Kiko, J., Kirsten, T. and Müller, H. W. 1972, preprint, Max-Planck-Institut für Kernphysik, Heidelberg.

Eberhardt, P., Geiss, J., Graf, H., Grögler, N., Krähenbühl, U., Schwaller, H., Schwarzmüller, J. and Stettler, A. 1970, Proc. Apollo 11 Lunar Sci. Conf. 2, 1037.

El Goresy, A., Ramdohr, P. and Medenback, O. 1973, in Lunar Science IV, Lunar Science Institute, Houston, p. 222.

Endt, P. M. and Van der Leun, C. 1967, Nucl. Phys. A105, 1.

Epstein, S. and Taylor, H. P., Jr. 1970, Proc. Apollo 11 Lunar Sci. Conf. 2, 1085.

Epstein, S. and Taylor, H. P., Jr. 1971, Proc. Second Lunar Sci. Conf. 2, 1421.

Epstein, S. and Taylor, H. P., Jr. 1972, Proc. Third Lunar Sci. Conf. 2, 1429.

Ericson, J. E. 1973, private communication.

Espe, W. 1966, Materials of High Vacuum Technology, Vol. 1, "Metals and Metalloids," Pergamon Press, New York.

Fowler, W. A., Lauritsen, C. C. and Lauritsen, T. 1948, Rev. Mod. Phys. 20, 236.

Frank, L. A. 1970, J. Geophys. Res. 75, 707.

Friedman, I. and Smith, R. L. 1960, American Antiquity 25, 476.

Friedman, I., Smith, R. L. and Long, W. D. 1966, Geol. Soc. America Bull. 77, 323.

Friedman, I., Gleason, J. D. and Hardcastle, K. G. 1970, Proc. Apollo 11 Lunar Sci. Conf. 2, 1103.

Friedman, I. 1973, private communication.

Fuller, E. L., Jr., Holmes, H. F., Gammage, R. B. and Becker, K. 1971 Proc. Second Lunar Sci. Conf. 3, 2009.

Funkhouser, J., Jessberger, E., Müller, O. and Zähringer, J. 1971, Proc. Second Lunar Sci. Conf. 2, 1381.

Gammage, R. B. and Becker, K. 1971, Proc. Second Lunar Sci. Conf. 3, 2057.

Geiss, J., Eberhardt, P., Bühler, F., Meister, J. and Signer, P. 1970, J. Geophys. Res. 75, 5972.

Gibson, E. K., Jr., and Johnson, S. M. 1971, Proc. Second Lunar Sci. Conf. 2, 1351.

Grieve, R. A. F. and Plant, A. G. 1973, in Lunar Science IV, Lunar Science Institute, Houston, p. 317.

Hines, R. L. and Arndt, R. 1960, Phys. Rev. 119, 623.

Hintenberger, H., Weber, H. W.,Voshage, H., Wänke, H., Begemann, F. and Wlotza, F. 1970, Proc. Apollo 11 Lunar Sci. Conf. 2, 1269.

Hörz, F. 1971, private communication.

Huggins, M. L. and Sun, K.-H., 1943, J. Am. Ceram. Soc. 26, 4.

Hutcheon, I. D., Phakey, P. P. and Price, P. B. 1972, Proc. Third Lunar Sci. Conf. 3, 2845.

Jovanovic, S. and Reed, G. W., Jr. 1973, in Lunar Science IV, Lunar Science Institute, Houston, p. 418.

Keil, K., Bunch, T. E. and Prinz, M. 1970, Proc. Apollo 11 Lunar Sci. Conf. 1, 561.

Kelly, R. and Brown, F. 1965, Acta Metallurgica 13, 169.

Kelly, R., Jech, Č. and Matzke, Hj. 1968, Phys. Stat. Sol. 25, 641.

Kirsten, T., Müller, O., Steinbrunn, F. and Zähringer, J. 1970, Proc. Apollo 11 Lunar Sci. Conf. 2, 1331.

Kirsten, T., Steinbrunn, R. and Zähringer, J. 1971, Proc. Second Lunar Sci. Conf. 2, 1651.

Kirsten, T., Deubner, J., Horn, P., Kaneoka, I., Kiko, J., Schaeffer, O. A. and Thio, S. K. 1972, Proc. Third Lunar Sci. Conf. 2, 1865.

Lee, R., Leich, D., Tombrello, T., Ericson, J. and Friedman, I. 1973, in preparation.

Leich, D. A. and Tombrello, T. A. 1973, Nucl. Inst. and Meth. 108, 67.

Leich, D. A., Tombrello, T. A. and Burnett, D. S. 1973a, Earth Planet Sci. Lett. 19, 305.

Leich, D. A., Tombrello, T. A. and Burnett, D. S. 1973b, to be published in Proc. Fourth Lunar Sci. Conf. 2.

Lindhard, J., Scharff, M. and Schiøtt, H. E. 1963, Mat. Fys. Medd. Dan. Videnskab. Selskab 33, no. 14, 1.

Lord, H. C. 1968, J. Geophys. Res. 73, 5271.

LRL (Lunar Receiving Laboratory) 1971, Lunar Sample Information Catalog, Apollo 15, NASA report MSC 03209.

LRL (Lunar Receiving Laboratory) 1973, private communication.

LSPET (Lunar Sample Preliminary Examination Team) 1969, Science 165, 1211.

Maccabee, H. D., Raju, M. R. and Tobias, C. A. 1968, Phys. Rev. 165, 469.

Macdougall, D., Rajan, R. S., Hutcheon, I. D. and Price, P. B. 1973, in Lunar Science IV, Lunar Science Institute, Houston, p. 490.

Mann, F. M., Mak, H.-B. and Denkin, N. M. 1973, private communication.

Marshall, R. R. 1961, Geol. Soc. American Bull. 72, 1493.

Matzke, Hj. 1966, Phys. Stat. Sol. 18, 285.

Matzke, Hj. and Whitton, J. L. 1966, Can. J. Phys. 44, 995.

Möller, E. and Starfelt, N. 1967, Nucl. Inst. and Meth. 50, 225.

Morey, G. W. 1954, The Properties of Glass, Reinhold Publishing Corporation, New York.

Morrison, D. A., McKay, D. S. and Heiken, G. H. 1972, Proc. Third Lunar Sci. Conf. 3, 2767.

Nicolet, M. A. and Feng, J. 1973, private communication.

Northcliffe, L. C. 1963, Ann. Rev. Nucl. Sci. 13, 67.

Northcliffe, L. C. and Schilling. R. F. 1970, Nuclear Data Tables Section A 7, 233.

Ollerhead, R. W., Almqvist, E. and Kuehner, J. A. 1966, J. Appl. Phys. 37, 2440.

Padawer, G. M. and Schneid, E. J. 1969, Amer. Nucl. Soc. Trans. 12, 493.

Padawer, G. M. 1970, Nucl. Appl. and Tech. 9, 856.

Padawer, G. M. 1973, private communication.

Palmer, D. W. 1965, Nucl. Instr. and Meth, 38, 187.

Patterson, J. H., Turkevich, A. L., Franzgrote, E. J., Economou, T. E. and Sowinski, K. P. 1970, Science 168, 825.

Phakey, P. P., Hutcheon, I. D., Rajan, R. S. and Price, P. B. 1972, Proc. Third Lunar Sci. Conf. 3, 2905.

Phillips, W. R. and Read, F. H. 1963, Proc. Phys. Soc. 81, 1.

Porat, D. I. and Ramavataram, K. 1960, Proc. Phys. Soc. 76, 438.

Reed, G. W., Jr. 1964, Geochim. Cosmochim. Acta 28, 1729.

Reed, G. W., Jr. 1971, in Handbook of Elemental Abundances in Meteorites, B. Mason, ed., Gordon and Breach Science Publishers, New York, p. 103.

Schiøtt, H. E. 1966, Mat. Fys. Medd. Dan. Videnskab. Selskab 35, no. 9, 1.

Schiøtt, H. E. 1970, Radiation Effects 6, 107.

Stauber, M. C., Padawer, G. M., Brandt, W., D'Agostino, M. D., Kamykowski, E. and Young, D. A. 1973, submitted for publication in Proc. Fourth Lunar Sci. Conf.

Stevels, J. M. 1948, Progress in the Theory of the Physical Properties of Glass, Elsevier Publishing Company, New York.

Sutton, R. L., Hait, M. H., Larson, K. B., Swann, G. A., Reed, V. S. and Schaber, G. G. 1972, Documentation of Apollo 15 Samples, U.S.G.S. Interagency Report: Astrogeology 47.

Taylor, L. A. 1973, in Lunar Science IV, Lunar Science Institute, Houston, p. 715.

Thompson, D. A. and Mackintosh, W. D. 1971, J. Appl. Phys. 42, 3969.

Tombrello, T. A. and Leich, D. A. 1971, IEEE Trans. on Nucl. Sci. NS-18, 164.

Turkevich, A. L. 1973, private communication.

Whitton, J. L., Mitchell, I. V. and Winterbon, K. B. 1971, Can. J. Phys. 49, 1225.

Wilshire, H. G., Stuart-Alexander, D. E. and Jackson, E. D. 1973, in Lunar Science IV, Lunar Science Institute, Houston, p. 784.

Winterbon, K. B., Sigmund, P. and Sanders, J. B. 1970, Mat. Fys. Medd. Dan. Videnskab. Selskab 37, no. 14, 1.

Wolfe, J. H. 1972, in Solar Wind, NASA SP-308, Washington, D. C.

Young, E. J., Myers, A. T., Munson, E. L. and Conklin, N. M. 1969, U.S.G.S. Professional Paper 650-D, p. 84.

Zeller, E. J., Dreschhoff, G. and Kevan, L. 1968, Modern Geology 1, 141.

TABLE 1

Sample Type	Implantation Current (nA)	Implantation Dose ($\times 10^{15}$ ions/cm^2)	R_P (μg/cm^2)	R_M (μg/cm^2)	FWHM (μg/cm^2)
Crystalline Quartz	75	5	35	35	23
	150	10	39	39	47
	150	10	34	37	41
	200	9	24	35	35
	200	16	39	44	45
Fused Silica	60	6	50	45	47
	100	8	35	33	35
	200	9	35	41	59
Feldspar (Ca-rich)	150	10	33	43	45
	200	9	34	38	46
	200	9	40	44	50
	200	5	34	33	35

Most probable range (R_P), median range (R_M) and full-width at half-maximum (FWHM) are given for samples implanted with ~12 keV protons. Calculations from Schiøtt (1966) predict a mean range of 34 μg/cm^2 for SiO_2 and 35 μg/cm^2 for the feldspar composition, with FWHM's of 25 μg/cm^2 and 26 μg/cm^2, repectively (see text, page 20).

TABLE 2

Element Analyzed	Reaction Used	E_R (MeV)	γ-ray Energy (MeV)	Sensitivity ($\times 10^{-13}$)
H	$^{1}H(^{19}F,\alpha\gamma)^{16}O$	16.45	6.1, 6.9, 7.1	51
F	$^{19}F(p,\alpha\gamma)^{16}O$	0.872	6.1, 6.9, 7.1	6.5
Na	$^{23}Na(p,\gamma)^{24}Mg$	1.318	11.6, 13.0	0.03
Aℓ	$^{27}Aℓ(p,\gamma)^{28}Si$	0.992	10.8	0.01

Resonant nuclear reactions used for analysis of H, F, Na and Aℓ are given along with the incident ion energy and the energy of the principal characteristic γ-ray reaction products. In addition, the reaction sensitivity, defined as the thick target yield per incident ion for a quartz target containing 1 ppm by weight of the particular target atoms, is also given for each reaction (see text, page 22).

TABLE 3

Hydrogen depth profile data summary. The "surface" H concentrations pertain to observed peaks within ~300 Å of the surface. The total H content of the 0-0.4 μm deep measured region, expressed as a surface density, does not include the amounts identified as "surface" H, so the total H observed is the sum of the values in the first two columns. The H content, expressed in ppm H by weight (100 ppm is equivalent to 1.55×10^{20} H atoms/cm^3 assuming a nominal density of 2.6 g/cm^3), is also given for depths of 0.1 μm and 0.4 μm. The profiles are characterized by the depth x_p at which the peak H content is observed and the full-width at half-maximum (FWHM) of the distribution. (The apparent broadening due to the resonance width Γ_1 has been removed in the calculation of the latter quantity.) The size of the fused silica collimator used with each target is also listed. The fraction of the beam hitting the sample is estimated as 0.6 ± .2 for the 2.0-mm size, 0.8 ± .2 for the 2.4-mm size, $1.0 \pm {}^{0}_{.2}$ for the 3.2-mm size, and 1.0 for the 4.5-mm size and the samples without collimators. Uncertainties in the H concentration are ± 10% with lower limits of $\pm 0.5 \times 10^{15}$/cm^2 and ± 20 ppm (see text, Section III, Part A).

TABLE 3

Sample	H content			
	Surface ($\times 10^{15}$ cm^{-2})	0-0.4μm ($\times 10^{15}$ cm^{-2})	at x=0.1μm (ppm)	at x=0.4μm (ppm)
10085,1	<2	19	370	120
10085,31-9[a]	<0.5	9	160	80
10085,31-12[a]	<3	55	1500	300
15413,5-2[a]	<1	17	400	80
15413,5-5	<0.5	4	70	30
15533,4-1	0.5	5	80	60
15015,39-1	~10	2	100	20
15015,39-1(int.)	2	3	50	40
15015,39-2	2	2	30	30
15015,39-2(int.)	2	3	40	40
15059,28	4	3.5	70	50
15059,32	4	5	120	40
64455,24	3	3	90	30
64455,24(int.)	1	2.5	40	30
64455,33-1	6	3	100	50
64455,33-1(int.)	4	2.5	50	30
64455,33-2	3	2.5	60	30
64455,33-2(int.)	2	2.5	40	30
65315,6*	0.5	5	100	40
65315,6(int.)*[b]	1.5	2	40	30
65315,8(int.)*	0.5	1	10	0
65315,20*	1.5	7	150	10
65315,20(int.)*	3	3	80	30
66044,8-A*	0.5	5	90	50
66044,8-B	2	6	100	<100
68124,3-A*	1	2	30	10
68124,3-B	1	2	30	10
68124,10-A*	<0.5	3	60	30
68124,10-B	1	3	60	30
68815,27	~3	23	500	150
68815,27(int.)	1.5	1	30	20

TABLE 3 (continued)

x_p (μm)	FWHM (μm)	Collimator size (mm)	Sample
0.09 ± .03	0.27 ± .07	2.0	10085,1
0.13 ± .05	0.22 ± .10	2.4	10085,31-9
0.11 ± .02	0.22 ± .03	3.2	10085,31-12
0.09 ± .03	0.20 ± .04	2.4	15413,5-2
0.07 ± .03	0.20 ± .05	2.0	15413,5-5
∿0.1	>0.4	2.4	15533,4-1
<0.02	<0.08		15015,39-1
<0.02	<0.05		15015,39-1(int.)
<0.02	0.04 ± .02		15015,39-2
<0.02	<0.05		15015,39-2(int.)
<0.02	0.02 ± .02		15059,28
<0.03	0.03 ± .03	3.2[c]	15059,32
<0.02	<0.05		64455,24
<0.02	<0.05		64455,24(int.)
<0.02	0.05 ± .03		64455,33-1
<0.02	<0.05		64455,33-1(int.)
<0.03	<0.05		64455,33-2
<0.03	<0.05		64455,33-2(int.)
0.11 ± .05	0.22 ± .05		65315,6
<0.03	<0.05		65315,6(int.)
<0.03	<0.05		65315,8(int.)
<0.05	0.15 ± .05		65315,20
<0.03	0.08 ± .04		65315,20(int.)
<0.05	0.15 ± .03	3.2[c]	66044,8-A
<0.03	>0.4	3.2[c]	66044,8-B
<0.03	<0.05	4.5	68124,3-A
<0.03	<0.05	4.5	68124,3-B
<0.05	>0.4		68124,10-A
<0.05	0.12 ± .05		68124,10-B
0.03 ± .02	0.18 ± .02		68815,27
<0.02	<0.05		68815,27(int.)

TABLE 3 (continued)

* F distribution measured prior to H distribution.

a Ultrasonic rinse in high-purity acetone prior to analysis.

b Values given are averages of measurements on two separate pieces of this sample.

c Collimator material is pyrex rather than fused silica. The small H content of the pyrex may contribute to the measured H for these samples.

int.: interior

TABLE 4

F distribution data summary for Apollo 16 samples. The F content is given for a layer extending from the surface to ∿0.5 μm deep and for a layer extending from ∿0.5 μm deep to ∿1 μm deep. Uncertainties are ± 10% with a lower limit of ± 20 ppm. The apparent depth x_p at which the peak F concentration is observed is given along with the FWHM of the measured distribution. The surface potential of the sample under irradiation, as measured using the reaction $^{27}Al(p,\gamma)^{28}Si$, is also given for several of these samples (see text, Section III, Part A).

int.: interior

n.d.: not determined

* F distribution measured prior to H analysis.

TABLE 4

Sample	F Content 0-0.5 μm (ppm)	F Content 0.5-1.0 μm (ppm)	x_p (μm)	FWHM (μm)	Surface Potential (kV)
64455,24	270	70	0.35	0.22	n.d.
64455,24 (int.)	70	50	0.05	0.18	n.d.
64455,33-1	210	50	0.05	0.10	n.d.
64455,33-1 (int.)	60	20	0.05	0.18	n.d.
64455,33-2	40	40	no peak observed		n.d.
64455,33-2 (int.)	100	110	no peak observed		$\leq$ 10
65315,6*	1000	480	0.10	0.17	$\leq$ 5
65315,6 (int.)*	100	50	0.12	0.30	3 ± 2
65315,8 (int.)*	140	50	0.12	0.20	$\leq$ 5
65315,20*	90	50	0.12	~0.8	n.d.
65315,20 (int.)*	160	120	0.05	0.18	n.d.
66044,8-A*	820	540	0.10	~0.4	7 ± 3
66044,8-B	1900	1400	0.03	0.08	2 ± 2
68124,3-A*	410	50	0.13	0.13	10 ± 3
68124,3-B	850	120	0.12	0.13	8 ± 3
68124,10-A*	260	130	0.09	0.20	n.d.
68124,10-B	220	100	0.17	0.20	(14)
68815,27	460	210	0.15	0.08	n.d.
68815,27 (int.)	180	120	0.05	0.18	n.d.

TABLE 5

Measurements of hydration profiles for a selection of obsidian samples. The values given for H_2O content are hydration plateau values (compare with Figs. 29 and 30). The quoted statistical uncertainties do not include a possible systematic error (of up to 5%) introduced by the estimates of detection efficiency and stopping power. The measured hydration layer thickness h, determined by the depth at which the maximum H_2O concentration gradient is observed, is also given. The uncertainties listed indicate the extent of the depth region in which the diffusion front is located, except for samples 1 - 4 where the uncertainties are determined by the resolution of the $^{1}H(^{19}F,\alpha\gamma)^{16}O$ technique. Optically measured hydration band thicknesses of thin-sections taken from the same obsidian samples are included for comparison.

TABLE 5

Sample	Source	Description	H_2O Content (percent by weight)	h(μm) $^1H(^{19}F,\alpha\gamma)^{16}O$ Technique	h(μm) Optical Technique*
1	Big Obsidian Flow, Oregon	Artificially hydrated at 75°C for 1 day	2.11 ± .14	0.09 ± .02	n.d.
2	Big Obsidian Flow, Oregon	Artificially hydrated at 75°C for 2 days	2.08 ± .13	0.11 ± .02	n.d.
3	Big Obsidian Flow, Oregon	Artificially hydrated at 75°C for 4 days	2.45 ± .14	0.14 ± .02	n.d.
4	Big Glass Mountain, California	Initial exposure August 1963	2.16 ± .12	0.19 ± .02	0.39
5	Big Obsidian Flow, Oregon		2.5 ± .1	1.2 ± .1	1.2 ± .2
6	Amapa, Nayarit, Mexico	Artifact	1.9 ± .5	1.55 ± .50	1.4 ± .2
7†	Amapa, Nayarit, Mexico	Artifact	2.15 ± .1 1.56 ± .05	0.9 ± .1 1.77 ± .27	1.7 ± .2

TABLE 5 (continued)

Sample Source	Description	H_2O Content (percent by weight)	h(μm) $^1H(^{19}F,\alpha\gamma)^{16}O$ Technique	h(μm) Optical Technique*
8 Amapa, Nayarit, Mexico	Artifact	2.3 ± .1	1.8 ± .2	1.8 ± .2
9† Amapa, Nayarit, Mexico	Artifact	2.65 ± .10 2.1 ± .1	0.53 ± .1 1.82 ± .25	2.1 ± .2
10 Borax Lake, California	Chipping waste	2.8 ± .1	1.8 ± .5	0.7 ± .5

*Data are from Ericson (1973) and Friedman (1973). The value of h given for sample 4 is not an actual measurement, but an estimate based on the known exposure time and an estimated hydration rate (Friedman, 1973).

†Two values are given for H_2O content and the hydration layer thickness h due to the appearance of two plateaus in the hydration profile. The higher H_2O content applies from the surface to the first depth and the smaller content represents the H_2O level between this depth and the larger depth.

TABLE 6

Source	H_2O Content (percent by weight)	
	Intrinsic	Hydrated
Bodie Hills, California	0.21 ± .04	2.31 ± .20
Coso, California	0.23 ± .07	2.68 ± .25
Borax Lake, California	0.35 ± .09	3.32 ± .32
East Dago Valley, California	0.66* ± .06	3.47 ± .23

*Mean of three samples from same source. Individual analyses were 0.60, 0.69, and 0.70% H_2O.

Measurement of H_2O content are given for hydrated and unhydrated samples from each of four California obsidian sources. Quoted uncertainties reflect random errors in the measurements but do not include a possible systematic error (of up to 5%) introduced by the estimates of detection efficiency and stopping power (see text, page 88).

FIGURE 1

Depth resolution of the $^{1}H(^{19}F,\alpha\gamma)^{16}O$ H analysis technique as a function of depth. The solid curve is calculated from equation A.9 in Appendix A for a quartz sample including the effects of energy straggling, the energy width of the resonance, and the energy spread of the ^{19}F ion beam (see text, page 9).

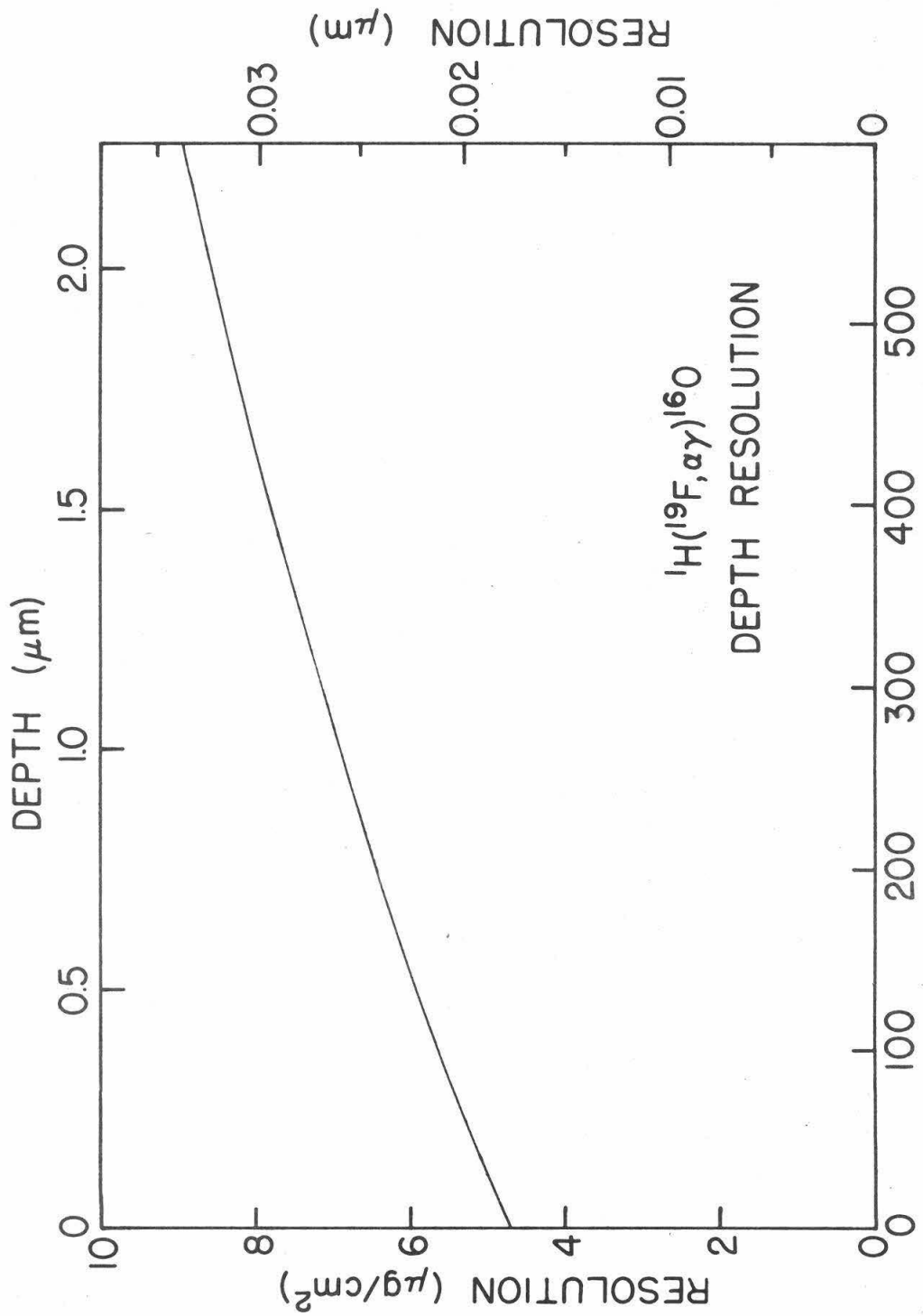
RESOLUTION (μm)
0.03
0.02
0.01
0
DEPTH (μm)
0
0.5
1.0
1.5
2.0
RESOLUTION (μg/cm²)
10
8
6
4
2
0
$^{1}H(^{19}F,\alpha\gamma)^{16}O$
DEPTH RESOLUTION
0
100
200
300
400
500
DEPTH (μg/cm²)

FIGURE 1

FIGURE 2

Schematic drawing of the target chamber vacuum system and detection electronics. The insert shows the arrangement of target mounts. (See text, page 11.)

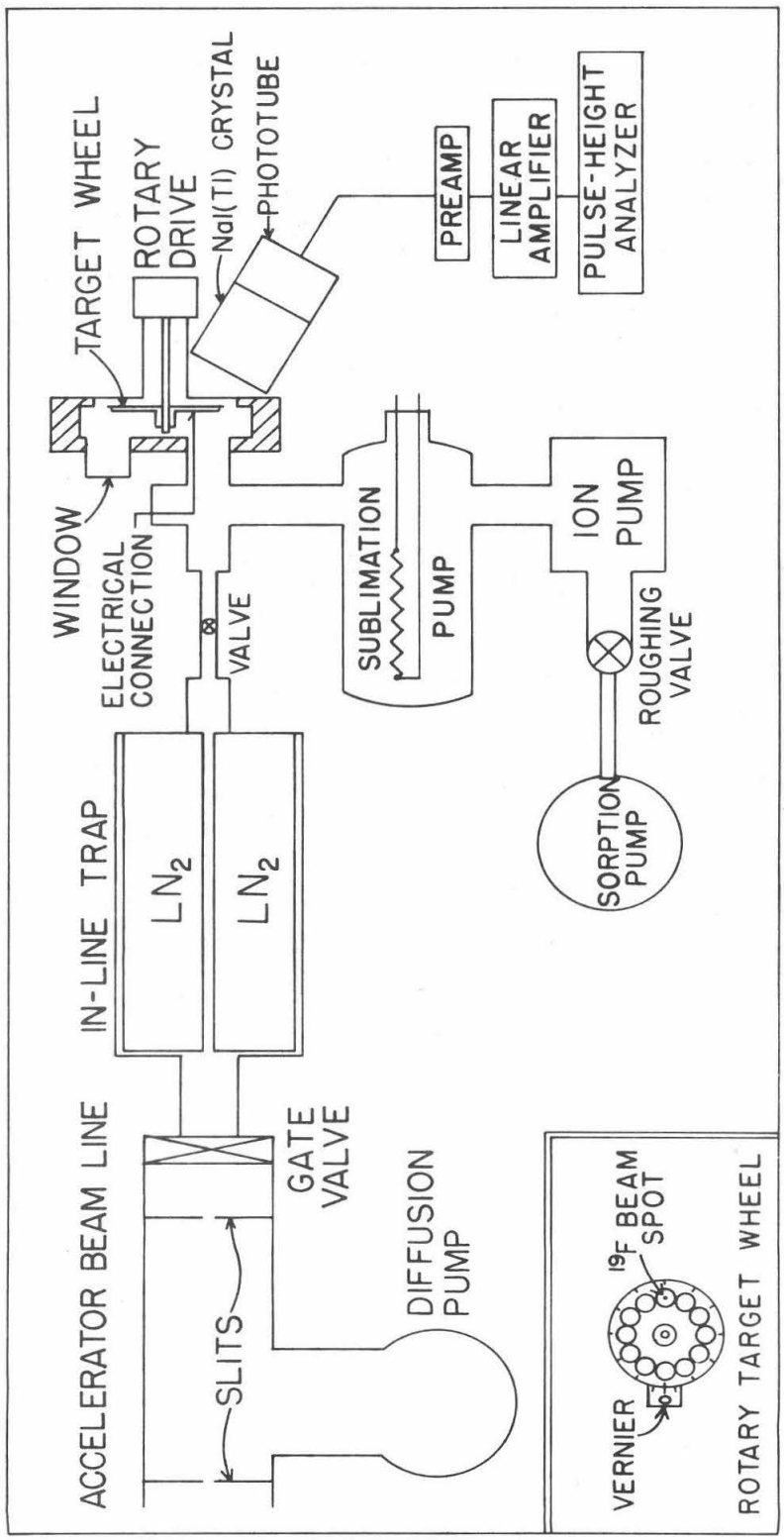
ACCELERATOR BEAM LINE
SLITS
GATE VALVE
DIFFUSION PUMP
IN-LINE TRAP
LN2
LN2
WINDOW
ELECTRICAL CONNECTION
VALVE
TARGET WHEEL
ROTARY DRIVE
NaI(Tl) CRYSTAL
PHOTOTUBE
SUBLIMATION PUMP
ION PUMP
ROUGHING VALVE
SORPTION PUMP
PREAMP
LINEAR AMPLIFIER
PULSE-HEIGHT ANALYZER
VERNIER
19F BEAM SPOT
ROTARY TARGET WHEEL

FIGURE 2

FIGURE 3

Pulse-height spectrum for 17.2-MeV ^{19}F ions incident on a sample of Belvidere Mountain chlorite. A 30-nA beam of $^{19}F^{4+}$ was used with a total integrated charge of 10 μC (see text, page 14). The positions of the full-energy peaks due to the 6.1-, 6.9- and 7.1-MeV γ rays are indicated by γ_1, γ_2 and γ_3, respectively. The single-escape and double-escape peaks following pair production from the 6.1-MeV γ ray are easily resolved at the positions indicated by γ_1-mc^2 and γ_1-2mc^2, respectively, where m is the rest mass of an electron. The positions of the single-escape peaks from γ_2 and γ_3 are also shown (the double-escape peaks are lost in the γ_1 full-energy peak). The relatively flat spectrum between channels 100 and 200 is due to Compton scattering of the three high-energy γ rays in the NaI(Tℓ) crystal. (Background is negligible above channel 100.) The peak at channel 58 is room background due to the decay of ^{40}K by electron capture to the 1.46 MeV state of ^{40}Ar.

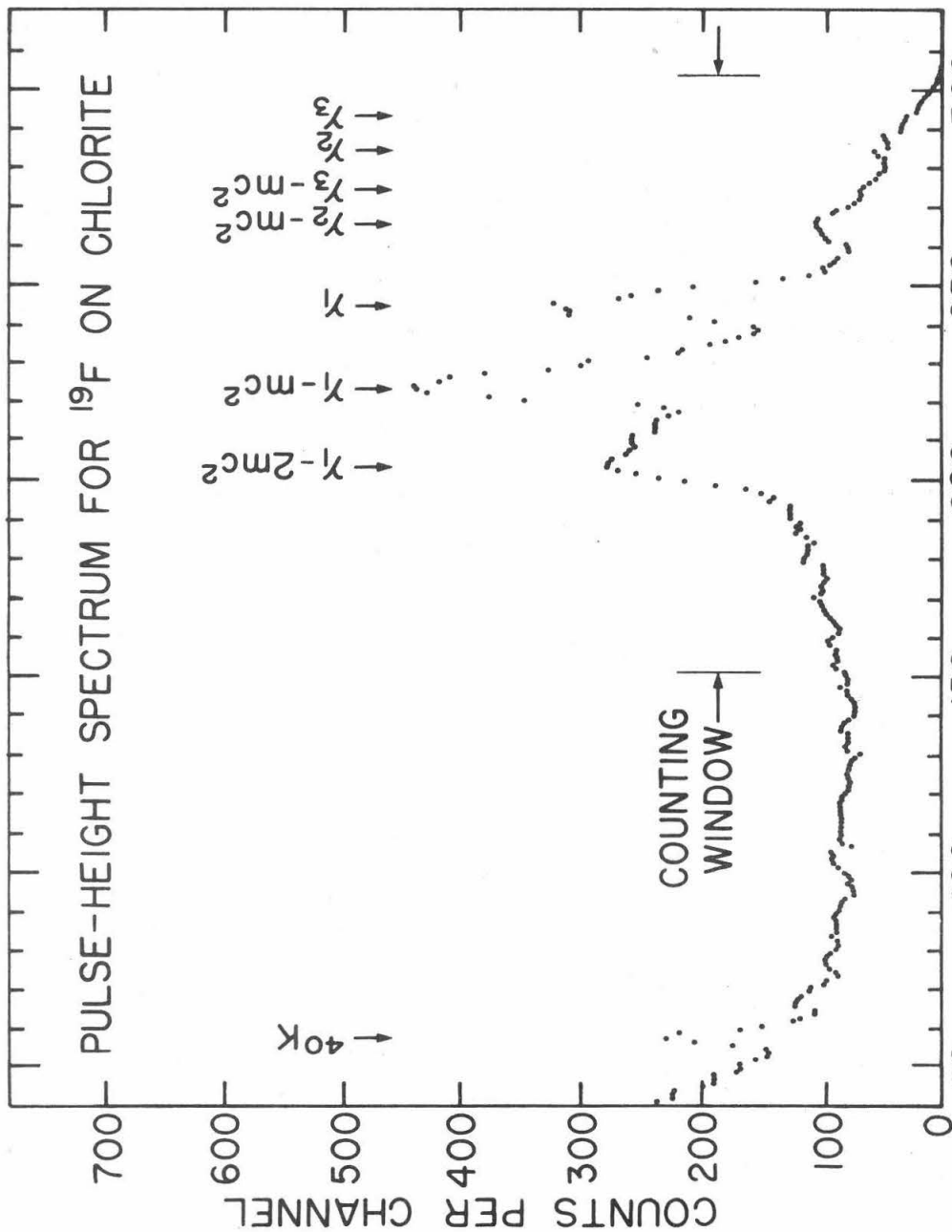
PULSE-HEIGHT SPECTRUM FOR ^{19}F ON CHLORITE
COUNTS PER CHANNEL
CHANNEL NUMBER
^{40}K
γ_1-2mc^2
γ_1-mc^2
γ_1
γ_2-mc^2
γ_3-mc^2
γ_2
γ_3
COUNTING WINDOW
0
50
100
150
200
250
300
100
200
300
400
500
600
700

FIGURE 3

FIGURE 4

The γ-ray yield versus bombarding energy for an implanted fused silica sample and for an identical non-implanted (blank) sample. The energy scale shows the resonance energy E_R subtracted from the ^{19}F beam energy E. A calculated depth scale is also shown. Error bars show statistical uncertainties. (See text, page 19.)

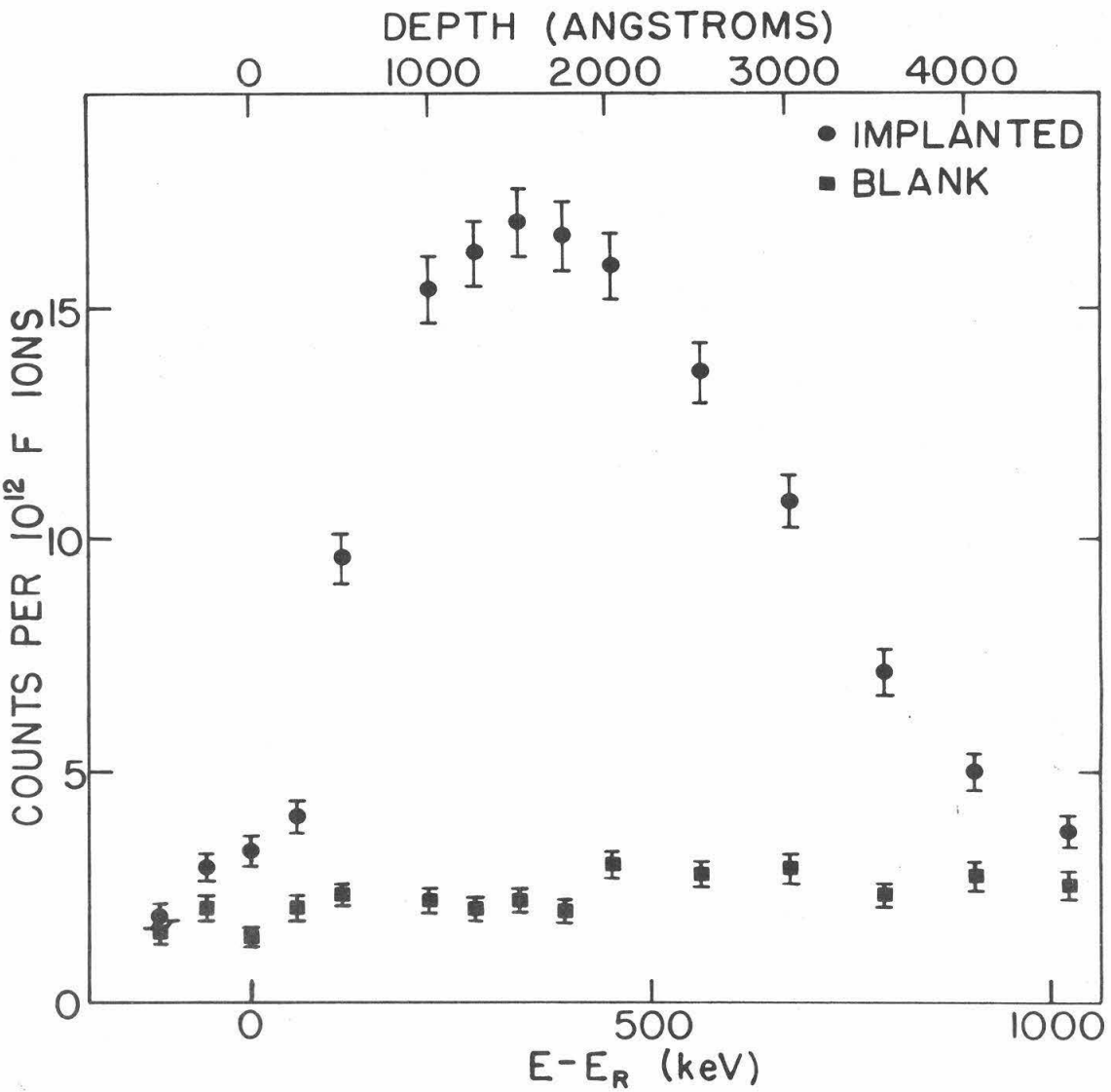

FIGURE 4

FIGURE 5

Implantation profile for fused silica sample implanted with ~12-keV protons. Experimental points were obtained by subtracting the data for the blank from the data for the implanted sample shown in Figure 4. (See text, page 19)

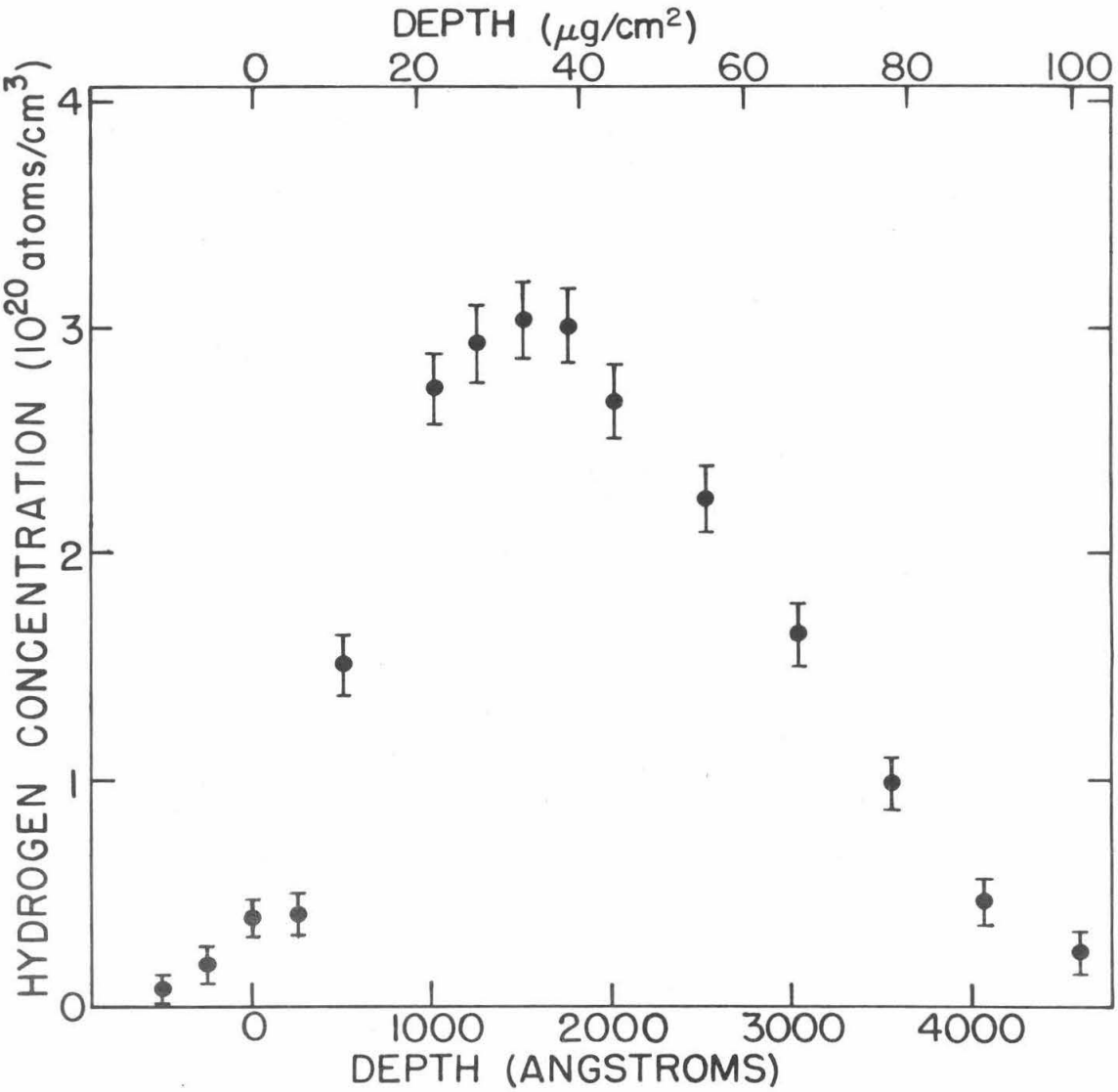
DEPTH (μg/cm²)
0
20
40
60
80
100
HYDROGEN CONCENTRATION (10²⁰ atoms/cm³)
0
1
2
3
4
0
1000
2000
3000
4000
DEPTH (ANGSTROMS)

FIGURE 5

FIGURE 6

Depth resolution as a function of depth for F, Na, and Aℓ in quartz. The resolution curve for each of these elements is indicated by the reaction used in the depth analysis measurement for that element (see text, page 22). The depth resolution for H (Figure 1) is also shown for comparison.

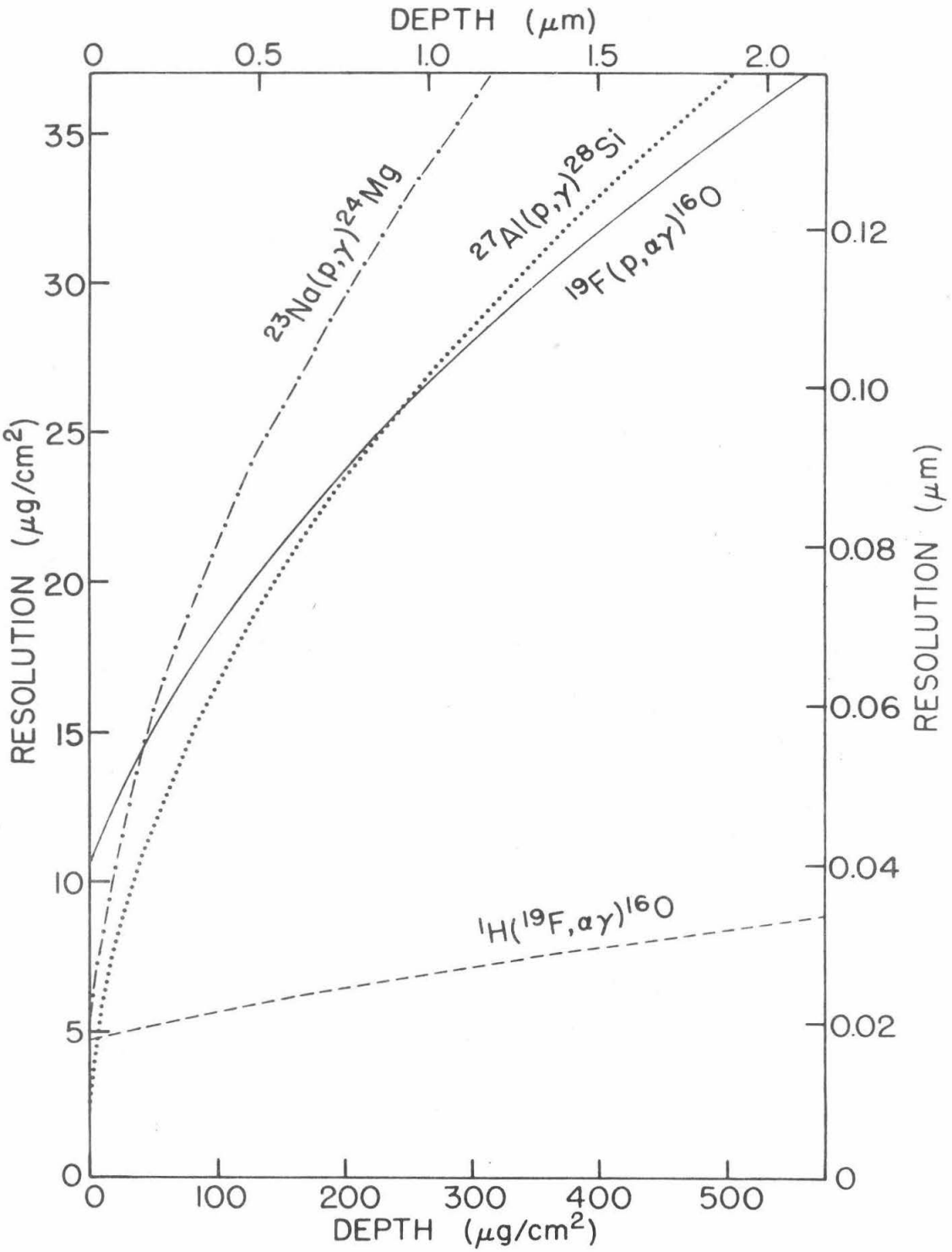
DEPTH (μm)
0
0.5
1.0
1.5
2.0
35
30
25
20
15
10
5
0
RESOLUTION (μg/cm²)
0.12
0.10
0.08
0.06
0.04
0.02
0
RESOLUTION (μm)
23Na(p,γ)24Mg
27Al(p,γ)28Si
19F(p,αγ)16O
1H(19F,αγ)16O
0
100
200
300
400
500
DEPTH (μg/cm²)

FIGURE 6

FIGURE 7

Hydrogen concentration versus depth for lunar glass sample 10085,31-12. The top scale is the difference between the ^{19}F beam energy, E, and the resonance energy E_R. The right-hand scale indicates the γ-ray counting rate. Data points for this figure and those following are number of counts with their associated statistical (1σ) uncertainties plotted against ^{19}F beam energy. Hydrogen concentration and depth scales are calculated using a nominal density of 2.6 g/cm^3. The zero point of the hydrogen concentration scale corresponds to the background counting rate, indicated by the displacement of the zero point from the bottom border of the graph. The conversion factors used to obtain the calculated scales are uncertain by about 10% due mainly to the uncertainty in the electronic stopping power of the lunar material for ^{19}F ions. Open squares are data from the third measurement of the distribution. Uncertainties are comparable to those on the data points for the original measurement, but error bars are omitted for clarity. "First run" data were taken in 50-keV steps from below the resonance energy to about 1-MeV above the resonance. "Third run" data were taken in the reverse order. (See text, page 28.)

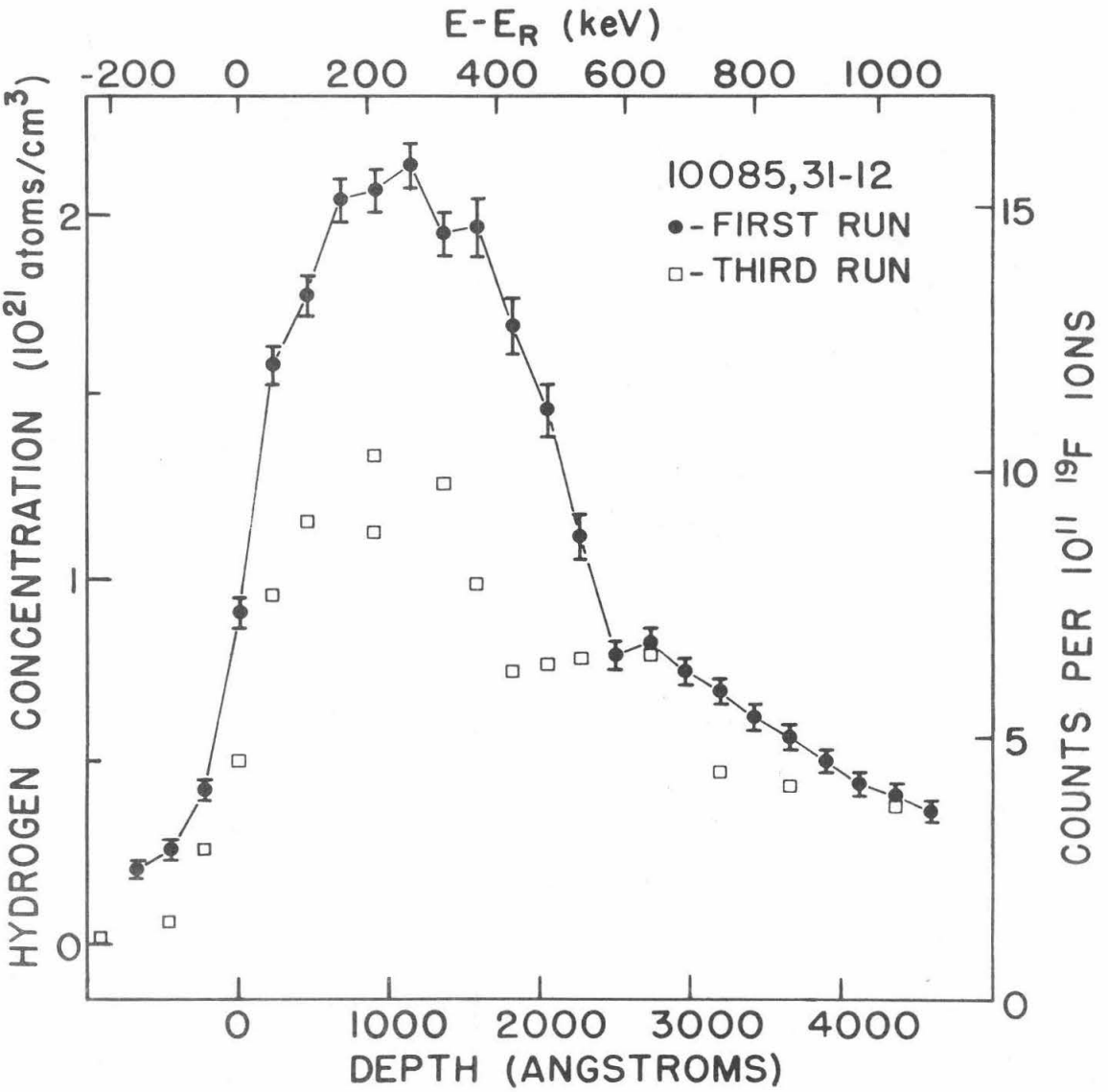
E-E$_R$ (keV)
-200
0
200
400
600
800
1000
10085,31-12
●-FIRST RUN
□-THIRD RUN
HYDROGEN CONCENTRATION (10^{21} atoms/cm^3)
COUNTS PER 10^{11} ^{19}F IONS
0
1
2
5
10
15
0
1000
2000
3000
4000
DEPTH (ANGSTROMS)

FIGURE 7

FIGURE 8

Hydrogen concentration versus depth for lunar glass fragment 10085,1. "First run" data were taken in 200-keV steps decreasing in energy (depth). "Second run" data (connected by straight lines) were taken in the reverse order. The H concentration is expressed in terms of ppm by weight as well as in atoms/cm^3. These scales have been calculated assuming the fraction of the beam hitting the sample was 0.6 with the remainder striking the 2.0-mm aperture fused silica collimator and, consequently, are uncertain by about 20%. (See text, page 30.)

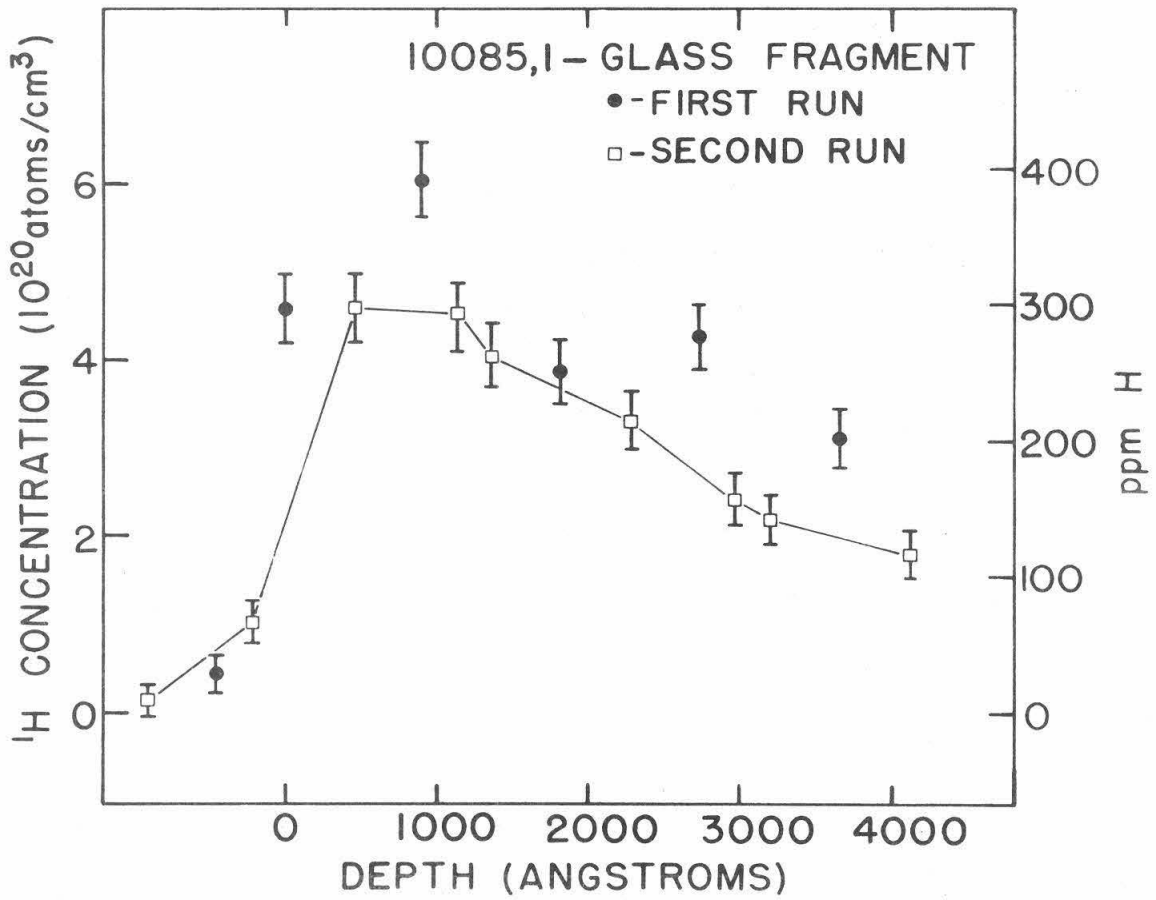
10085,1 – GLASS FRAGMENT
●-FIRST RUN
□-SECOND RUN
^{1}H CONCENTRATION (10^{20}atoms/cm^3)
ppm H
DEPTH (ANGSTROMS)
0
2
4
6
0
100
200
300
400
0
1000
2000
3000
4000

FIGURE 8

FIGURE 9

Hydrogen concentration versus depth for pyroxene-rich lunar rock fragment 15413,5-2. "First run" data were taken in steps decreasing in energy (depth). "Second run" data (connected by straight lines) were taken in the opposite direction. The fraction of the beam striking the 2.4-mm aperture fused silica collimator was estimated at 0.2 in the calculation of the H concentration scales (with a 20% uncertainty). (See text, page 31.)

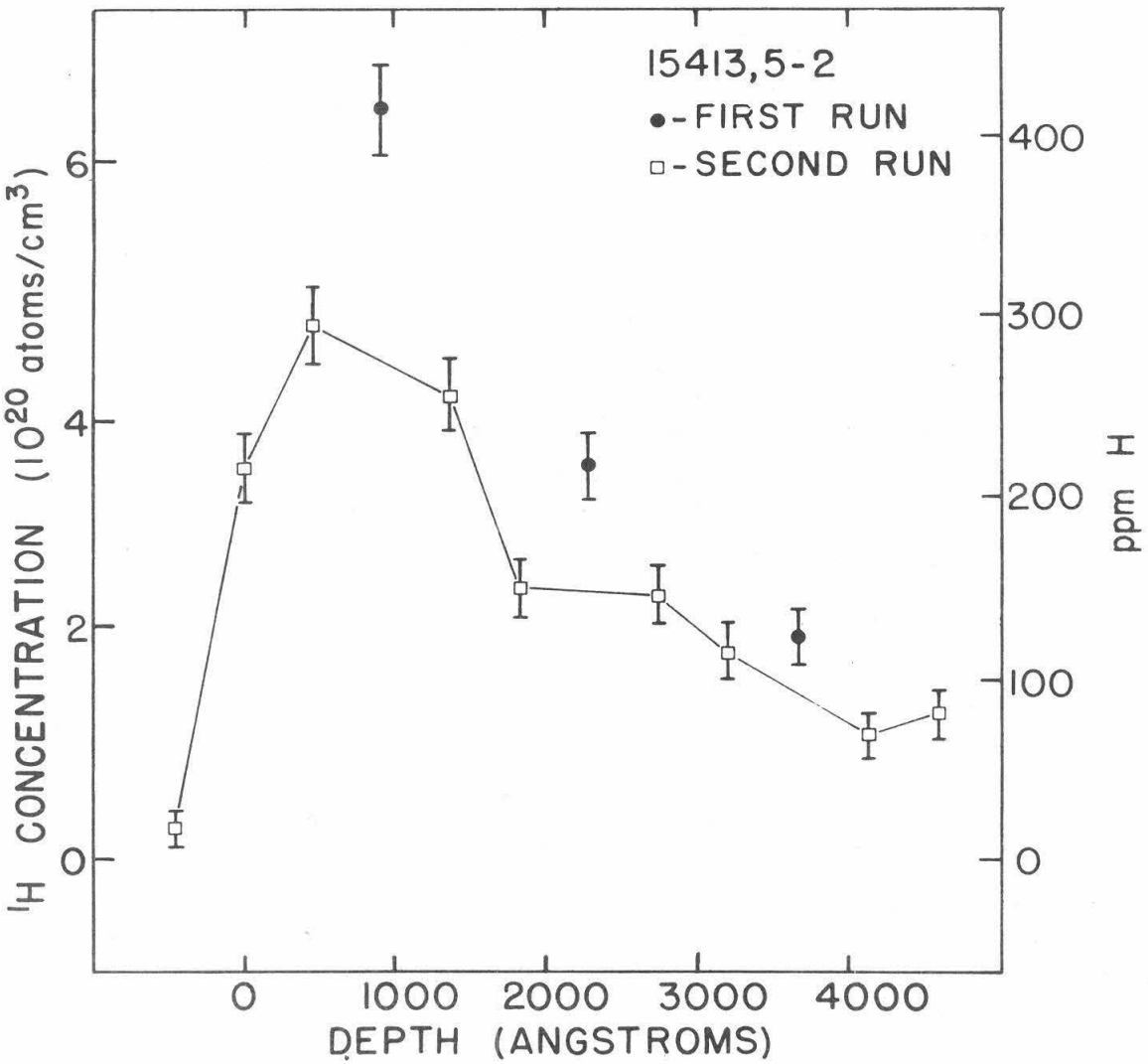
15413,5-2
●-FIRST RUN
□-SECOND RUN
^{1}H CONCENTRATION (10^{20} atoms/cm^3)
ppm H
DEPTH (ANGSTROMS)
0
2
4
6
0
100
200
300
400
0
1000
2000
3000
4000

FIGURE 9

FIGURE 10

Hydrogen concentration versus depth for glass-coated lunar rock chip 15015,39-1. This sample comes from the lunar bottom of rock 15015. The counting rate for the initial data point (taken at the resonance energy, corresponding to zero depth) was a factor of 2 too high to be included in the figure. "First run" data are in increasing energy (depth) steps, with the direction reversed for the "second run" data. (See text, page 36.)

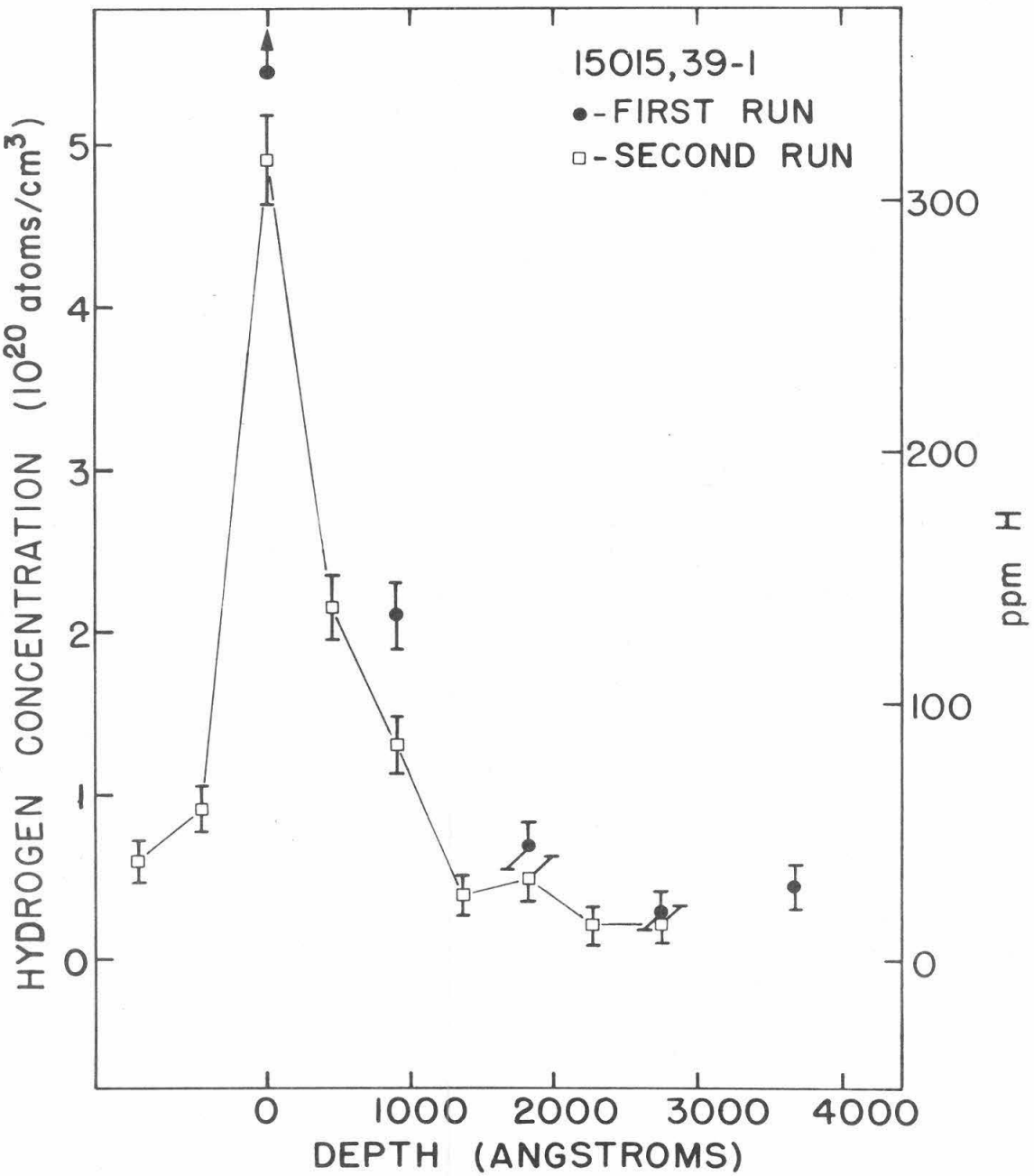
15015,39-1
●-FIRST RUN
□-SECOND RUN
HYDROGEN CONCENTRATION (10^{20} atoms/cm^3)
ppm H
DEPTH (ANGSTROMS)
0
1
2
3
4
5
0
100
200
300
0
1000
2000
3000
4000

FIGURE 10

FIGURE 11

Hydrogen concentration versus depth for glass-coated lunar rock chip 15015,39-2, from the lunar bottom of rock 15015. "First run" data were taken in increasing energy (depth) steps with the direction reversed for the "second run" data. (See text, page 36.)

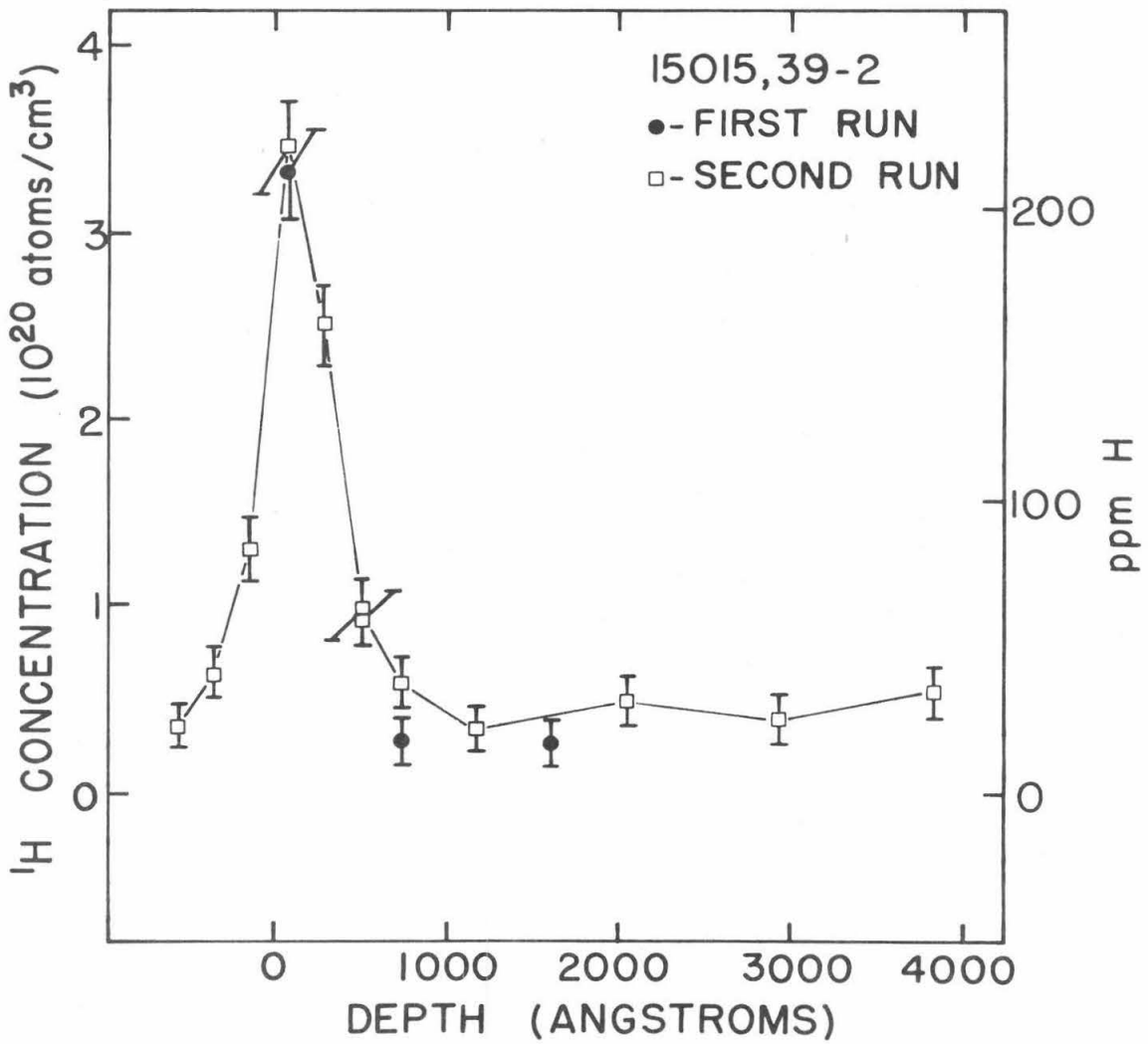
15015,39-2
●-FIRST RUN
□-SECOND RUN
^{1}H CONCENTRATION (10^{20} atoms/cm^3)
ppm H
DEPTH (ANGSTROMS)
0
1
2
3
4
100
200
1000
2000
3000
4000

FIGURE 11

FIGURE 12

Hydrogen concentration versus depth for glass-coated lunar rock chips 15059,32 and 15059,28, from the lunar top and bottom of rock 15059, respectively. The initial data point for each sample (taken at the resonance energy, corresponding to zero depth) was too large, by almost a factor of 2, to be included in the figure. The same energy was repeated for the second data point, with increasing energy (depth) steps for subsequent "first run" data on each sample. "Second run" data are in steps of decreasing energy (depth). (See text, page 37.)

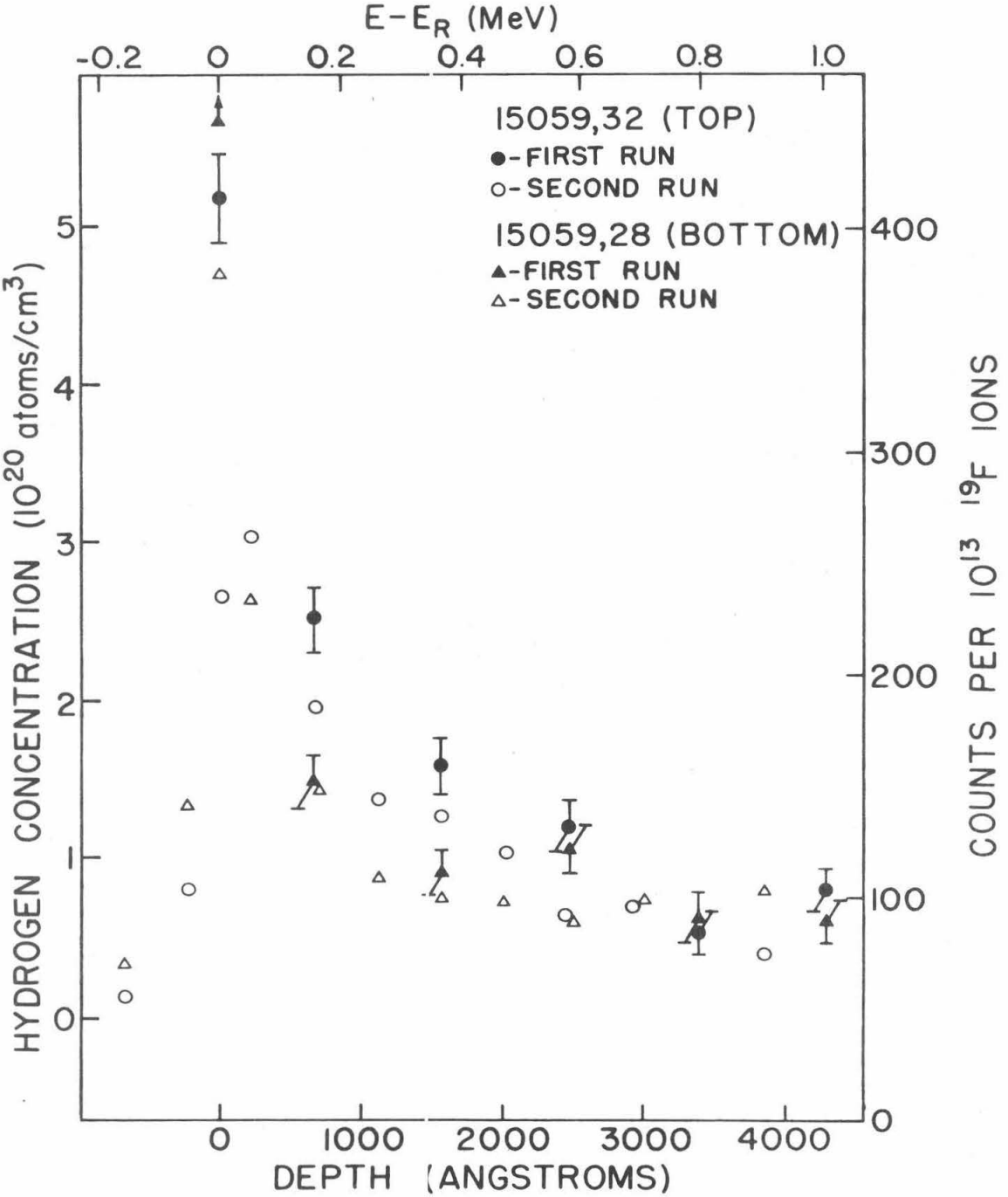
E-E_R (MeV)
-0.2
0
0.2
0.4
0.6
0.8
1.0
15059,32 (TOP)
●-FIRST RUN
○-SECOND RUN
15059,28 (BOTTOM)
▲-FIRST RUN
△-SECOND RUN
HYDROGEN CONCENTRATION (10^20 atoms/cm^3)
COUNTS PER 10^13 19F IONS
0
1
2
3
4
5
0
100
200
300
400
0
1000
2000
3000
4000
DEPTH (ANGSTROMS)

FIGURE 12

FIGURE 13

Hydrogen concentration versus depth for feldspar-rich lunar rock chip 64455,33-1, lunar exterior and interior surfaces. Error bars on the "interior surface" data are omitted for clarity, but are of the same size as for the "exterior surface" data. Straight lines have been drawn to connect the "second run" data and the last three points from the "first run" for the exterior surface. The dotted curve shows the calculated appearance (including background) of a stable H_2O monolayer ($\sim$9 $\mathring{A}^2$ per molecule corresponding to $\sim 2 \times 10^{15}$ H atoms/cm^2) on the surface of the sample. The width of the peak at zero depth reflects the resolution of this technique. The curve rises at depths greater than $\sim$4000 $\mathring{A}$ due to counts from the resonance at 17.64-MeV ^{19}F energy. (See text, page 41.)

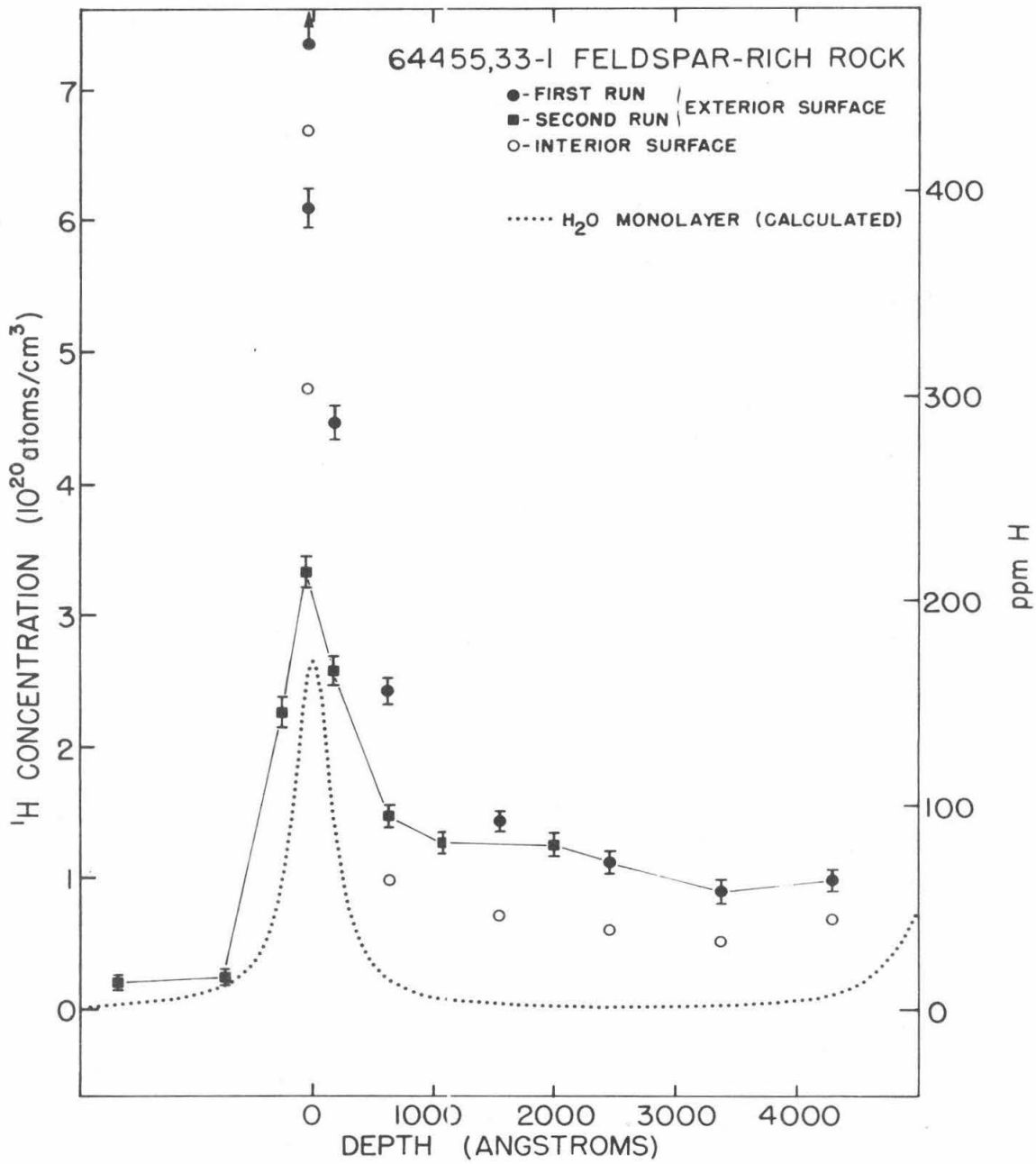
64455,33-1 FELDSPAR-RICH ROCK
●-FIRST RUN
■-SECOND RUN
EXTERIOR SURFACE
○-INTERIOR SURFACE
····· H_2O MONOLAYER (CALCULATED)
^1H CONCENTRATION (10^{20} atoms/cm^3)
ppm H
DEPTH (ANGSTROMS)
0
1000
2000
3000
4000
1
2
3
4
5
6
7
100
200
300
400

FIGURE 13

FIGURE 14

Hydrogen concentration versus depth for glass-coated lunar rock chip 64455,24 and feldspar-rich lunar rock chip 64455,33-2. Data from "interior surfaces" are also plotted for both samples, with error bars omitted for clarity. The calculated appearance of a stable H_2O monolayer is again included for comparison. (See text, page 41.)

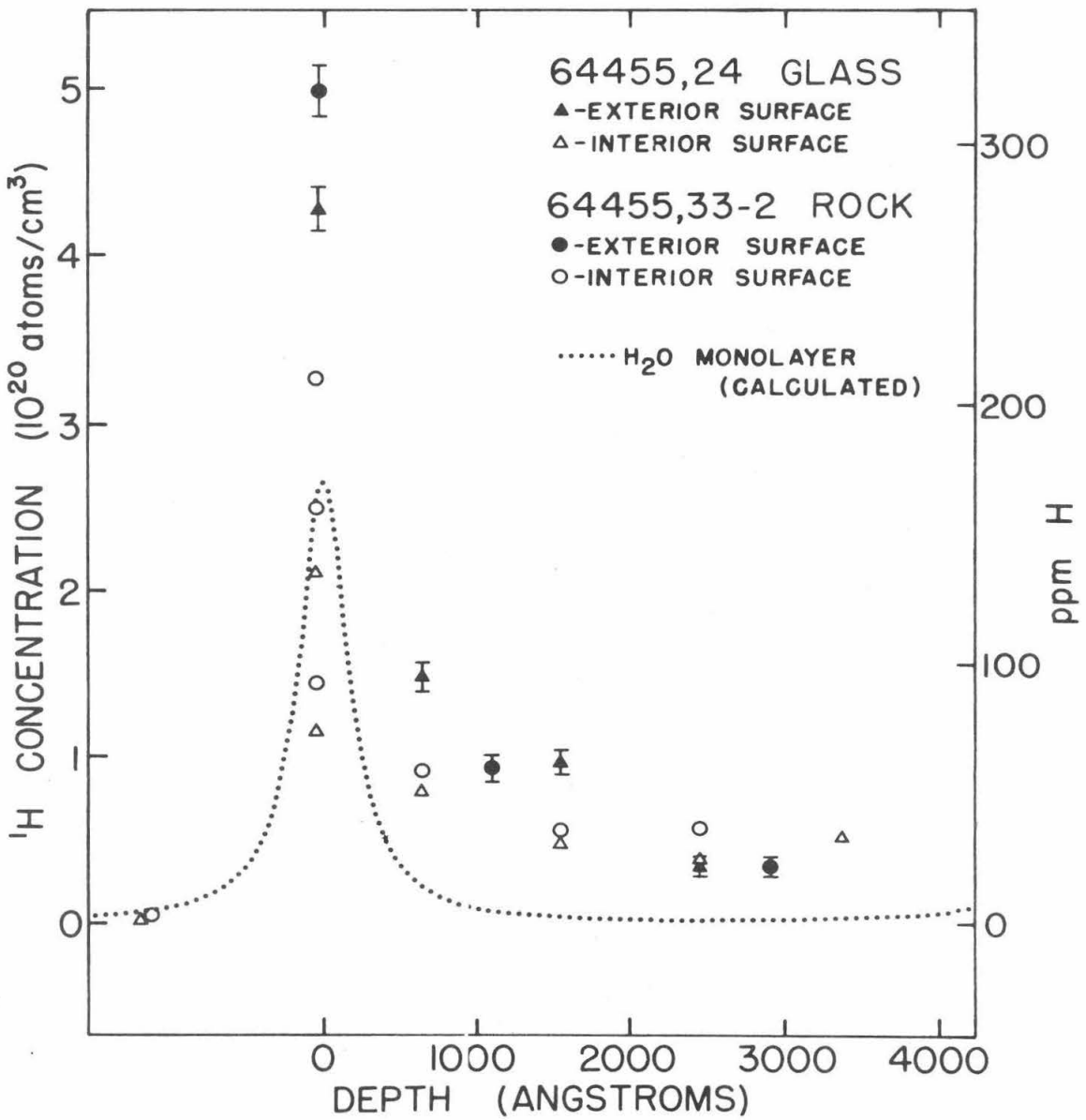
64455,24 GLASS
▲-EXTERIOR SURFACE
△-INTERIOR SURFACE
64455,33-2 ROCK
●-EXTERIOR SURFACE
○-INTERIOR SURFACE
····· H_2O MONOLAYER (CALCULATED)
^1H CONCENTRATION (10^{20} atoms/cm^3)
ppm H
DEPTH (ANGSTROMS)
0
1
2
3
4
5
0
100
200
300
0
1000
2000
3000
4000

FIGURE 14

FIGURE 15

Fluorine concentration versus depth for glass-coated lunar rock chip 64455,24. Straight lines have been drawn connecting "first run" data for the exterior surface. Error bars for "interior surface" data are omitted for clarity. (See text, page 43.)

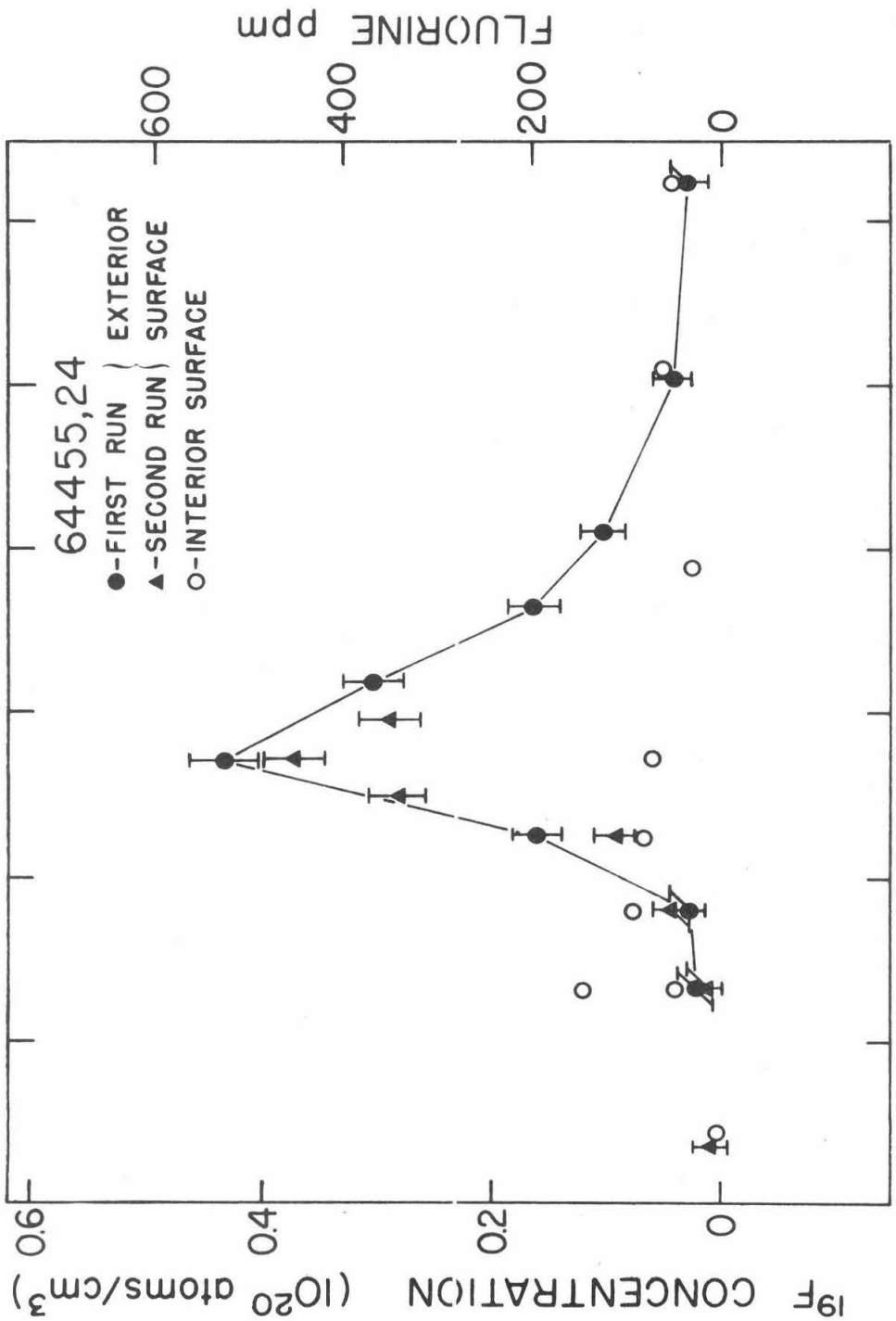
64455,24
●-FIRST RUN ⟩ EXTERIOR
▲-SECOND RUN ⟩ SURFACE
o-INTERIOR SURFACE
^{19}F CONCENTRATION (10^{20} atoms/cm^3)
FLUORINE ppm
DEPTH (μm)
0
0.2
0.4
0.6
0.8
1.0
0
200
400
600
0.2
0.4
0.6

FIGURE 15

FIGURE 16

Fluorine concentration versus depth for two feldspar-rich lunar rock chips 64455,33. Error bars for "interior surface" data are omitted for clarity. (See text, page 43.)

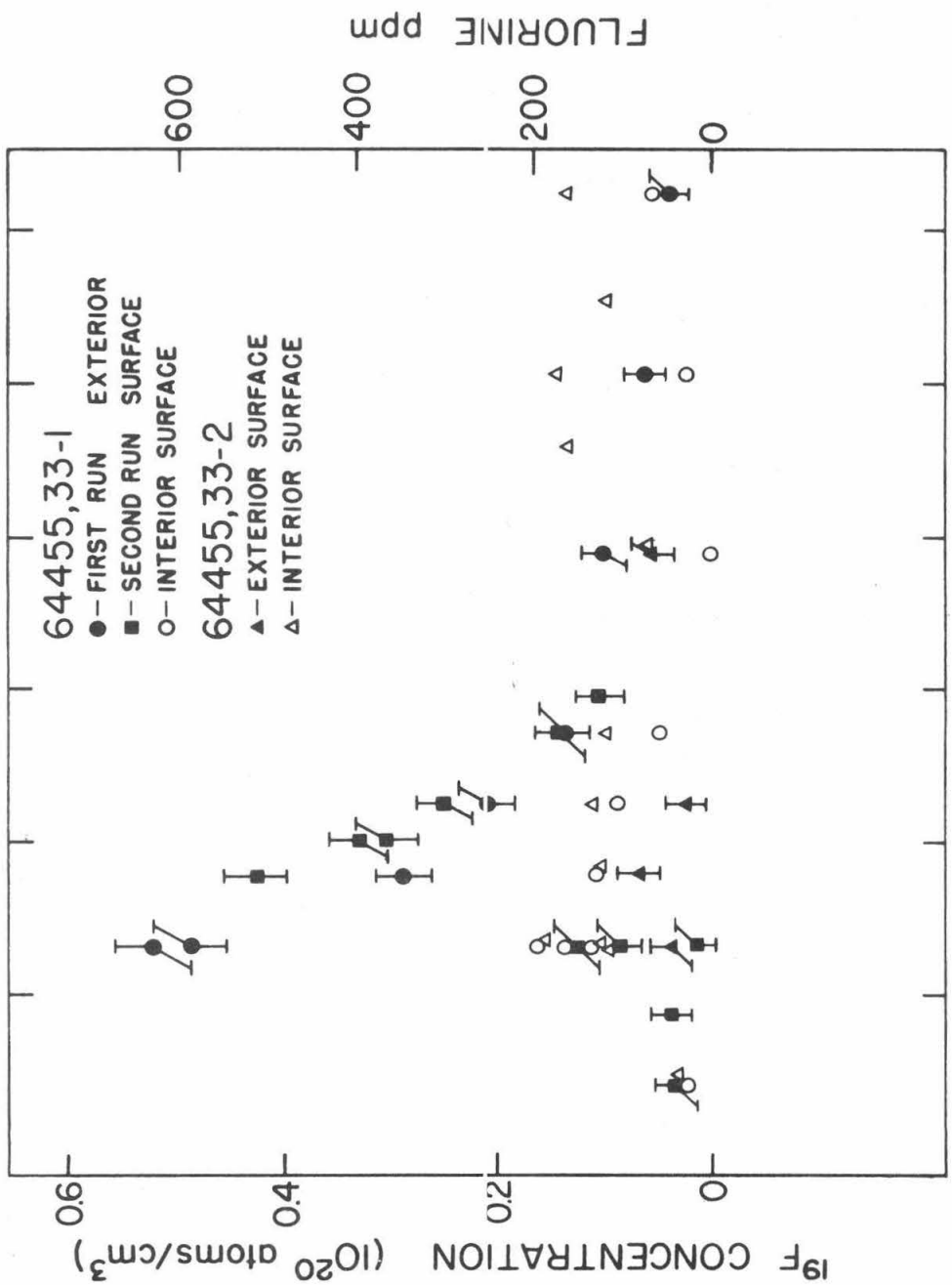
64455,33-1
● - FIRST RUN EXTERIOR
■ - SECOND RUN SURFACE
○ - INTERIOR SURFACE
64455,33-2
▲ - EXTERIOR SURFACE
△ - INTERIOR SURFACE
^{19}F CONCENTRATION (10^{20} atoms/cm^3)
FLUORINE ppm
DEPTH (μm)
0
0.2
0.4
0.6
0.8
1.0
200
400
600

FIGURE 16

FIGURE 17

Fluorine concentration versus depth for lunar glass chip 65315,6. Data for "first run" and "second run" were taken in steps of increasing energy (depth). Error bars for "second run" data are omitted for clarity. Straight lines have been drawn connecting the data points. (See text, page 46.)

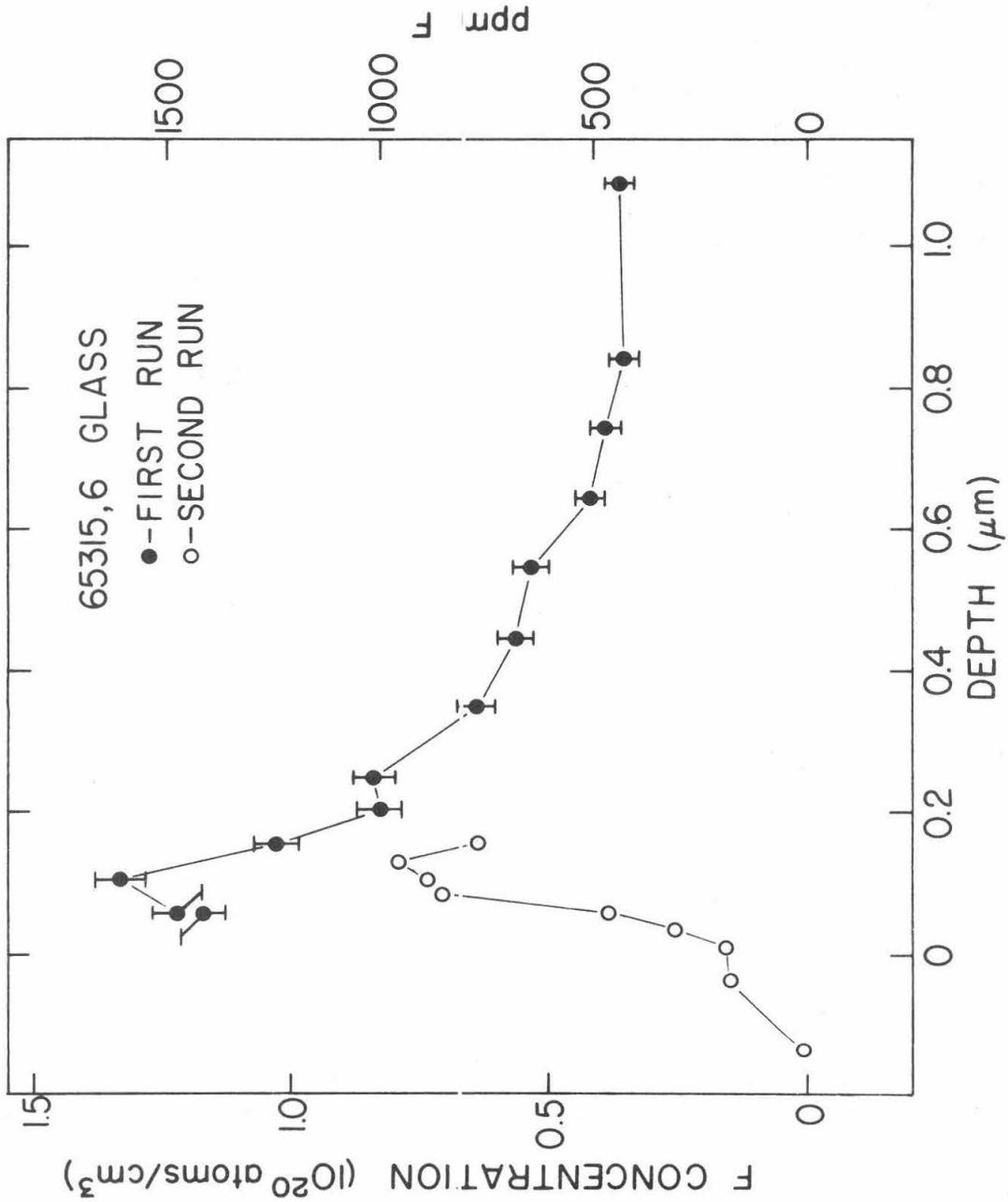
65315,6 GLASS
●-FIRST RUN
○-SECOND RUN
F CONCENTRATION (10^{20} atoms/cm^3)
ppm F
DEPTH (μm)
0
0.5
1.0
1.5
500
1000
1500
0.2
0.4
0.6
0.8
1.0

FIGURE 17

FIGURE 18

Hydrogen concentration versus depth for lunar breccia chip 68815,27. Data from an interior surface of the same chip are also plotted with error bars omitted for clarity. The first two data points (taken at the resonance energy, corresponding to zero depth) for each surface show a comparable decrease in counting rate. Subsequent "first run" points are in increasing energy (depth) steps, with the direction reversed for "second run" data. (See text, page 49.)

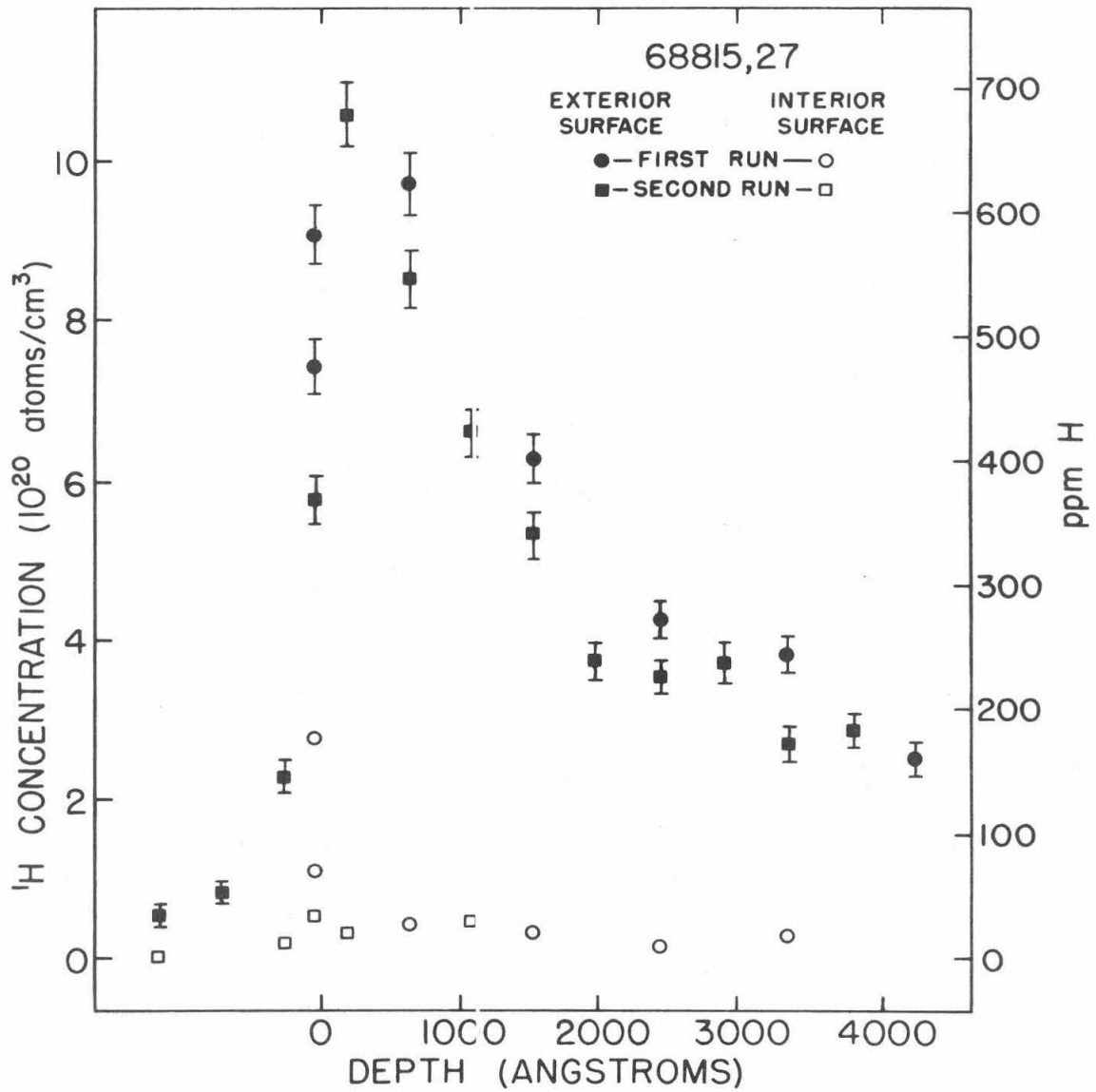
68815,27
EXTERIOR SURFACE
INTERIOR SURFACE
●—FIRST RUN—○
■—SECOND RUN—□
^{1}H CONCENTRATION (10^{20} atoms/cm^3)
ppm H
DEPTH (ANGSTROMS)
0
2
4
6
8
10
0
100
200
300
400
500
600
700
0
1000
2000
3000
4000

FIGURE 18

FIGURE 19

Curves drawn through each of three consecutive data sets (runs) for the 68815,27 hydrogen depth distribution (Figure 18) show the evolution of the profile due to irradiation with the ^{19}F beam. Straight lines have been drawn connecting the data points except near the peak, where a somewhat arbitrary curve has been drawn as an estimate of its shape for each run. The dash-dot curve connects data for the interior surface, with the vertical dash-dot line at zero depth connecting the three data points taken at the resonance energy, each having a successively lower yield. (See text, page 49.)

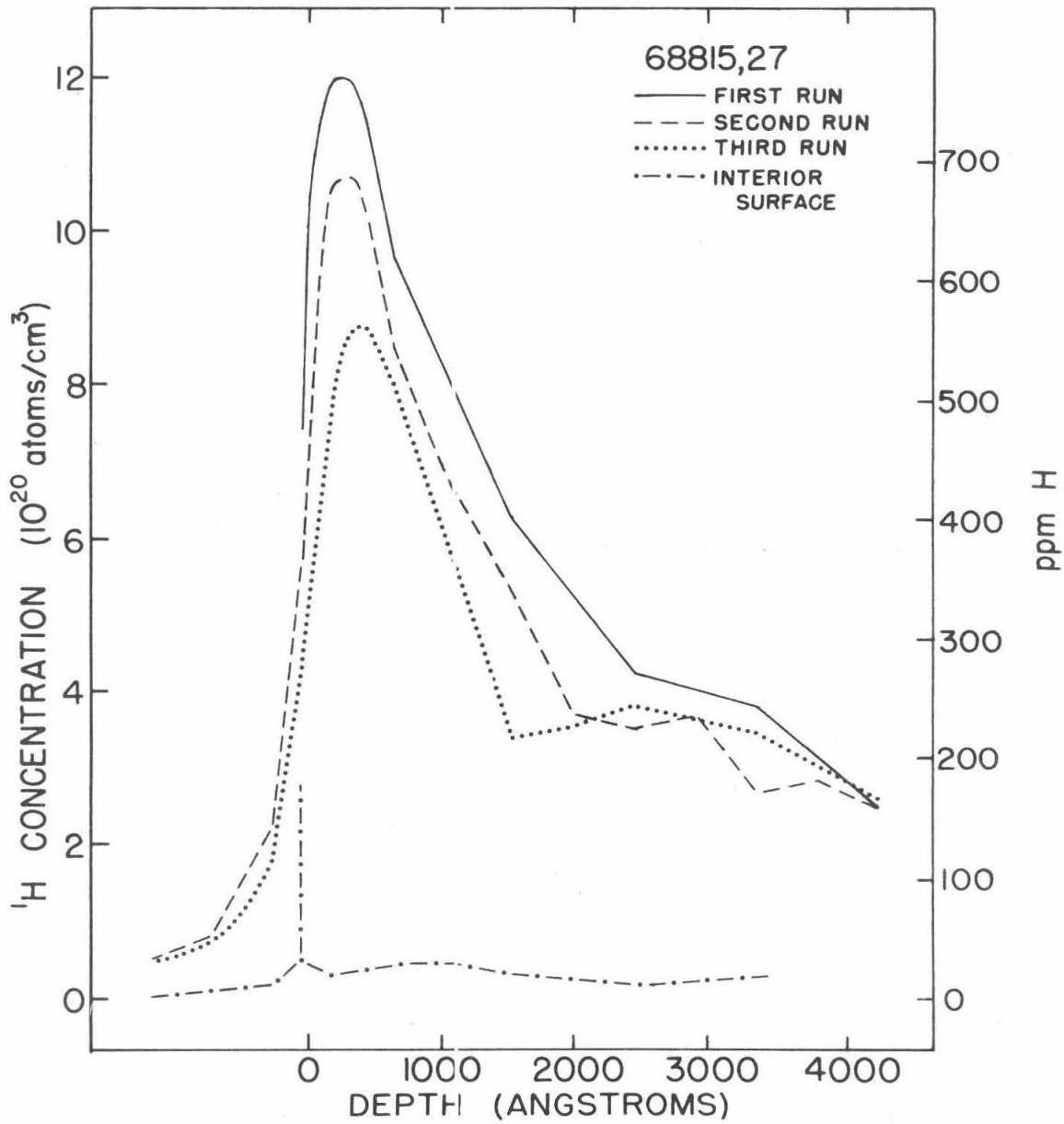
68815,27
FIRST RUN
SECOND RUN
THIRD RUN
INTERIOR SURFACE
^{1}H CONCENTRATION (10^{20} atoms/cm^3)
ppm H
DEPTH (ANGSTROMS)
0
2
4
6
8
10
12
0
100
200
300
400
500
600
700
0
1000
2000
3000
4000

FIGURE 19

FIGURE 20

Fluorine concentration versus depth for breccia chip 68815,27, both lunar exterior and interior surfaces. Each curve is drawn through two consecutive runs, showing the excellent reproducibility of these measurements. The dotted curve represents the data for the hydrogen concentration on the same sample multiplied by 1/10 and plotted on the same depth scale for comparison. The difference between the proton beam energy E and the resonance energy E_R (= 872 keV) is shown on the top scale. The fluorine content is also expressed in ppm on the right-hand scale. Only sample error bars are shown. (See text, page 52.)

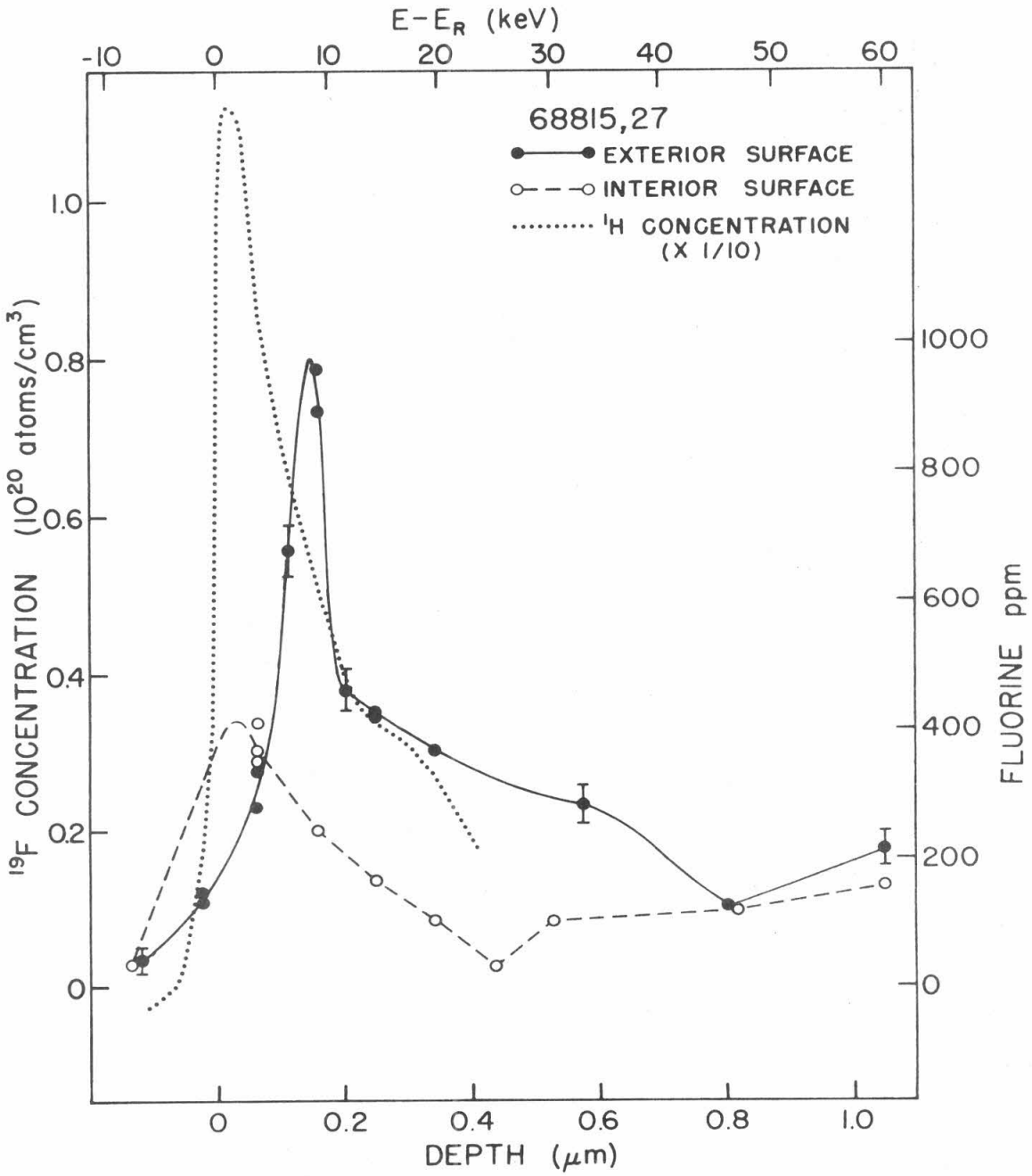
E-E$_R$ (keV)
-10
0
10
20
30
40
50
60
68815,27
EXTERIOR SURFACE
INTERIOR SURFACE
^{1}H CONCENTRATION
(X 1/10)
^{19}F CONCENTRATION (10^{20} atoms/cm^3)
FLUORINE ppm
0
0.2
0.4
0.6
0.8
1.0
200
400
600
800
1000
DEPTH (μm)

FIGURE 20

FIGURE 21

Fluorine concentration versus depth for lunar anorthosite fragment 66044,8. The data represented by the solid circles were taken following a $\frac{1}{2}$ - mm shift in the center of the proton beam spot on the sample after the data shown by the open circles had been taken. Only sample error bars are shown. (See text, page 54.)

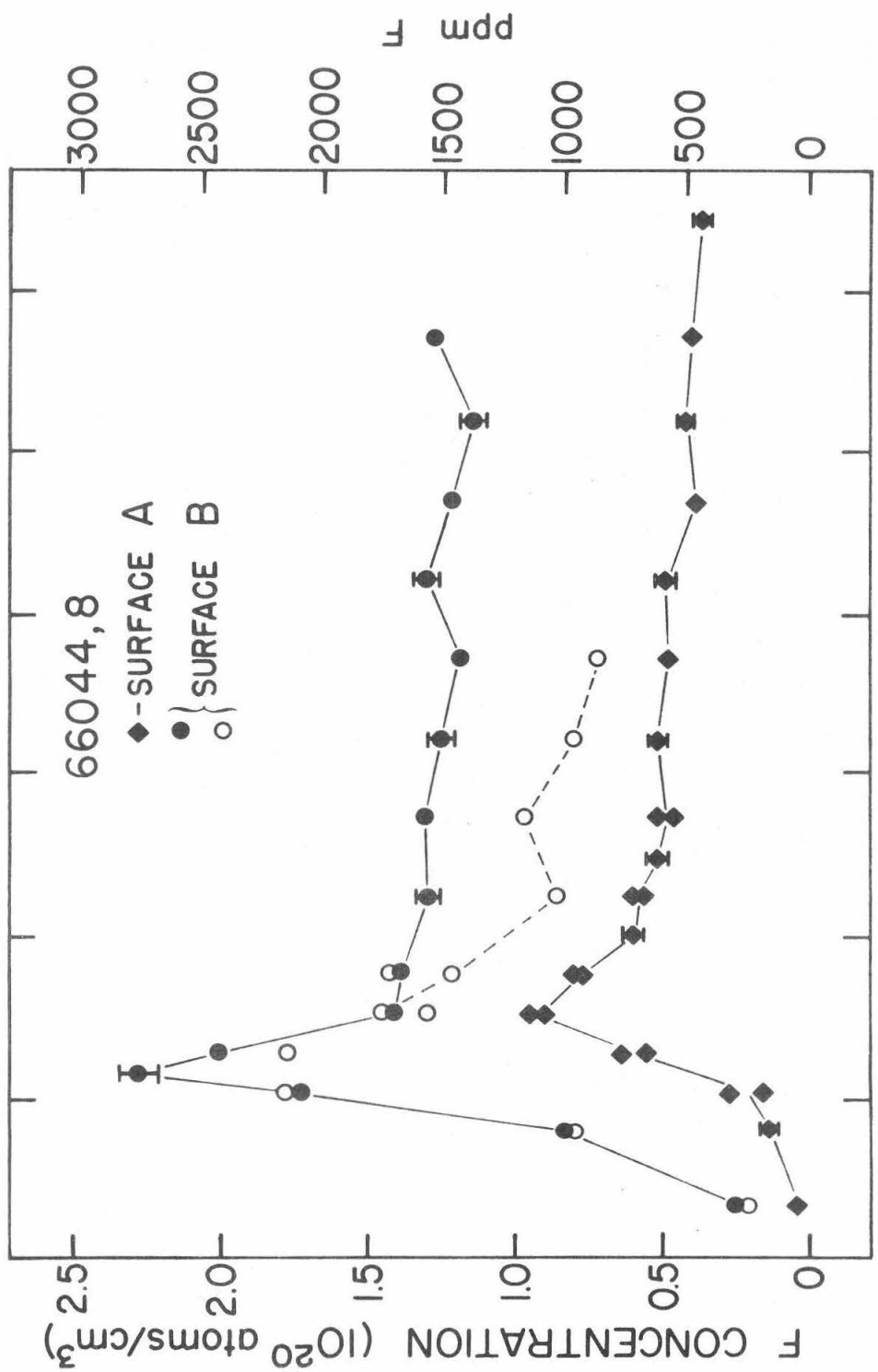
66044,8
◆-SURFACE A
●}SURFACE B
○}
F CONCENTRATION (10²⁰ atoms/cm³)
ppm F
DEPTH (μm)
0
0.5
1.0
1.5
2.0
2.5
500
1000
1500
2000
2500
3000
0.2
0.4
0.6
0.8
1.0

FIGURE 21

FIGURE 22

$^{27}Al(p,\gamma)^{28}Si$ measurements on lunar samples. This composite figure shows data for 11-MeV γ-ray counts per 6 μC of incident protons versus proton energy near the 992-keV resonance (indicated by the solid line at E_R) for six lunar sample surfaces. The estimated shape of the step (due to a presumably uniform aluminum content in a particular sample) is shown for each sample as a solid curve, with an arrow drawn to the center of the step indicating the magnitude of the shift in energy from E_R. The implied average surface potential is given for each sample. The more gentle slopes (e.g. 68124,3) probably indicate large (a few keV) fluctuations about the average potential, while the steeper slopes (e.g. 65315,6) may be largely due to the spread in energy of the proton beam. (See text, page 54.)

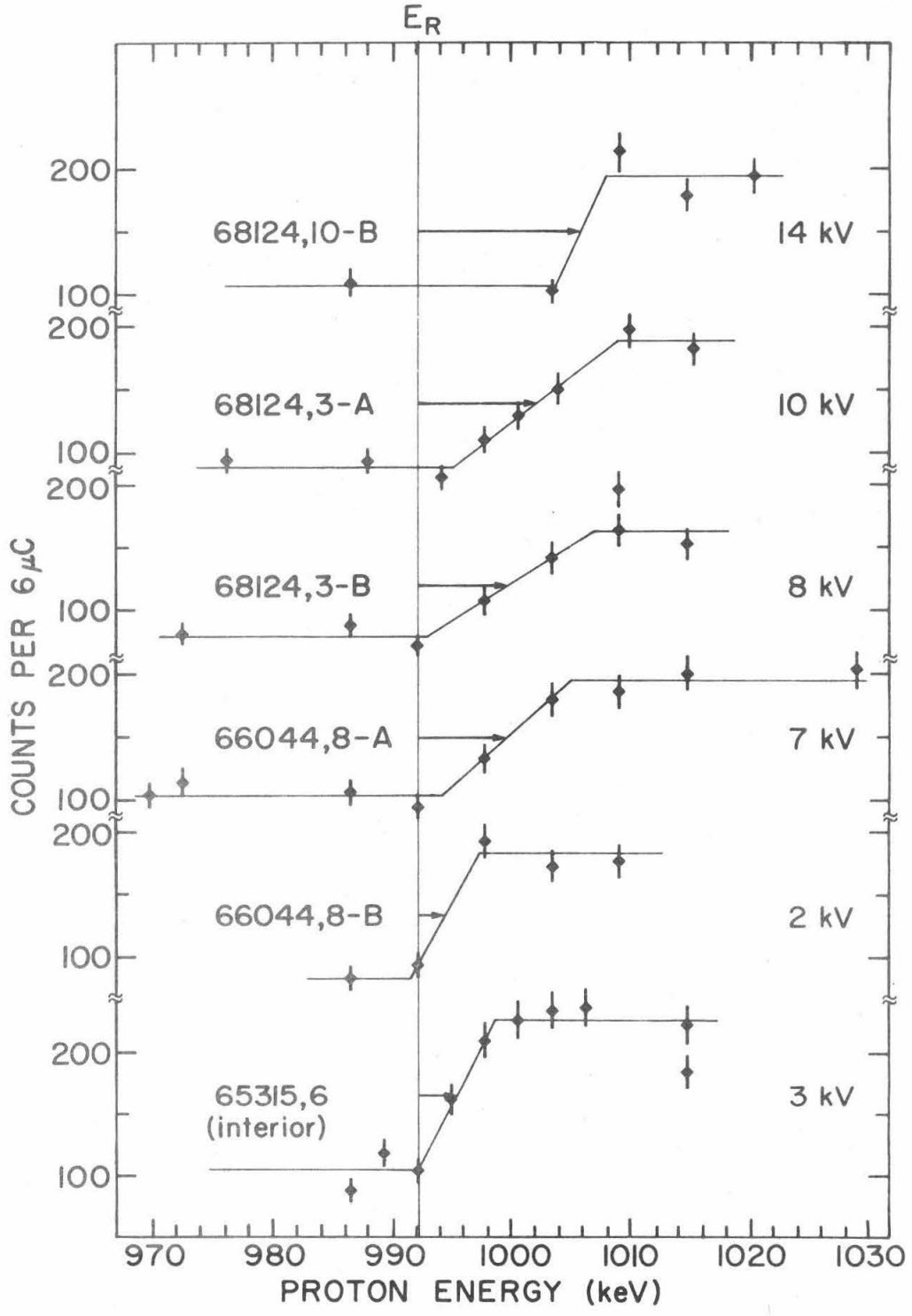
E_R
68124,10-B
14 kV
68124,3-A
10 kV
68124,3-B
8 kV
66044,8-A
7 kV
66044,8-B
2 kV
65315,6
(interior)
3 kV
COUNTS PER 6 μC
100
200
970
980
990
1000
1010
1020
1030
PROTON ENERGY (keV)

FIGURE 22

FIGURE 23

Fluorine concentration versus depth for lunar glass spherule 68124,3. Solid circles and open circles represent "first run" and "second run" data respectively for surface B. For surface A, data from two consecutive runs are plotted together. Only sample error bars are shown. (See text, page 55.)

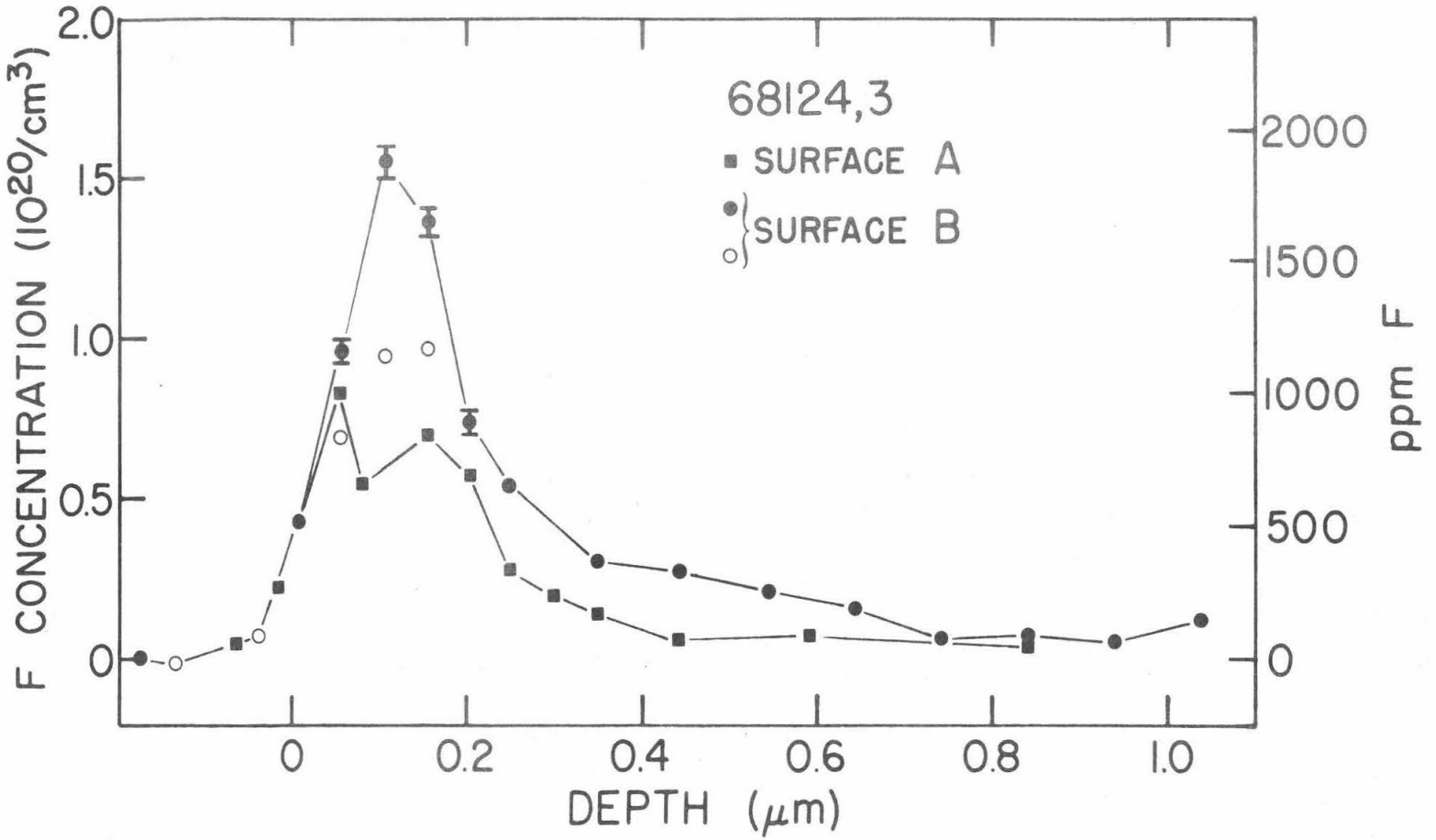
68124,3
SURFACE A
SURFACE B
F CONCENTRATION (10^{20}/cm^3)
2.0
1.5
1.0
0.5
0
2000
1500
1000
500
0
ppm F
0
0.2
0.4
0.6
0.8
1.0
DEPTH (μm)

FIGURE 23

FIGURE 24

Fused silica simulation experiment results. Data shown are representative of a set of samples subjected first to radiation damage and H_2O exposure tests. Two of the samples were damaged by irradiating them with 86-keV $^{16}O^-$ ions for 4 hours to a total dose of 1.4×10^{17} ions/cm^2. One of these (solid circles) was subsequently exposed to H_2O in both liquid (submerged in distilled water for 24 hr) and vapor (laboratory atmosphere for one week) form, while the other (solid triangles) was exposed only to dry N_2 gas for 2 hr. A third sample (open circles) was not radiation damaged but was given the same H_2O exposure as the first sample. Only sample error bars are shown on the data points obtained during the subsequent H analysis, performed to determine the extent of H_2O penetration. The solid curve represents typical results for a clean fused silica sample with a normal (for this batch) H content of $\sim$20 ppm. (See text, page 57.)

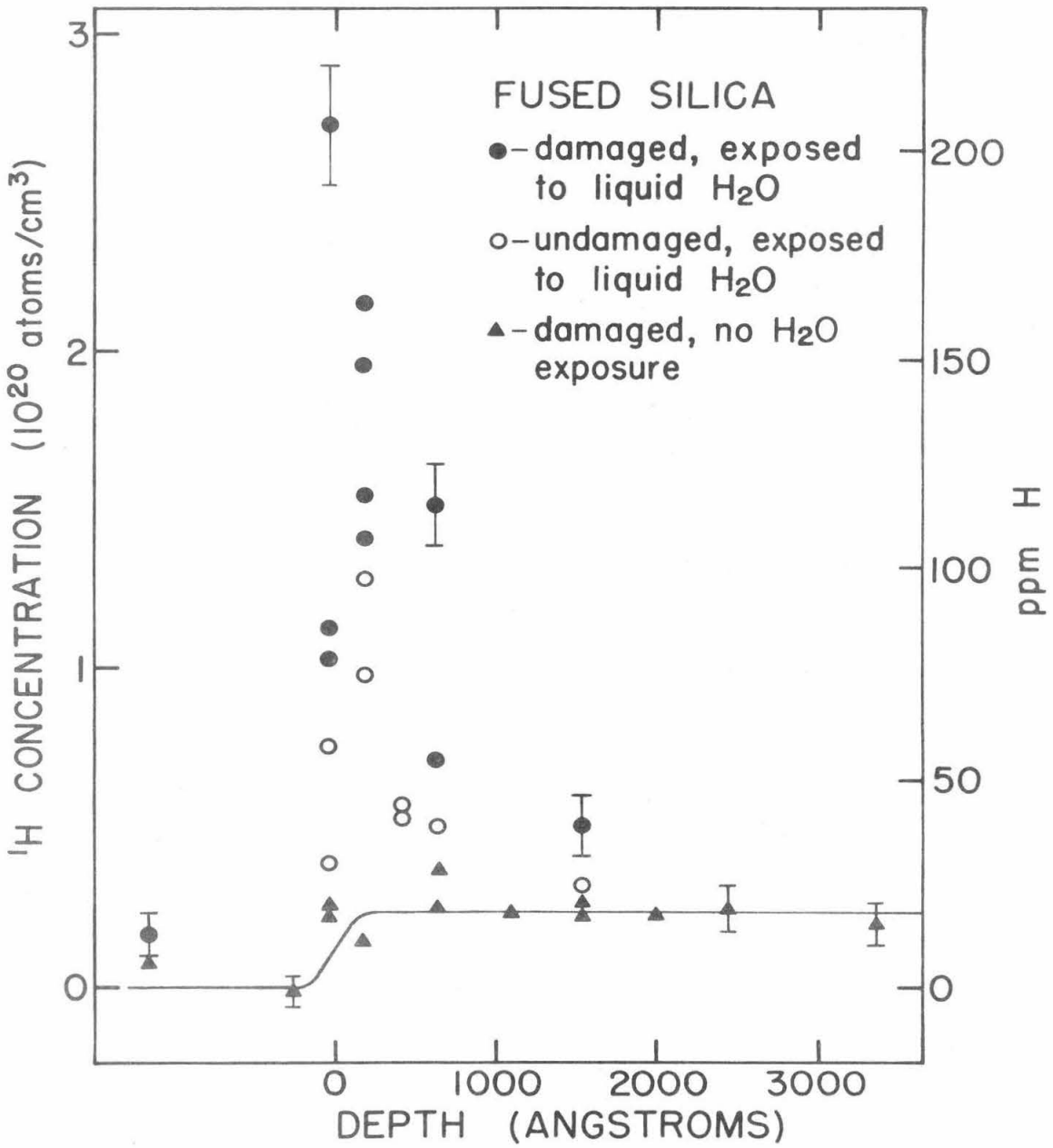
FUSED SILICA
●-damaged, exposed to liquid H_2O
○-undamaged, exposed to liquid H_2O
▲-damaged, no H_2O exposure
^1H CONCENTRATION (10^{20} atoms/cm^3)
ppm H
DEPTH (ANGSTROMS)
0
1
2
3
50
100
150
200
1000
2000

FIGURE 24

FIGURE 25

Equilibrium H distribution functions resulting from implantation of a monoenergetic proton source of flux ϕ_o for lunar surface samples subject to a constant atomic erosion rate v. Straggling is neglected, so each incident proton is assumed to penetrate a distance R_o (corresponding to the mean projected range of protons of energy E_o) along its incident direction. The distributions shown are for normal incidence ($H_N(x)$), an isotropic angular distribution ($H_I(x)$), and protons incident from the solar direction ($H_S(x)$); where x is the depth in the sample. (See text, page 74 and Appendix E, page 110.)

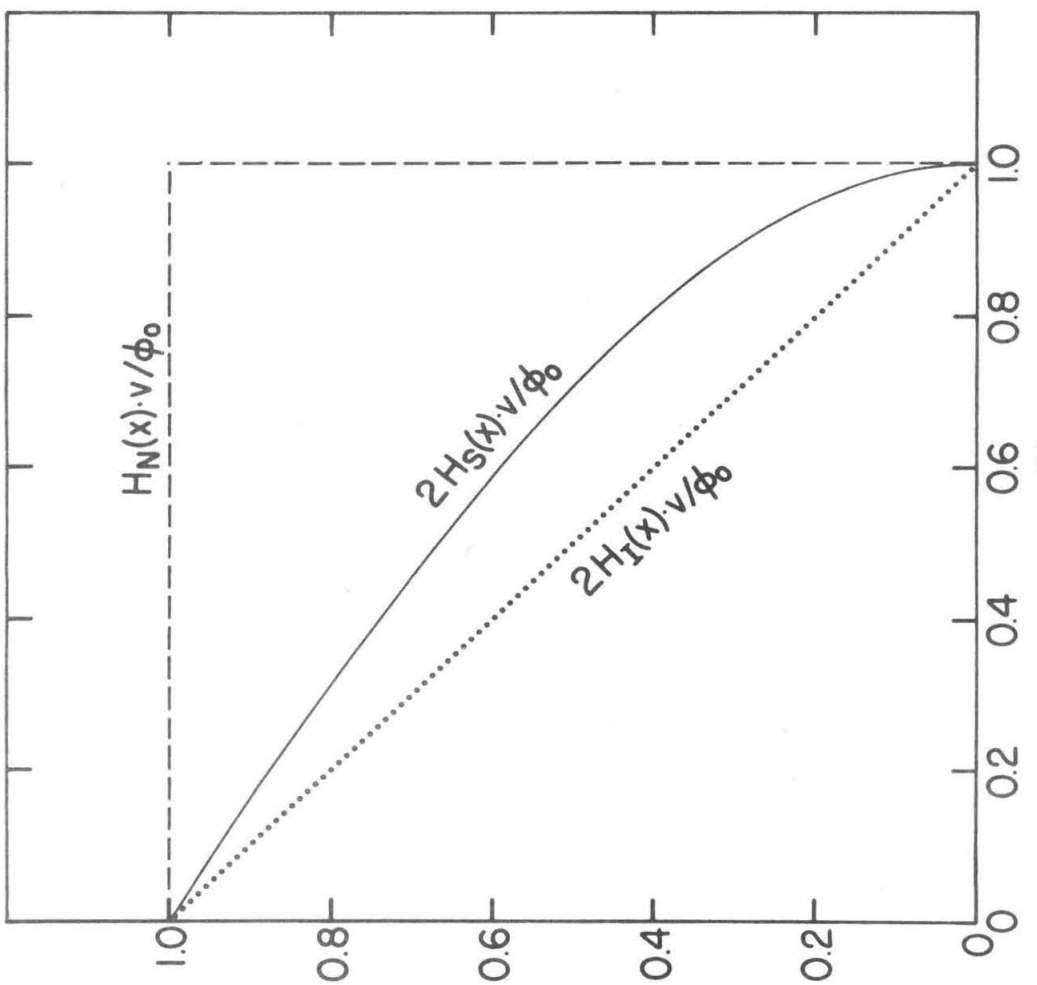
$H_N(x)\cdot v/\phi_0$
$2H_S(x)\cdot v/\phi_0$
$2H_I(x)\cdot v/\phi_0$
1.0
0.8
0.6
0.4
0.2
0
0
0.2
0.4
0.6
0.8
1.0
x/R_0

FIGURE 25

FIGURE 26

"Suprathermal" proton flux spectrum $d\phi/dE$ versus proton energy E. Data points with associated error bars are taken from satellite observations reported by Frank (1970). A spectrum adjusted to give a rough fit to the observed H distribution in 68815,27, assuming an atomic erosion rate of 0.5 Å/yr, is indicated by the solid lines. (See text, page 74.)

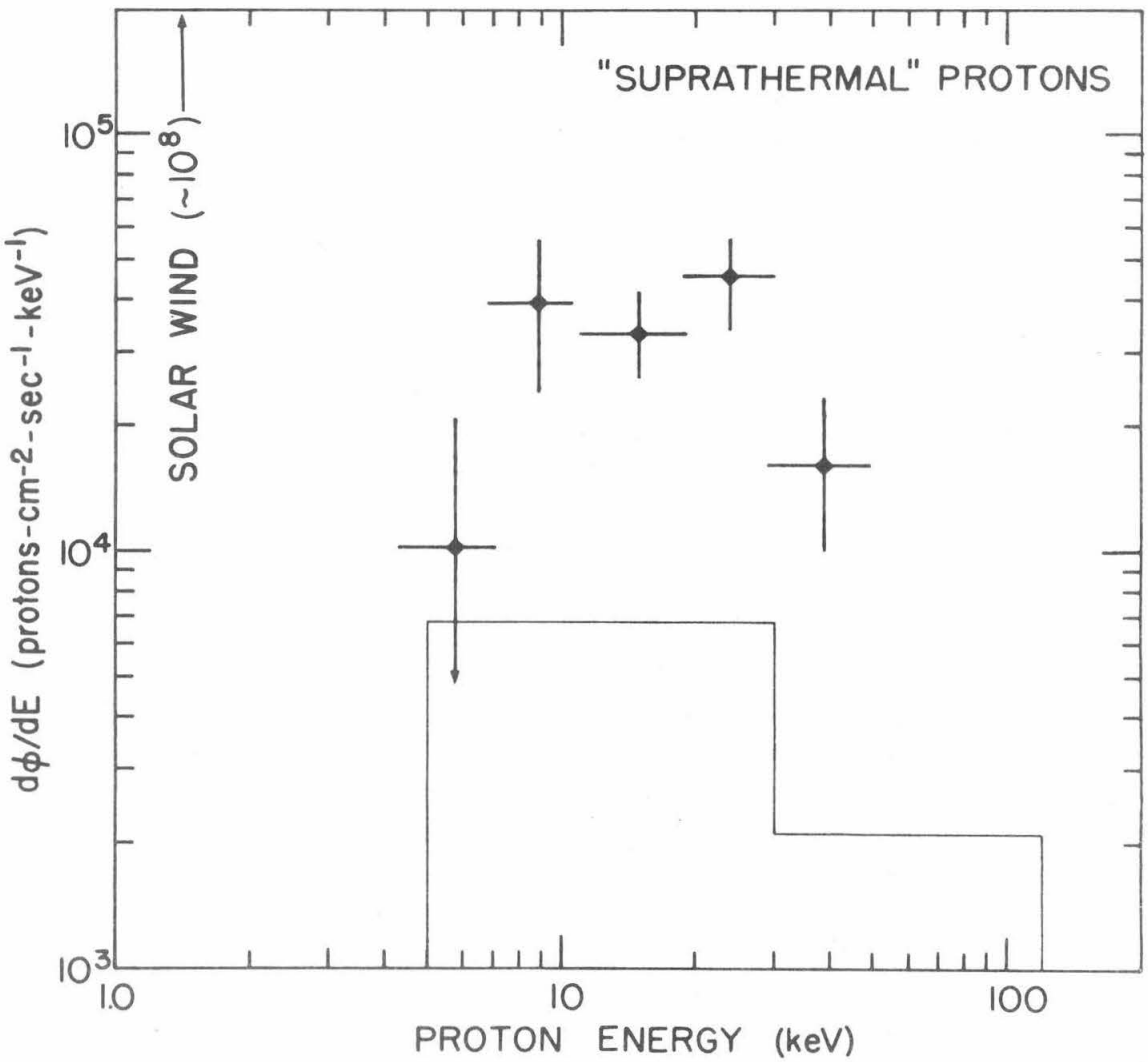
"SUPRATHERMAL" PROTONS
SOLAR WIND (~10^8)
dφ/dE (protons-cm^-2-sec^-1-keV^-1)
10^5
10^4
10^3
1.0
10
100
PROTON ENERGY (keV)

FIGURE 26

FIGURE 27

Implantation of solar protons in lunar samples. The data points are from sample 68815,27 (Figure 18). The solid curve is the distribution resulting from the flux spectrum indicated by the solid lines in Figure 26, assuming an atomic erosion rate of 0.5 Å/yr, and calculated using equations E.8 and E.9 of Appendix E. The spectrum was chosen to give a rough fit to the data, using a proton range-energy relation derived from Schiøtt (1966) and neglecting range straggling and diffusion. The dashed curve indicates the limit of penetration of the present-day solar wind, including the effects of range straggling. With no diffusive losses, the peak H content at the surface would be greater than 10^{23} H atoms/cm^3 -- more than two orders of magnitude higher than the observed H content near the surface of sample 68815,27. (See text, page 75.)

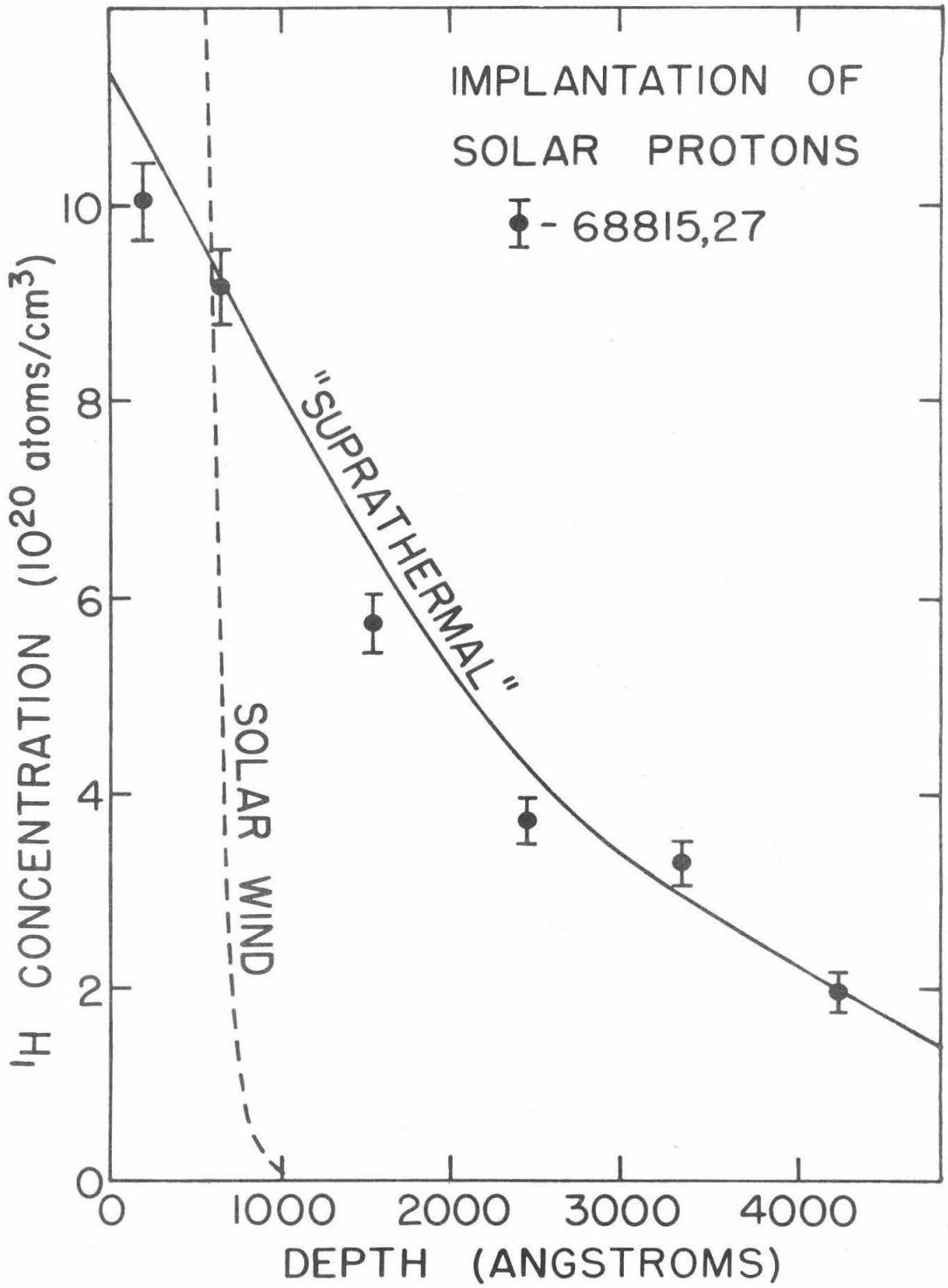
IMPLANTATION OF
SOLAR PROTONS
- 68815,27
"SUPRATHERMAL"
SOLAR WIND
^{1}H CONCENTRATION (10^{20} atoms/cm^3)
0
2
4
6
8
10
0
1000
2000
3000
4000
DEPTH (ANGSTROMS)

FIGURE 27

FIGURE 28

Data from two obsidian samples with thin hydration layers. Sample 2 (a) was artificially hydrated at 75°C for 2 days. Sample 4 (b) was hydrated in a normal laboratory environment (room temperature) for 10 years. Data are γ-ray counts per 3 μC of $^{19}F^{4+}$ plotted against the incident ^{19}F ion energy E_o. The depth scale is calculated from the stopping power of the obsidian for ^{19}F ions, with the zero point corresponding to the resonance energy (16.45 MeV). The data imply peak H_2O contents of ∿2% by weight, with hydration layer thicknesses of 0.11 μm and 0.19 μm for samples 2 and 4, respectively. (See text, page 86.)

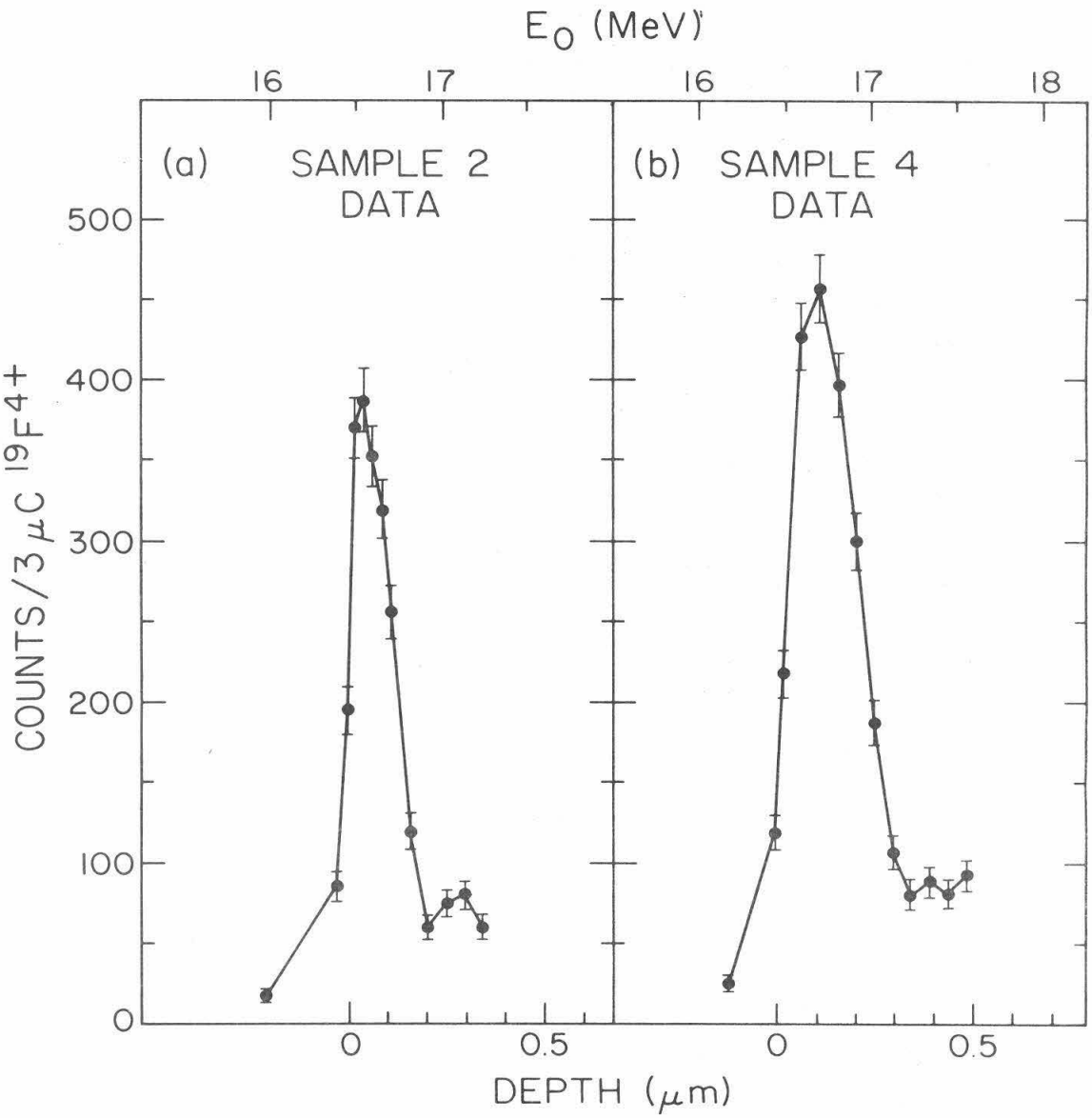
E_0 (MeV)
16
17
16
17
18
(a) SAMPLE 2 DATA
(b) SAMPLE 4 DATA
500
400
300
200
100
0
COUNTS/3 μC $^{19}F^{4+}$
0
0.5
0
0.5
DEPTH (μm)

FIGURE 28

FIGURE 29

Unfolding procedure for obsidian sample number 5. In (a) raw data are plotted for sample 5 and for a freshly exposed, unhydrated interior sample (0.3% H_2O). The hydration profile in (b) is obtained by subtracting the counting rate for the unhydrated sample (dashed curve) from the data for sample 5 at each energy, and then performing the unfolding procedure described in the text (Section II, Part A) in which the γ-ray counts due to the resonance at 17.64 MeV are subtracted, leaving only the yield due to the resonance at 16.45 MeV. The resulting reduced data are then fitted with an H_2O content scale (the 0.3% H_2O is added back in the placement of the zero point of this scale) and a depth scale using the calculated stopping power of obsidian for ^{19}F ions. (See text, page 87.)

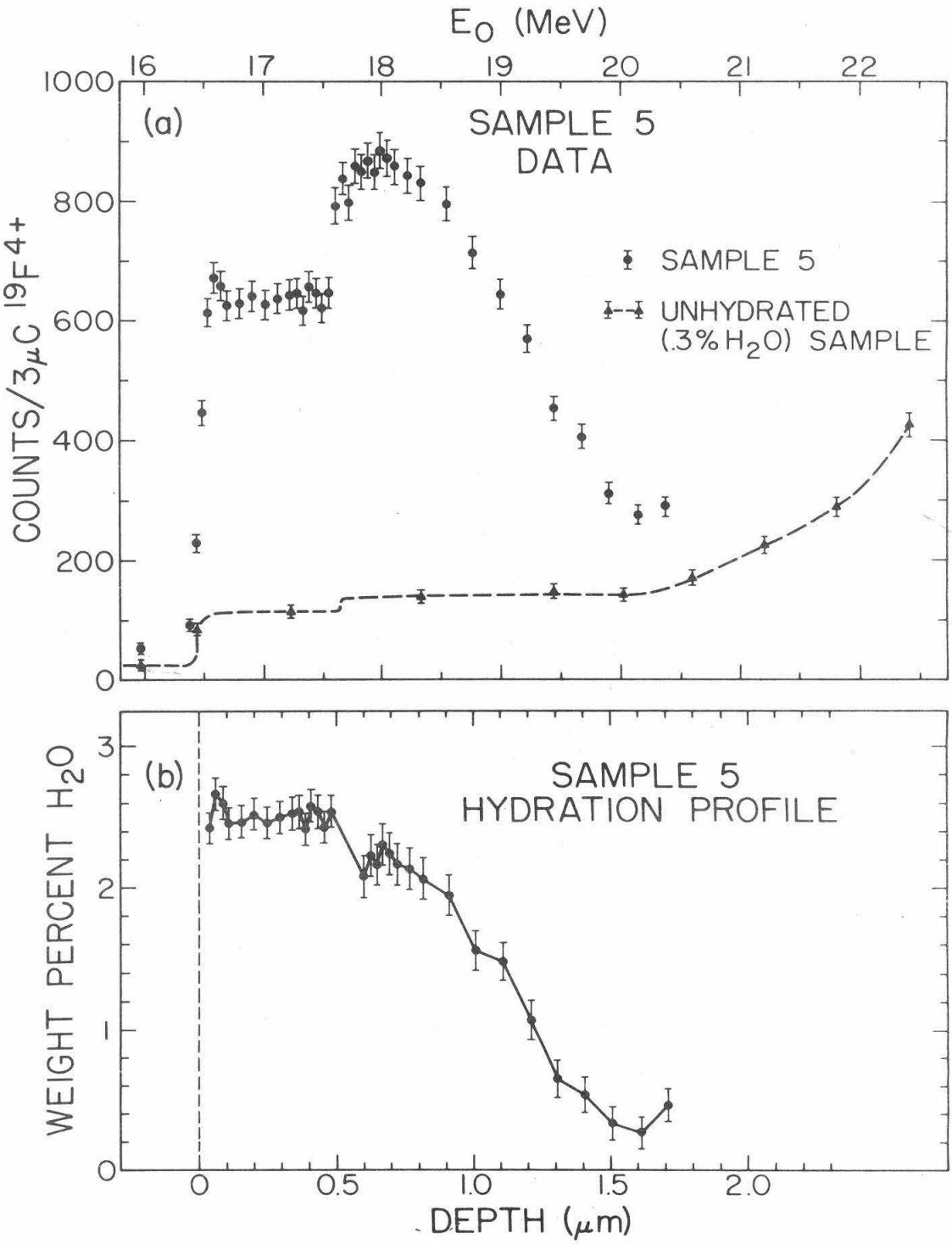
E_0 (MeV)
16
17
18
19
20
21
22
(a)
SAMPLE 5
DATA
SAMPLE 5
UNHYDRATED
(.3% H_2O) SAMPLE
COUNTS/3μC $^{19}F^{4+}$
1000
800
600
400
200
0
(b)
SAMPLE 5
HYDRATION PROFILE
WEIGHT PERCENT H_2O
3
2
1
0
0
0.5
1.0
1.5
2.0
DEPTH (μm)

FIGURE 29

FIGURE 30

Hydration profiles for obsidian samples 9 (a) and 7 (b). These profiles were obtained in the same manner as shown in Figure 29 for sample 5. Error bars are not shown, but are of comparable magnitude to those in Figure 29 (b) (1σ statistical uncertainties). Samples 7 and 9 both appear to have two plateau levels in their hydration profiles. (See text, page 88.)

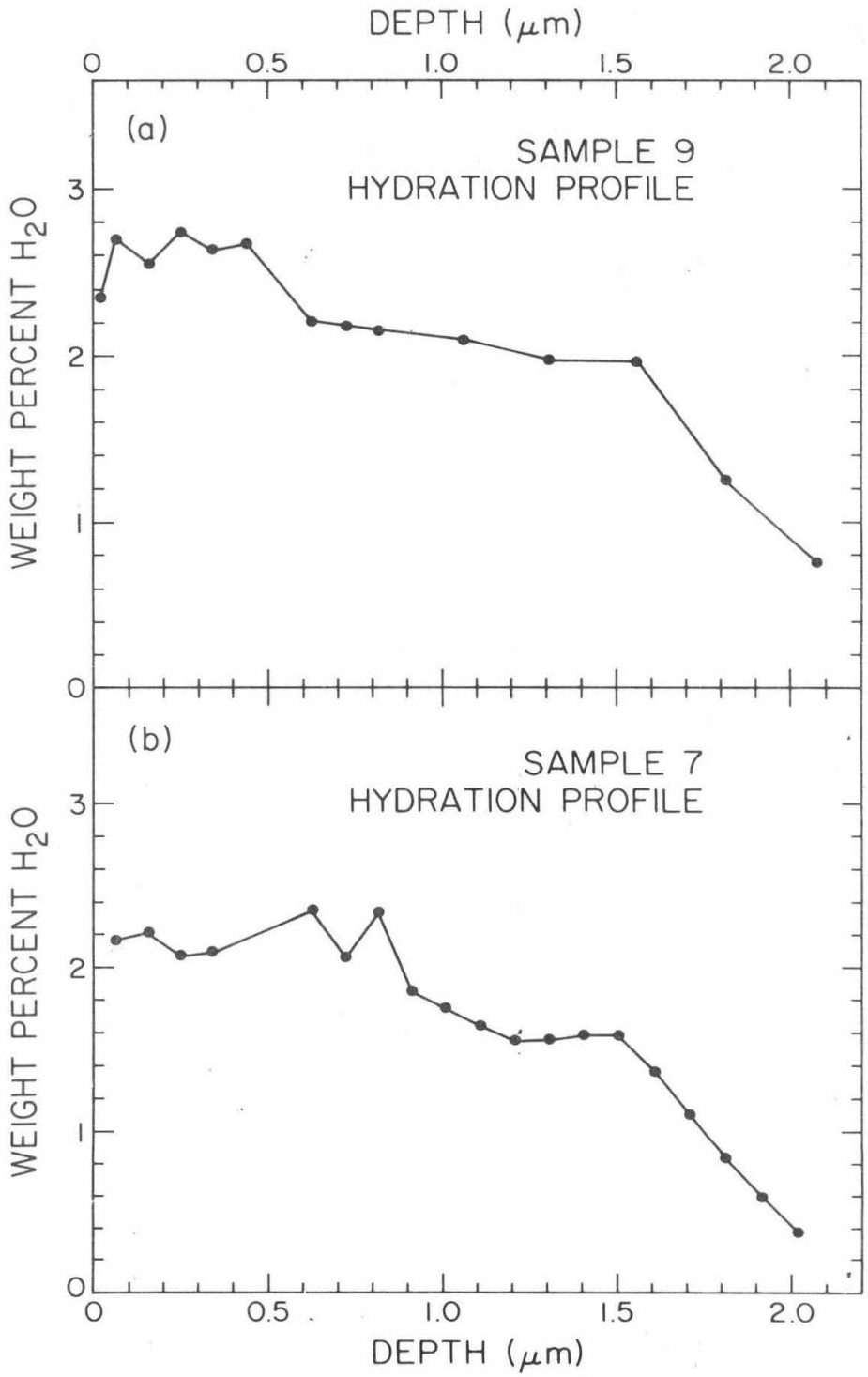
DEPTH (μm)
0
0.5
1.0
1.5
2.0
(a)
SAMPLE 9
HYDRATION PROFILE
WEIGHT PERCENT H2O
3
2
1
0
(b)
SAMPLE 7
HYDRATION PROFILE
WEIGHT PERCENT H2O
3
2
1
0
0
0.5
1.0
1.5
2.0
DEPTH (μm)

FIGURE 30